Integrated Acousto-optic Devices based on Brillouin Optomechanics

Qiyu Liu

A dissertation

submitted in partial fulfillment of the

requirements for the degree of

Doctor of Philosophy

University of Washington

2020

Reading Committee:

Mo Li, Chair

Kai-Mei Fu

Arka Majumdar

Program Authorized to Offer Degree:

Electrical Engineering

University of Washington

Abstract

Integrated Acousto-optic Devices based on Brillouin Optomechanics

Qiyu Liu

Chair of the Supervisory Committee:
Professor Mo Li
Electrical and Computer Engineering

Brillouin scattering is the inelastic light-sound interaction. It has given birth to two popular research topics: stimulated Brillouin scattering and acousto-optics. With recent advances in nanotechnology, research on both stimulated Brillouin scattering and acousto-optics has focused on scaling down the traditional bulky material to nanophotonic chips for functional devices. The integrated platforms have not only the advantage of a small footprint but also the flexibility of design and fabrication.

On-chip stimulated Brillouin scattering has been demonstrated in varieties of platforms for integrated photonics. The key factor of stimulated Brillouin scattering is the Brillouin gain, which is determined by the intensity of the coherent acoustic waves. Because the acoustic wave frequency is about five orders of magnitude lower than that of light, the energy efficiency of acoustic

generation through intense pump light is relatively low. On the contrary, in acousto-optics, acoustic waves are generated piezoelectrically with microwave at the same frequency, which is much efficient. However, previous work in acousto-optics focused on either acoustic modulation of cavities or small deflection of light. The interaction of light and sound with the wavelength in the same scale remains unexplored.

My first project focused on exploring new phenomena and inventing novel devices by combining the advantages of stimulated Brillouin scattering and the acousto-optic modulation. With successfully integrating sub-optical wavelength acoustic transducers onto aluminum nitride photonic integrated circuits, we experimentally observed the backscattering of photons with piezoelectrically excited phonons for the first time. We systematically studied the electromechanical Brillouin scattering system. Potential applications as single-sideband modulators and microwave photonic links have also been demonstrated.

In the second project, a subwavelength suspended phononic waveguide was realized. The coupling of an acoustic wave was achieved through a parabolic acoustic coupler. Different acoustic couplers with interdigital transducers with different apertures are fabricated for comparison and optimization. Transmission of the Lamb wave at 3.4 GHz was detected even in the presence of high waveguide loss. Furthermore, the phenomenon of mode conversion from membrane acoustic waves to subwavelength guided modes was first visualized through microwave impedance microscopy. This project provides guidance for the future design of co-confining light and sound in subwavelength structures.

Besides these two projects, I will also discuss the fundamental of surface acoustic waves and the technical details in surface acoustic wave device design in Chapter 2. Future perspectives for integrated acousto-optic devices are included in the last chapter.

TABLE OF CONTENTS

LIST OF FIGURES

LIST OF TABLES

ACKNOWLEDGEMENTS

I would like to give my deepest gratitude to my advisor, Prof. Mo Li, who led me to photonics and advised me during my Ph. D. career. Without his careful instruction and kindly encouragement, I would never achieve any success in this dissertation. His enthusiasm for science and rigorous attitude to research inspired me a lot.

I would also like to give my special thanks to Dr. Huan Li. Huan is a very kind person with intelligent thoughts and creative ideas. Huan is always the first person I am heading for when I need help. I learned a lot from him.

My appreciation also goes to Dr. Semere Ayalew Tadesse for his mentoring in nanofabrication during my first year. Without his help, I would not learn the device fabrication so fast.

I also thank my collaborators, Prof. Keji Lai and Dae-Hun Lee, at UT Austin, for their selfless sharing and helps on research.

I would like to thank Dr. Junyang Chen, Dr. Nathan Youngblood, Dr. Li He, Dr. Che Chen, Ruoming Peng, Bingzhao Li, Changming Wu, Seokyeong Lee, Euijae Shim, I-Tung Chun, and Adina Ripin for help and friendship.

I would also like to thank all staff members from Washington Nanofabrication Facility and Molecular Analysis Facility at the University of Washington for their careful maintenance of the tools and timely help. I would like to especially mention the assistance and advice from Dr. Mark Morgan, Dr. Darick Baker, Shane Patrick, and Dr. Fred Newman. The same acknowledgment goes

to all staff members from the Minnesota Nano Center and the Characterization Facility, especially Kevin Roberts, Lage von Dissen, and Rich Macy, for the timely assistance.

I would also like to give my special thanks to my girlfriend, Helin Wang. I enjoyed everyday living with her.

Finally, my special gratitude goes to my parents for their love and support.

Chapter 1. INTRODUCTION

1.1 A BRIEF REVIEW OF PHOTONIC INTEGRATED CIRCUITS

1.1.1 *From fiber optics to photonic integrated circuits*

The phenomenon of total internal reflection happens when the light is incident from a medium with a high refractive index to one with a low refractive index. By substituting into Snell's Law, one can get that when the incident angle is larger than $\arcsin(n_2/n_1)$, the transmission vanishes. Guiding light by total internal reflection was first introduced in the famous "light fountain" or "light pipe" experiment by Daniel Colladon and Jacques Babinet in Paris in the early 1840s, that light would follow the water flow but not leak to air when the incident angle reached 48 degrees or greater. The experiment inspired practical applications like internal illumination during dentistry, surgical lamps, and, more importantly, optical fibers. Optical fibers are flexible and transparent fibers containing high refractive-index core and low refractive index-claddings. Owing to the invention of the laser and the development of low loss optical fiber after Charles K. Kao and George A. Hockham promoted the idea in the 1960s[1], [2], fiber optics have incubated numerous applications in telecommunications[1], optical amplifiers[3]–[7], fiber lasers[8]–[12], and sensors[13]–[15]. Similar to moving from bulky electronics to microchips, there have been visions of shrinking down fiber optic systems on a chip as integrated photonic circuits, which contained all functional optical components including sources, waveguides, modulators, amplifiers, and detectors on a chip since the 1970s [16], [17]. Recently, with the promotion of semiconductor fabrication technology, many of these functional components have been deeply studied and well developed[18]–[28]. The proposed integrated optical system is now well known as the photonic integrated circuits.

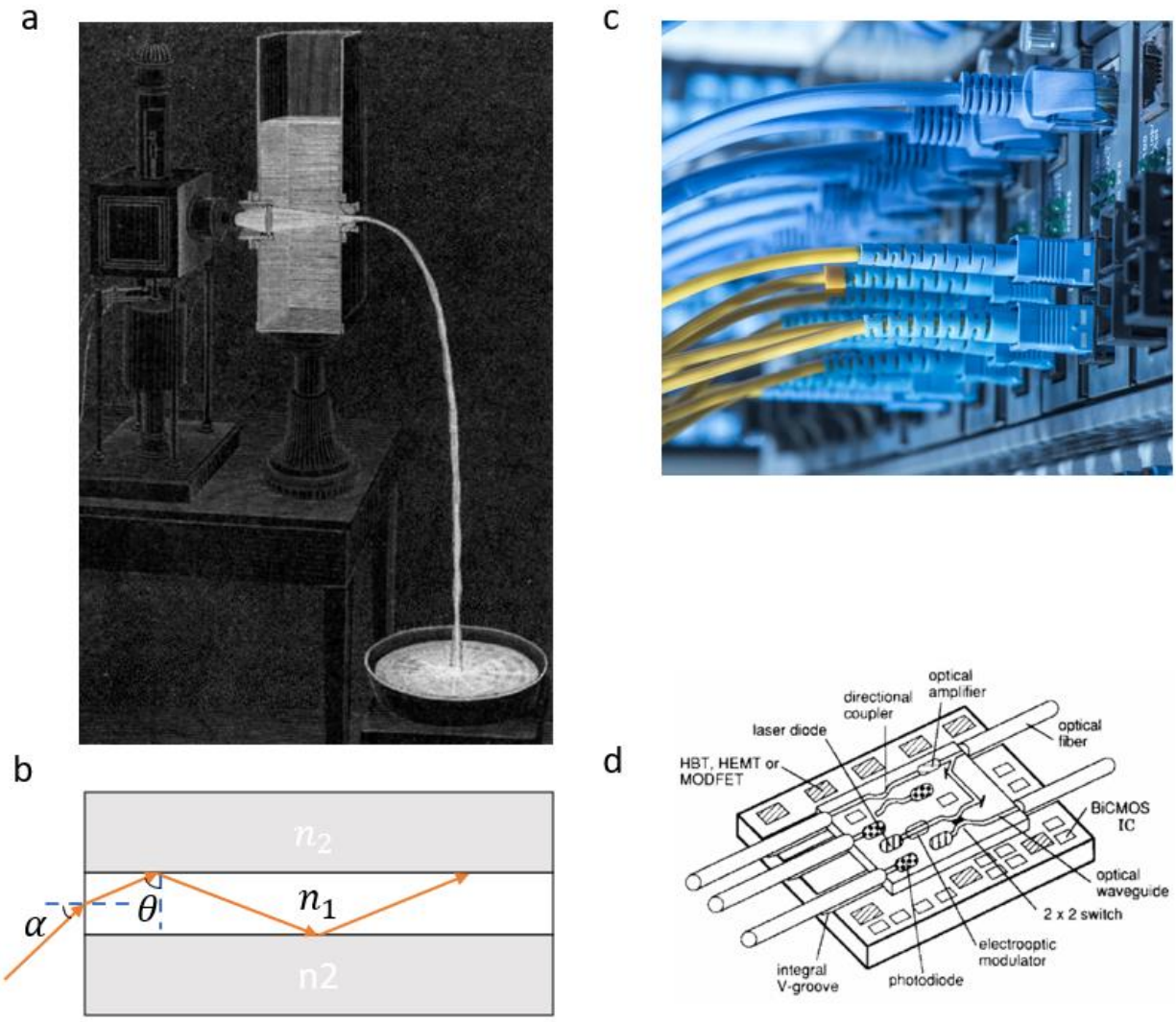

Figure 1.1 **Historical Review of Fiber Optics and Photonic Integrated Circuits.** a) The "light fountain" experiment demonstrated by Daniel Colladon and Jacques Babinet in the early 1840s. b) The schematic of total internal reflection ($\theta > \arcsin(n_2/n_1)$). c) Fiber optical communication systems. d) the optical super-chip proposed in 1970s that contained laser diodes, waveguides, optical amplifiers, electro-optical modulators, directional couplers, and receivers all in one chip[17].

1.1.2 *Recent progress of PIC*

Photonic integrated circuits share the same principle as optical fibers. The primary element is the optical waveguide composed of a sub-micron core of high refractive index and a cladding of

low refractive index. The optical waveguides support one or more propagational modes whose electromagnetic fields are tightly confined in the core and evanescently decaying in the cladding. Like optical fibers, integrated waveguides support two different sets of modes. The TE-like modes have electrical fields in the transverse direction that is parallel to the surface of the substrate. The TM-like modes have electrical fields in the vertical direction that is perpendicular to the surface of the substrate. Photonic integrated circuits have many advantages over electronic integrated circuits[29]. First, the optical loss of photonic waveguide is much lower than the electrical circuits, simply because there is no resistance for light. Second, the information capacity of optical waveguides is much larger than the electrical connection owing to the large communication bandwidth and naturally low crosstalk between channels. Third, photonic waveguides are naturally robust for noise from the widely exist electromagnetic background. Moreover, unlike electronic integrated circuits that are dominated by silicon, photonic integrated circuits have been developed in varieties of platforms and produced different applications based on their unique properties. For example, two mature platforms are silicon-on-insulator and InP. The silicon-on-insulator (SOI) platform is suitable for passive photonic integrated circuits owing to its low optical loss and high information volume[30], [31]. Owing to its excellent CMOS manufacturing compatibility, the SOI-based photonic circuits have played an essential role in the data transfer between microprocessors. Silicon photonics has result in many applications benefiting from its advantages of mature fabrication technique; however, the indirect bandgap of silicon limits its ability to integrate active components like lasers, amplifiers, and photodetector. The direct bandgap of InP, on the contrary, makes it an excellent platform for active devices like high-energy-efficiency quantum well lasers[34]–[37], optical amplifiers [34]–[38], detectors[39]–[42] as well as a range of passive components for creating interferometers, combiners and modulators.

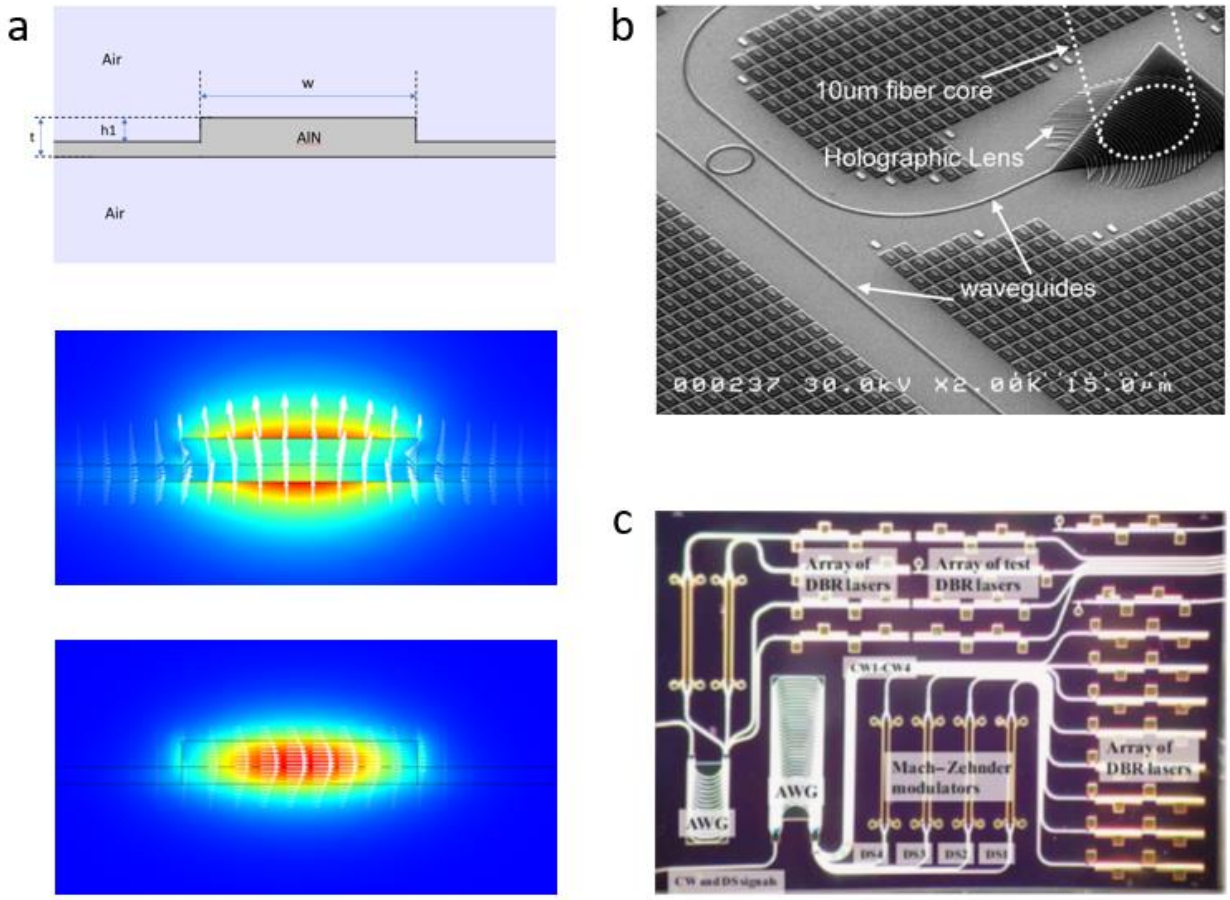

Figure 1.2 **Principle of the Index Guiding of Photonic Waveguide and Applications of Photonic Integrated Circuits on Telecommunication**. a) The cross-section of an aluminum nitride rib waveguide is shown on the top image. The thickness of the aluminum nitride film is t= 330 nm. The etching depth is h_1 = 220 nm. The width of the waveguide is about 2 μm. The middle (bottom) figure shows the fundamental TM-like (TE-like) mode in the rib waveguide. The colormap and the arrow surface represent the mode profile and the electrical filed at grid points, respectively. b) Microscope image of a commercial silicon photonic integrated circuit with waveguides, grating couplers, and micro ring resonators[32]. c) An example of InP integrated photonic circuits with DBR lasers, arrayed waveguide grating, Mach-Zehnder modulators all in one chip[33].

The InP-based photonic chips integrated distributed feedback laser diodes with electro-absorption modulators have been widely used in fiber-optic communication systems[33]. Nowadays, more

functionality of integrated photonics based on novel platforms has been developed in academia. By combining silicon photonic devices with two-dimensional materials like graphene and black phosphorus[43], high-speed photodetectors[44]–[47] and modulators[48]–[50] have been demonstrated. By integrated together with the phase-changing materials, silicon photonic has also been demonstrated as a good platform for neural network computing[51]–[53]. Compared with current electrical circuits, optical computing is potentially faster and more power-efficient. Photonic integrated circuits fabricated on aluminum nitride have not only the potential to integrate directly with silicon microchips benefitting from its excellent CMOS compatibility but also the feasibility to fabricate integrated acousto-optical and cavity optomechanical devices because of its strong piezoelectricity[54]–[58]. Moreover, the large bandgap and strong optical nonlinearity[59], [60] made it an excellent platform for photonic applications from mid-infrared to ultra-violet[61]–[63]. By embedding SAW transducers with the photonic integrated circuits, efficient on-chip acousto-optic modulation has been achieved[58], [64]. Lithium niobate is famous for its good electro-optical effect and nonlinear optic effect, and its lack of effective dry etch process for making low-loss waveguides[65], [66] has been solved recently. The photonic circuits built on lithium niobate performed well on microwave photonics applications including second harmonic generation[67], electro-optic modulation[68], [69], electro-optic frequency comb generation[70], acousto-optic frequency shifters[71] and acousto-optic frequency comb generation[72]. Besides applications in classical signal processing and communication, photonic integrated circuits also played an important role in the quantum regime. Photonic nanobeams fabricated on the diamond has been used as the communication channel for coherent interaction between photons and NV centers[73]–[77]. In general, photonic integrated circuits are playing a more important role recently both in fundamental research and applications.

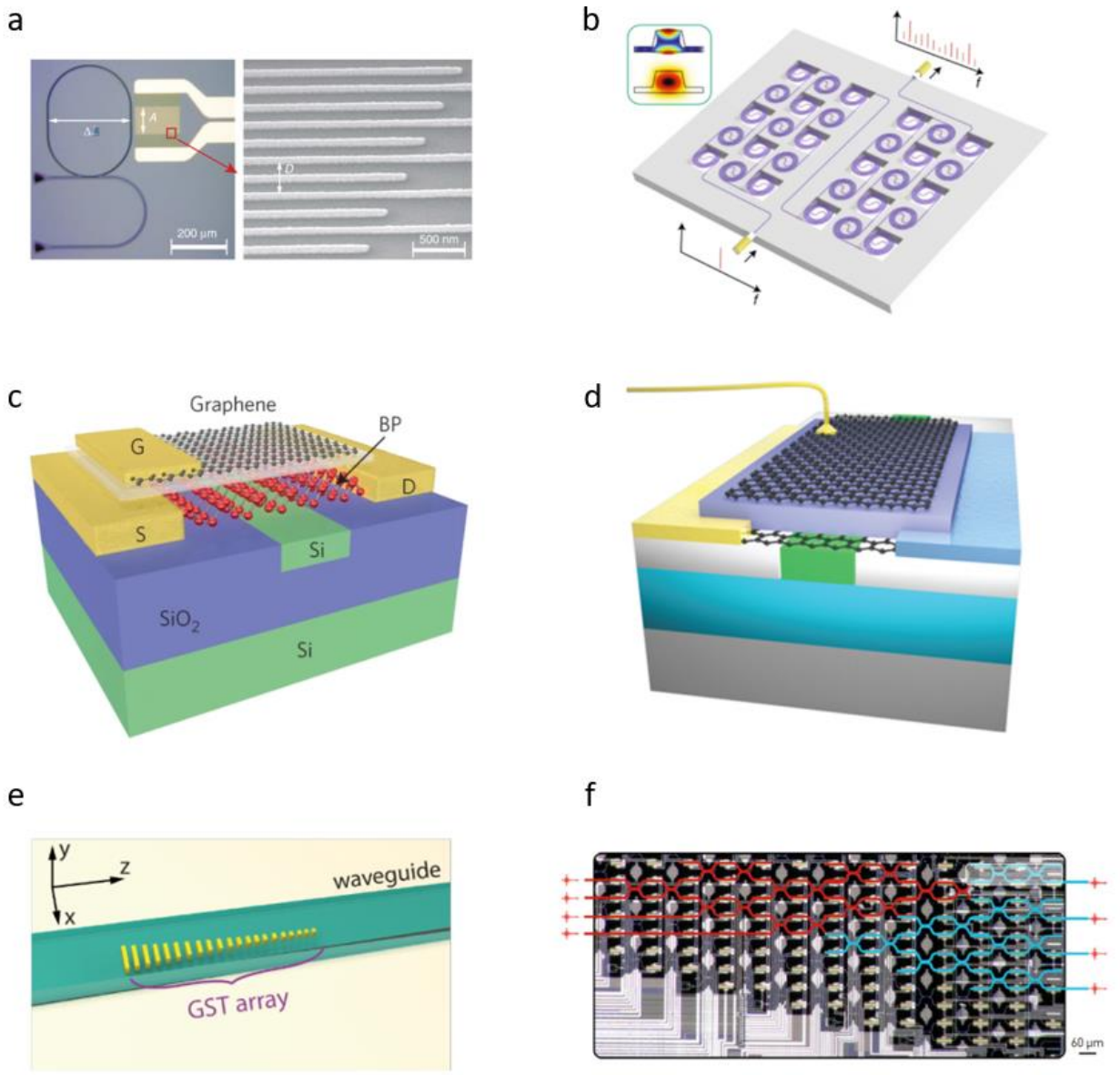

Figure 1.3 **Recent Research Progress on Novel Functional Devices based on Photonic Integrated Circuits.** a-b: mechanical modulation of photonic integrated circuits. a) acousto-optic modulation of an optical ring resonator with sub-optical wavelength acoustic wave[58]. b) Deep phase modulation based-on nanomechanical-photonic waveguide. c-d: photonic integrated circuit with 2D materials. c) high-speed black phosphorus optoelectronics based on silicon photonic circuits. d) multi-functional graphene modulator and photodetector integrated with silicon waveguide. e-f: optical computing based on photonic integrated circuits. e) optical computing based on phase-changing material integrated on silicon waveguide. b) multi-functional neural network based on large scale silicon photonic circuits.

1.2 A BRIEF REVIEW OF SURFACE ACOUSTIC WAVE

1.2.1 *Introduction to surface acoustic wave*

The existence of surface acoustic waves (SAW) was predicted by Lord Reighlay[78] in 1885 and had been widely studied in seismology. The first excitation of a single-mode surface acoustic wave was achieved by R. M. White and F. W. Voltmer[79], [80], who fabricated the interdigital transducers on piezoelectric materials. The AC signal is added to the interdigital transducers, which are metal electrodes with spatial periodicity deposited on the surface of the piezoelectric material. The harmonic vibration of the external electrical field induced mechanical vibrations at the same frequency. The acoustic modes matching both the frequency and the spatial periodicity of the electrical field are strongly excited. The interdigital transducers are not only widely used for surface acoustic wave generation due to the large overlap integral between the displacement field of the surface acoustic wave and the electrical field, but also used to generate other pseudo-SAW modes like the leaky surface acoustic wave, the surface-skimming bulk wave, and the surface transverse wave[79]. Those different modes which are distinguishable from their dispersion curve highly increased the bandwidth of the SAW devices.

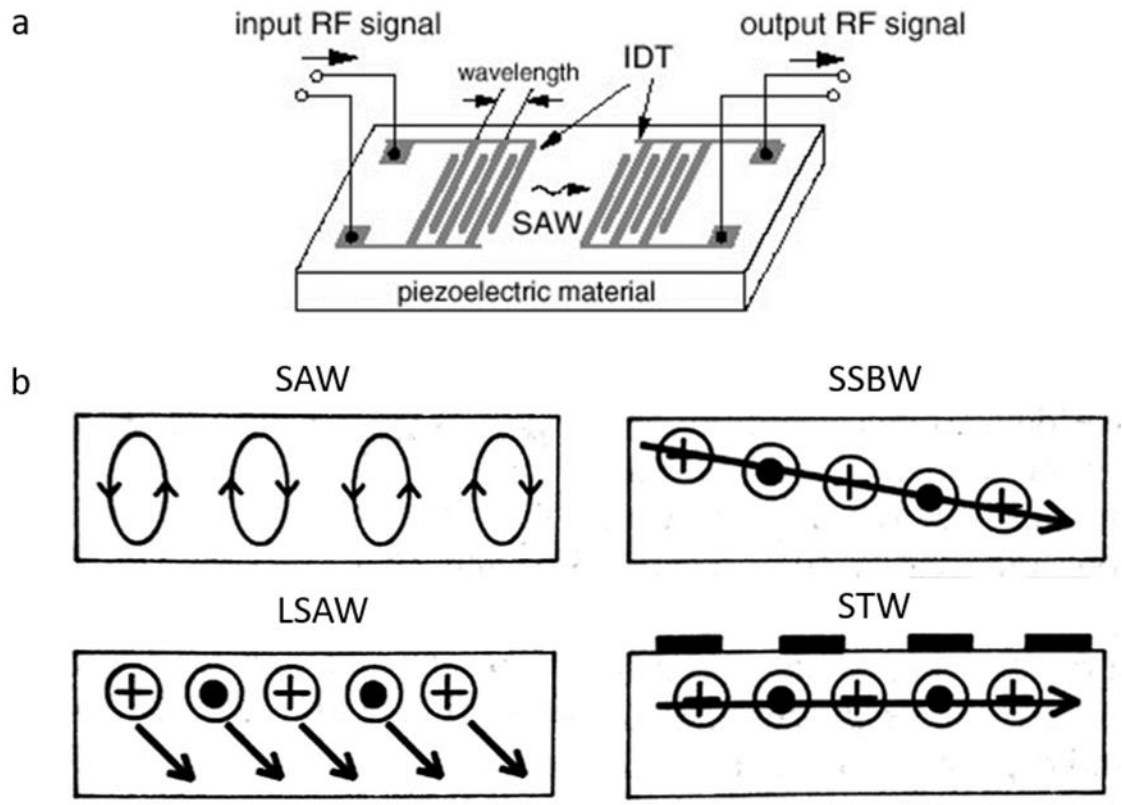

Figure 1.4 **The Fundamental of Surface Acoustic Wave Devices.** a) a typical SAW device. b) Four types of SAW and Pseudo-SAW modes are generated by an interdigital transducer.[79]

1.2.2 *Applications of surface acoustic wave devices*

In a surface acoustic wave device, an appropriate AC voltage is applied to the transducer converting of the electrical signal into mechanical vibrations. The mechanical vibration propagates out as surface acoustic waves and then reversely coupled to the receiver, and thus the mechanical energy is converted back to an electrical signal again. The electronic industry quickly recognized that such a piezoelectrical conversion process is equivalent to an electrical filter working at SAW frequency[81]–[84]. Because sound travels much slower than the electromagnetic wave, surface acoustic waves at radio and microwave frequencies have wavelengths at the micron range, which is much smaller than the wavelength of electromagnetic waves. The surface acoustic wave filters were quickly used as intermediate-frequency (IF) filters to instead bulky LC lump circuit filters in

TV receivers. The same advantage made the SAW filter one of the key components in modern high-speed wireless communication [85]–[87]. With the increasing demand in wireless communication in recent years, other similar piezoelectrical resonators have been invented, aiming to different frequency range and applications, including bulk acoustic wave (BAW) resonators[88]–[90] and thin-film bulk acoustic wave resonators (FBAR). Typically, in the commercial market, SAW and pseudo-SAW devices are built on LiNbO3 and LiTaO3. Bulk acoustic resonators are built on quartz crystal. Thin-film bulk acoustic resonators are used on aluminum nitride and zinc oxides membranes. It should be noted that SAW devices are also widely used in biosensors[91], [92], and chemical sensors[93]–[95] in medical research and working as microfluid actuators[96], [97]. The devices for those applications are working at kHz to MHz frequency range, which is much lower than the frequency of our devices; thus, we are not to introduce the details.

1.3 RECENT RESEARCH ON SURFACE ACOUSTIC WAVES

Surface acoustic wave devices have already played an important role in wireless communications; however, they were mostly considered as equivalent electrical components without deep exploring and modifying their properties. Recently, many nanomechanical devices based on surface acoustic waves have been invented with combination with photonic crystal cavities[57], [98], color centers[99], [100], or superconducting qubit[101]–[104]. Moreover, similar to the total internal reflection from Snell's Law, acoustic waves with lower sound velocity encountered total internal reflection at an interface with high sound velocity material when reaching a certain incident angle. The index-guiding property allows the fabrication of subwavelength acoustic waveguides on a certain platform. The phononic integrated circuits for a guided surface acoustic mode at hundreds of megahertz frequency containing waveguide and a

ring resonator was first demonstrated on the GaN-on-Sapphire platform with focusing IDTs as the source[105]. The concept was then developed to other platforms like LiNbO3-on-Sapphire[106] and more functionality of integrated phononic circuit devices is under exploration.

1.4 A BRIEF REVIEW OF ACOUSTO-OPTICS AND BRILLOUIN SCATTERING

1.4.1 *Principle of the Brillouin scattering*

The inelastic scattering of photons with acoustic phonons is well-known as Brillouin scattering after first predicted in theory by Leon Brillouin in 1922[107]. The macroscale mechanical fluctuations in liquids or solids would modulate the refractive index through the photoelastic effect. A simplified model, as Brillouin did in his first analysis, is to treat both light and the mechanical vibration as harmonic waves. The sinusoid acoustic wave propagates along with the solid-state system and works as a moving grating of small perturbation of the refractive index. Similar to the Bragg diffraction via a normal grating, when the angle between the incident light and sound is specially chosen, the constructive interference of the light beams reflected off the crests of the sound waveforms maximum light reflection toward a special direction. This angle is called the critical angle. Since the phase velocity of sound is so small compared to that of light, for purposes of analysis, we can still assume the sound to be a standstill grating. The critical angle is then calculated from Bragg's law: $\lambda = 2\Lambda \sin(\Phi_B)$. Here, λ is the optical wavelength, Λ is the acoustic wavelength. Φ_B is the predicted critical angle. The only difference between the sound and a normal static grating, according to Brillouin, is to impart a Doppler shift of the reflected light frequency. If the incident light is reflected toward the same direction of the acoustic wave, reflected light is blue-shifted to a higher frequency. And reversely, if the incident light is reflected toward the opposite direction of the acoustic wave, reflected light experiences a red-shift. From the

quantum mechanical point of view, Brillouin scattering is able to happen only when energy and momentum are conserved. Energy conservation results in the frequency shift of photons, while momentum conservation results in the existence of the critical angle.

1.4.2 *The exploration of Brillouin scattering*

Brillouin scattering was first experimentally observed in 1932 by Debye and Sears[108], and Lucas and Biquard[109] separately. Debye and Sears directed a beam of light upon a column of sound generated by a quartz transducer. The angle between light and sound was adjusted by continuously rotating the quartz crystal in one direction, and the deflected pattern with different angle was then monitored. They confirmed that “under favorable conditions as to the intensity of the (acoustic) vibration, more than ten spectra to the right and to the left (of the zero-order light) have been obtained”. Since the sound was generated by an oscillator with known frequency, and the wave could be obtained from Bragg's law, Debye and Sears calculated the sound velocity in quartz. The existence of the multiple order of deflected light, however, had not been well explained. In 1941, Osterhammel[110] showed that even close to the acoustic transducer, where the wavefronts are reasonably flat, there existed appreciable variations of amplitude due to Fresnel diffraction. And the mixture of acoustic wavefronts in different directions finally resulted in the observation of multiple critical angles. Another delicate experiment for the demonstration of Brillouin scattering was done by Schaefer and Bergmann in 1934[111]. Quartz was used as the platform, and acoustic waves are generated from LiNbO3 transducers cemented at the corner of the specimen. Since the transducer was located at the corner of the specimen, ultrasonic acoustic waves were generated and propagated in all directions. The specimen was illuminated with monochromatic light, and the resulting diffracted beams were focused on the back focal plane of a lens. The beautiful pattern on the focal plane is shown in Figure 1(b). Because the back-focal

plane image is the Fourier

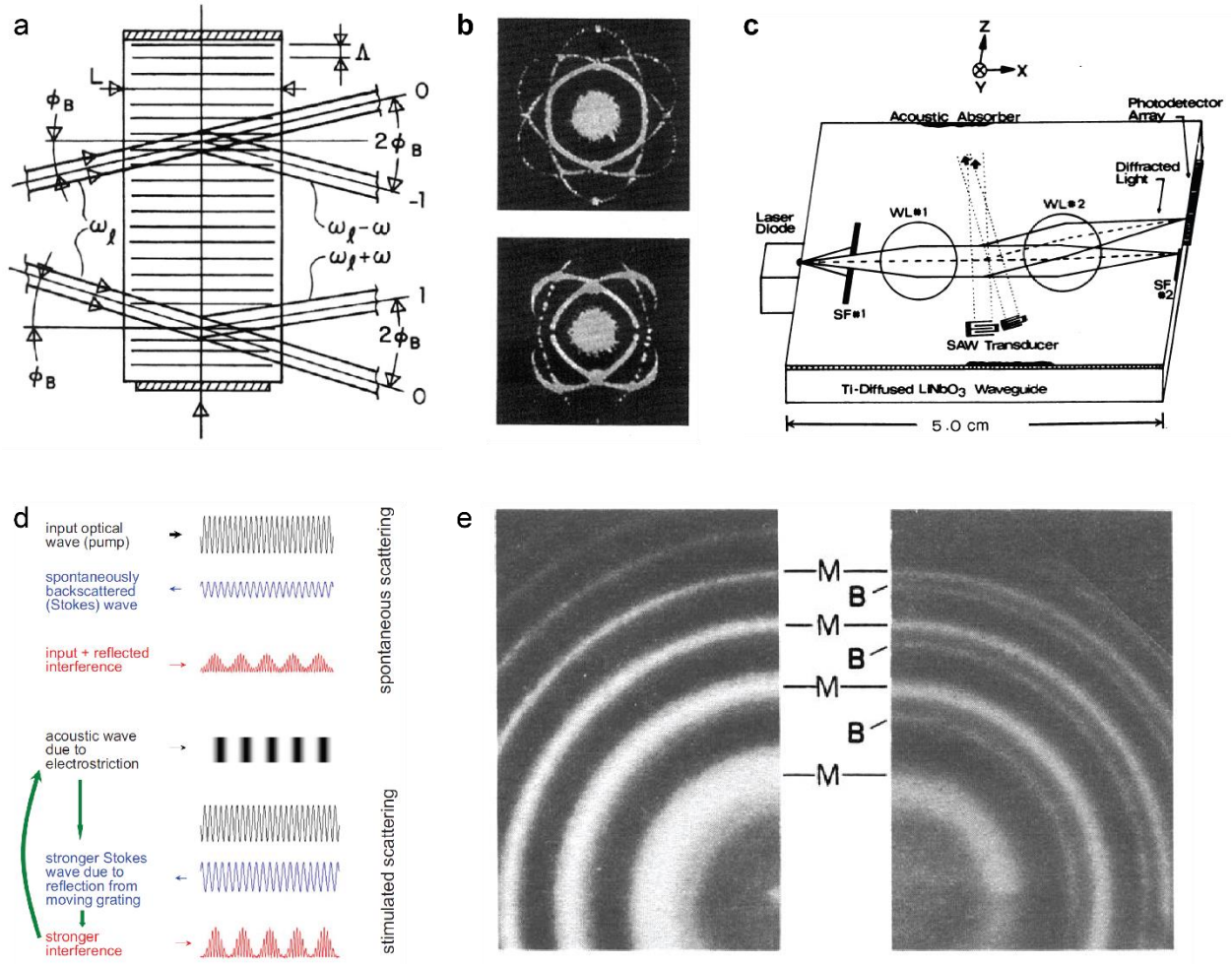

Figure 1.5 **Historical Review of Brillouin Scattering**. a. The first model of Brillouin scattering was presented by Léon Brillouin in 1922[107]. b. The back focal plane image of light is scattered by phonons in a quartz crystal done by Schaefer and Bergman in 1934[111]. c. The schematic of the acousto-optic spectra analyzer[110]. d. A comparison of spontaneous Brillouin scattering and stimulated Brillouin scattering[112]. e. Fabry-Perot interferograms of laser and of Brillouin scattered radiation from quartz.

transform of the incident wave, each of the bright spots corresponds to one phase-matching sound mode with a specific wavevector. The Schaefer-Bergmann pattern directly showed that only acoustic waves satisfying the specific critical angle could deflect the light efficiently.

1.4.3 *Development of stimulated Brillouin scattering*

The character of Brillouin scattering changed completely from scientific observation to a useful technology in the 1960s after the invention of lasers. The demands of operation for coherent light beams, for instance, deflecting them, inspired applications of Brillouin scattering. As photons have no charge, it is obvious that this can only be achieved by directly varying the refractive index through the electro-optic effect, or indirectly through the acousto-optic effect. Applications like acousto-optical frequency analyzer[113], the acousto-optic modulators[110], optical heterodyne signal processing[110], [114]–[117], large bandwidth beam-steering scanner[118], [119] and Bragg diffraction imaging of the surface acoustic wave[120] was developed. It was at the same time, stimulated Brillouin scattering (SBS), whereby intense light stimulates coherent acoustic phonons with electrostriction and radiation pressure, which come back to modulate the refractive index through photo-elastic effect and results in a strong Brillouin signal, was exploited[121], [122]. The first experimental observation of SBS was obtained in quartz with intense pump light from a Ruby laser by R. Y. Chiao and C. H. Townes in 1964[121]. Light generated by a ruby laser was focused on a quartz crystal by an objective lens. The back-reflected light was then collimated from the same lens and sent to a Fabry-Perot etalon. The maximums of interference of a Fabry-Perot etalon locates at angle α, which is dependent on the optical wavelength that $2d\ cos\ \alpha = m\lambda$. As shown in the left image of Figure 5(e), when the intensity of light is weak, the back reflected light only has the frequency component of laser wavelength. As the intensity of light kept increasing, another bunch of circles indicates for light with longer wavelength and lower frequency were observed. This phenomenon demonstrated that when light incident to the quartz crystal reached a certain threshold, the Brillouin scattering signal was rapidly amplified. The principle of SBS is shown in Figure 5(d)[112]. A small signal is generated with spontaneous Brillouin

scattering of the pump laser. The slow varying envelope of optical intensity resulting from beating between the signal and the pump then excites acoustic waves through the electrostriction. SBS happens when pump light reaches the threshold that the generating of an acoustic wave is the same as the acoustic decay rate. Starting in the 1990s, SBS was widely studied in optical fibers. A lot of technologies such as Brillouin lasers[123], [124], sensors[125], [126], SBS SL based true-time delay for RADARs[127], [128], all-optical signal processing and monitoring[129] and optomechanical oscillators were developed. Later in early 2000, SBS was characterized in photonic crystal fibers[130], where the strong confinement of the optical and acoustic modes provides strong photon-phonon interaction for exploiting SBS.

Recently, reinventing stimulated Brillouin scattering and the acousto-optic devices based on the traditional definition of Brillouin scattering on the integrated photonic platforms have drawn large research interest. The research on stimulated Brillouin scattering mainly focused on increasing the Brillouin gain and integration of multi-functional electro-optical devices. Compared with fibers and bulk materials, integrated photonic circuits provide more flexibility in the design of both the optical modes and the acoustic modes. Three different schemes have been demonstrated, the inter-mode forward scattering, the intra-mode backward scattering, and the inter-mode backward scattering. The inter-mode forward scattering, however, is most popular. Integrated SBS devices have been built on silicon[28], [124], silicon nitride[131], chalcogenide glass[132] and arsenic trisulfide[133], resulting in significant applications including Brillouin amplification and lasing[124], [130], tunable microwave filters[132], and frequency combs[134]. At the same time, the research on acousto-optic devices also revived. For example, the research on cavity-optomechanics proved that the mechanical vibrations strongly modulate the optical resonance through the photoelastic effect and boundary movement. In cavity-optomechanics,

mechanical vibration is highly localized. The surface acoustic wave, on the contrary, introduces remote modulation of the optical cavity. That means the surface acoustic wave can modulate multiple cavities together and coherently within the acoustic propagation length.

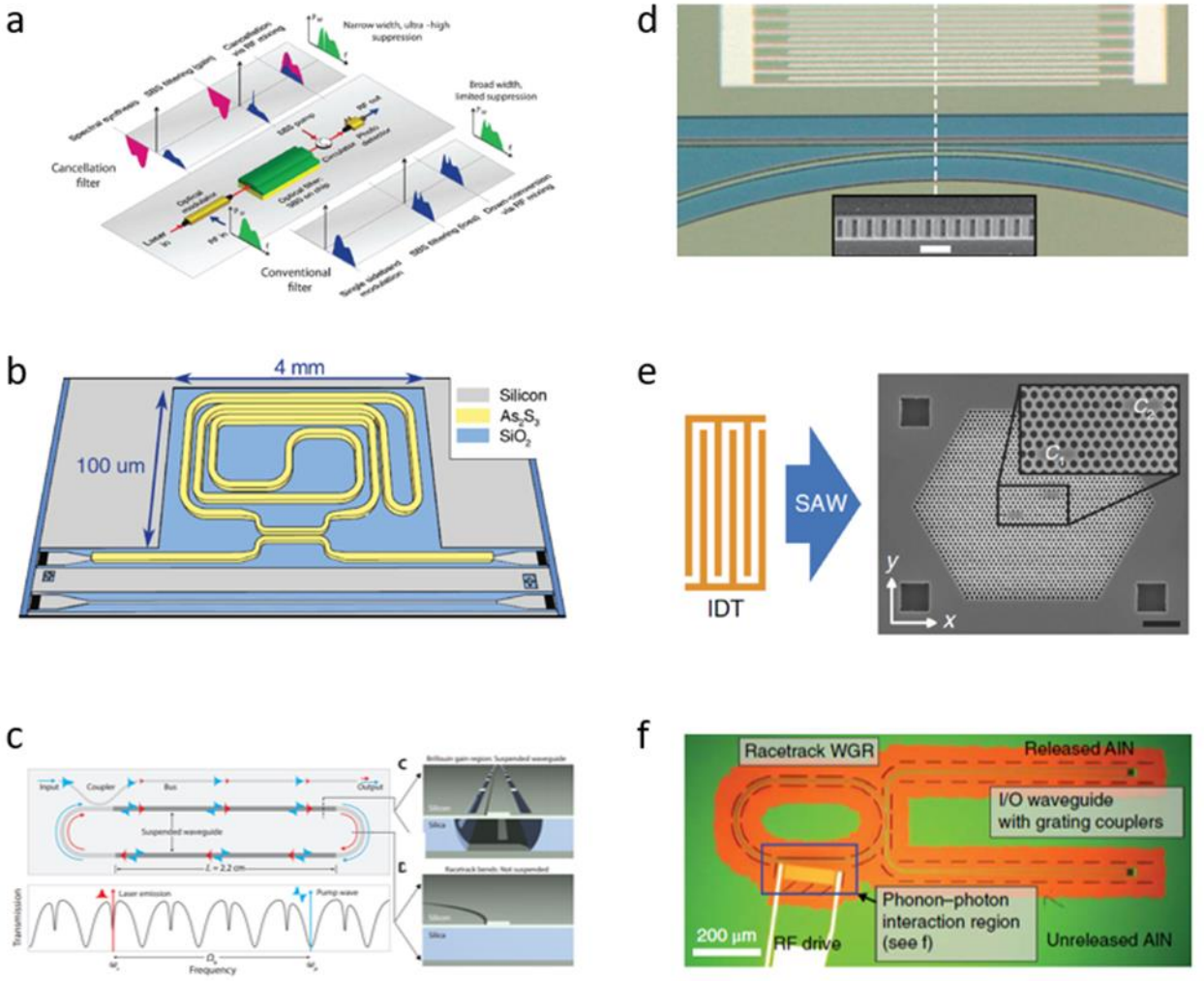

Figure 1.6 **State-of-Art Research on Stimulated Brillouin Scattering** (a-c) and the acousto-optics (d-f). a) tunable microwave notch filter based on SBS in chalcogenide glass [27]. b) Compact SBS devices through hybrid integration on silicon [28]. c) A silicon Brillouin laser based on SBS in ray-trace resonator [18]. d) acoustic modulation of the photonic crystal cavity with Lamb wave at microwave K band[64]. e) Dynamic acousto-optic control of two strongly coupled photonic crystal cavities[98]. f) Breaking time-reversal symmetry through the acousto-optic modulation[135].

Moreover, the non-zero wave number defines the propagation direction, thus naturally encoding the phase information to the modulated cavities. The phase information determined by the acoustic propagation direction breaks the time-reversal symmetry of the optical system[135], [136]. The coherent modulation of multiple optical cavities with the breaking of time-reversal symmetry results in unique phenomena like the synthetic magnetic field[137] and topological insulator in optical systems[138]. The phenomena lead to applications like unidirectional transmission, single sideband modulation[135], [136], [139], topological protection at the same time helps us understand the topological phenomena. In the quantum mechanical point of view, surface acoustic waves are the collection of phonons which naturally work as carriers to transfer quantum information on-chip. Superconducting qubit is the most promising qubit so far for quantum computation. However, the direct read-out of the quantum information as microwave photons will introduce strong disturbance through the transmission line connected to the classical equipment. Recently, researchers are investigating a way to first transfer quantum information from the superconducting qubit and the single phonon through piezoelectrical coupling[140]–[142]. Since the phonon is non-localized that finally propagates further away from the superconducting qubit, the information is picked up by input photons with optomechanical coupling.

1.5 CONTENT OF THE DISSERTATION

My Ph.D. project focused on realizing function acousto-optic devices by combining nanophotonic and nanophononics. The outline of the dissertation is presented as follows.

In Chapter 1, An introduction of the background of my research, including photonic integrated circuits, surface acoustic waves, and Brillouin scattering.

In Chapter 2, I will focus on membrane acoustics. Starting from the theory of linear elasticity and piezoelectricity, I will introduce the membrane acoustic modes, especially Lamb modes. Theoretical analysis, numerical simulation, and the experimental characterization of acoustic devices on aluminum nitride are included.

In Chapter 3, I will talk about the electromechanical Brillouin scattering. I will discuss the details of the theory in 1D Brillouin scattering, the simulation, and device design, and the fabrication and experimental results. The project is important because it inspires the invention of the hybrid platform for nanophotonics and nanophononics.

In Chapter 4, I will talk about the current project on the subwavelength photonic waveguide. Parabolic horns with different shapes are designed for the optimization of acoustic coupling from membrane mode and subwavelength waveguide. The acoustic transmission explored by S21 measurement is carefully analyzed. The visualization of the Lamb wave profile compared with FEM simulation is applied for a deep understanding of the process.

In Chapter 5, I will talk about further optimization of the electromechanical Brillouin scattering devices, including optimization of the design and fabrication process. I will also talk about other potential platforms that may help overcome the current problems, as well as other designs.

Chapter 2. FUNDAMENTAL OF SURFACE ACOUSTIC WAVES

Acoustic waves are the propagation of mechanical vibrations existing in all mediums. There are generally two categories of waves in solid bulk materials. The first set of modes are body waves propagating in the interior of the bulk materials, which are identified by its propagation direction (k_x, k_y, k_z) and frequency (f). When the displacement field is along with the propagation direction, the waves are called primary waves (p-wave) or longitudinal waves. On the other hand, if the displacement field is perpendicular to the propagation direction, the waves are called secondary waves (s-wave) or shear waves. The other set of waves is surface waves propagating on the surface of the solids, which are identified by its propagation direction (k_x, k_y) and frequency (f). The power of the surface acoustic wave concentrates on the surface and exponentially decays to the depth of the material. There are also two types of surface acoustic waves. The first one is called the Rayleigh wave; whose displacement field concentrates in the plane determined by the propagation direction and surface normal. The second type is called the Love wave (SH wave), whose displacement field is perpendicular to the surface normal. In our situation, both the mechanical deformation and the electrical polarization are in the linear regime. So, we applied the linear model for both elasticity and the piezoelectricity analysis. In the theory part, we applied the summation convention of tensors to simplify our expression.

2.1 LINEAR ELASTICITY

In solid mechanics, the body is described as a continuous geometrical model whose geometrical points indicate the infinitesimal material particles. The deformation of the body is described by the mapping of the body from the original state to the deformed state. Consider an infinitesimal line element connecting the point $P(x_1, x_2, x_3)$ and $Q(x_1 + dx_1, x_2 + dx_2, x_3 +$

dx_3) In the original body. They are mapped into the point $P'(x_1', x_2', x_3')$ and $Q'(x_1' + dx_1', x_2' + dx_2', x_3' + dx_3')$. The change of the length of the infinitesimal line describing the deformation is expressed by the following formula

$$P'Q' - PQ = dx'_i dx'_i - dx_i dx_i$$

$$= \left(\frac{\partial x'_i}{\partial x_j}\frac{\partial x'_i}{\partial x'_k} - \delta_{jk}\right) dx_j dx_k$$

The deformation is fully described by the second-order tensor

$$s_{ij} = \frac{1}{2}\left(\frac{\partial x'_i}{\partial x_j}\frac{\partial x'_i}{\partial x'_k} - \delta_{jk}\right)$$

known as the Green's strain tensor. The Green's strain tensor can be simplified by defining the displacement field $u_i = x'_i - x_i$, Thus

$$s_{ij} = \frac{1}{2}\left(\frac{\partial u_i}{\partial x_j} + \frac{\partial u_j}{\partial u_i} + \frac{\partial u_\alpha}{\partial x_i}\frac{\partial u_\alpha}{\partial x_j}\right)$$

We are working on the infinitesimal strain approximation that the higher-order term in the Green's strain tensor, well-known to cause difficulties in solving elastic problems, is negligible.

Consider a small surface element of area ΔS with unit normal vector $\boldsymbol{\nu}$ on an imagined surface S of the solid. A force ΔF is applied to the surface element. The stress at this point in the direction $\boldsymbol{\nu}$ is defined as:

$$\boldsymbol{T^{\nu}} = \frac{\Delta \boldsymbol{F}}{\Delta S}$$

With respect to the surface normal, the coaxial component of T is called the normal stress, while the other two components are called shearing stresses. Like strain, due to the freedom of both surface element and the force, the stress is fully described by a second-order tensor $\boldsymbol{\sigma}$. In a coordinate system, σ_{ij} is defined by the derivative of the force in x_i direction with respect to

surface element normal to the axis x_j. Thus, the stress applied in any direction at a certain point is represented by

$$T^{\nu} = \sigma_{ij}\nu_j$$

With the definition of stress, the motion of each particle can be derived from Newton's equation of motion:

$$\rho\frac{\partial^2 u_i}{\partial t^2} = \frac{\partial \sigma_{ij}}{\partial x_j}$$

The strain and stress are the most critical concepts in elasticity. The relation between stress and strain in the linear regime is expressed by the general formation of the Hawk's Law,

$$\sigma_{ij} = D_{ijkl}s_{kl}$$

where $\boldsymbol{D}$ is the elastic moduli tensor that determines the compliance of the solid. By substituting Hawk's Law to the equation of motion, one can get the general case of wave equation:

$$\rho\frac{\partial^2 u_i}{\partial t^2} = \frac{\partial}{x_j}\left(D_{jilk}s_{lk}\right) = \frac{\partial}{x_j}\left(\frac{1}{2}D_{jikl}\left(\frac{\partial u_l}{\partial x_k} + \frac{\partial u_k}{\partial x_l}\right)\right) = \frac{\partial}{x_j}\left(C_{jikl}\frac{\partial u_k}{\partial x_l}\right)$$

where $C_{ijkl} = \frac{1}{2}\left(D_{ijkl} + D_{ijlk}\right)$ is called compliance tensor. Because both stress tensor and strain tensor are symmetric, they are typically simplified using the Voigt notation: $11 \rightarrow 1, 22 \rightarrow 2, 33 \rightarrow 3, 23 \rightarrow 4, 13 \rightarrow 5, 12 \rightarrow 6$, to six-dimension vectors $\{\sigma\}$ and $\{s\}$. The compliance tensor is then converted to a 6x6 matrix $[C]$ called the compliance matrix or elasticity matrix.

2.2 THE RAYLEIGH AND LAMB WAVE

Let us demonstrate the existence of surface waves in the xz-plane by considering the case that particles moving in the plane formed by the propagating direction $(\hat{x})$ and surface normal $(\hat{y})$ with the following expression:

$$u = Ae^{-by}\exp\big(ik(x-ct)\big)$$

$$v = Be^{-by}\exp\big(ik(x-ct)\big)$$

$$w = 0$$

where $u, v, and\ w$ are the displacement fields in $\hat{x}, \hat{y}$,and $\hat{z}$, respectively. We assume the material is isotropic and has two body waves with phase velocity c_T for the transverse mode and c_L for the longitudinal mode. The relation of A, B, k, and c is determined by the wave equation. We can get two sets of solutions:

$$b' = k\left(1-\frac{c^2}{c_L^2}\right)^{\frac{1}{2}}, \qquad b'' = k\left(1-\frac{c^2}{c_T^2}\right)^{\frac{1}{2}}$$

$$\left(\frac{B'}{A'}\right) = -\frac{b'}{ik}, \qquad \left(\frac{B''}{A''}\right) = \frac{ik}{b''}$$

It is easy to check that the longitudinal and transverse components of the displacement field have $\pi/2$ phase delay. The displacement fields form a rolling profile on the surface and penetrate exponentially into the substrate. This type of acoustic wave is known as the Rayleigh wave.

When the thickness of the body is no longer infinite, there is another set of acoustic modes called Lamb waves, named after first predicted by the English mathematician Horace Lamb[143]. Just like Rayleigh waves, Lamb waves also have a phase difference between the longitudinal and transverse components of the displacement field. The general solution of Lamb waves is quite complicated. Unlike an infinitely deep medium that only supports two sets of body modes, the longitudinal waves (P-wave) and transverse waves (S-wave), and two sets of Rayleigh modes, a membrane supports two infinite sets of Lamb waves - antisymmetric Lamb modes and symmetric Lamb modes. For the symmetric modes, the displacement field is symmetric with respect to the center plane of the membrane. For the antisymmetric modes, the displacement field is

antisymmetric with respect to the center plane. The most critical modes are the zero-order symmetrical and antisymmetric modes. These are the only two modes that have zero frequency with $k = 0$. They are also the ones with the largest overlap integral with the electrical field of the piezoelectrical transducer, and thus carry most mechanical energy.

2.3 PIEZOELECTRICITY

Surface acoustic waves can be produced in many ways. The most commonly used technique is through piezoelectric excitation. Piezoelectricity is the phenomenon that material is electrically polarized with external pressure, which was first observed by Pierre Curie and Jacques Curies in crystals like tourmaline, quartz, and topaz. The additional electrical polarization in the material due to the existence of stress is described as a simple coupling term:

$$p_{pe} = [d] \cdot \{\sigma\}$$

The electric field will also generate additional strain through Coulomb's force. Thus, piezoelectricity can be described in the following strain-charge form,

$$\{s\} = [S_E]\{\sigma\} + [d]^T\{E\}$$

$$\{D\} = [d]\{\sigma\} + [\epsilon]\{E\}$$

where $[d]$ determines the electromechanical coupling strength. It should be noted that we can also model the piezoelectricity by considering D and T as the function of E and S, which is known as the stress-charge form.

$$\{\sigma\} = [C_E]\{s\} - [e]^T\{E\}$$

$$\{D\} = [e]\{s\} + [\epsilon]\{E\}$$

For piezoelectrical transducers, the energy conversion between electricity and mechanics depends not only on d but also the electrical field distribution. So, the most critical parameter is the electromechanical coupling factor k, which is determined as:

$$k_{pe}^2 = \frac{Converted\ Mechanical\ Energy}{Input\ electrical\ Energy}$$

In the simplest case, the piezoelectric material is sandwiched between two electrodes, and the electromechanical coupling factor k can be simply calculated as

$$k_{33}^2 = \frac{d_{33}^2}{\epsilon_{33}^T s_{33}^E}$$

However, in most cases like surface acoustic wave transmitters, both the electrical field distribution and the acoustic mode profile are complicated. Moreover, instead of all converted to the desired surface acoustic wave, some of the electrical power is converted to other local dissipative mechanical modes. Thus, the dissipation of electromagnetic energy by conversion to mechanical vibrations is always modeled as an equivalent circuit added to the electric circuits.

2.4 PHOTOELASTICITY

Because we are going to integrate phononic components with photonic devices, we shall also introduce the photoelasticity. Photoelasticity describes the change of refractive index under mechanical deformation. Because both the permittivity matrix and the strain matrix are second-order tensors, the photoelasticity is described by the fourth-order tensor:

$$\Delta(\epsilon)_{ij}^{-1} = P_{ijkl} s_{kl}$$

Similar to the elastic matrix, we can rewrite permittivity and strain to six-dimension vectors and the photoelastic tensor to a six-by-six symmetric matrix by applying Voigt notation.

2.5 SURFACE ACOUSTIC WAVE TRANSDUCER

The key component of the surface acoustic wave transmitter is the interdigital transducer (IDTs), which is composed of two interlocking combo-shape electrodes. The simplest design of IDTs is two arrays of electrodes, so-called IDT fingers, with constant periodicity. AC electrical signal added to the electrode converts to mechanical vibration at the same frequency. The periodic structure of IDT fingers can enhance the electromechanical conversion efficiency of all mechanical vibration with the same spatial periodicity through constructive interference and suppress excitation of all other mechanical vibration mismatching the spatial periodicity. The mechanical modes with frequency f and spatial periodicity k are often propagational acoustic modes. Though IDTs are also used for bulk waves or pseudo-surface waves generation, due to the high concentration of the displacement field near the surface, which has the maximum overlap integral with the input electrical field, IDT's are most efficient in generating surfaces acoustic waves modes like Rayleigh modes and Lamb modes. There are different equivalent circuit models for FBAR, BAW, and SAW transducers. The typical way to model SAW transducers is shown in Figure 2.1b. To have a better understanding of why the SAW excitation is equivalent to the additional electrical load, I am going to introduce the coupling-of-mode theory of surface acoustic wave transducers.

2.6 THE COUPLING OF MODE ANALYSIS

In the IDT fingers region, the forward propagation acoustic mode and the backward propagation acoustic mode couple to each other through the reflection at the edges of the metal. At the same time, they are both electromechanically coupled to the input microwave signal. Because the wavelength of the microwave signal is about three orders of magnitude larger than the IDT fingers region, the spatial periodicity of the input microwave only depends on the period of

IDT fingers (Λ_T), which can be considered a pseudo-wavevector with wavenumber k_T=2π/Λ_T of the input microwave in this region. Without loss of generality, we assume the acoustic coupling through reflection at the boundaries of IDT fingers is small, meaning that the extra mass loading caused by metal electrodes is small. We set a_1, a_2, and k_0 to be the displacement fields of the forward wave, backward acoustic wave, and their wavenumbers, respectively. The phase-matching condition showed that for both the piezoelectrical excitation and the acoustic reflection, only the ± 1 components dominate the coupling process. SAW excitation process in this region can thus be modeled with the following coupling-of-mode equations based on the perturbation theory:

$$\frac{da_1}{dx} = -jk_0 a_1 + j\kappa \exp(-j2k_T x)\, a_2 + j\alpha V \exp(-jk_T x)$$

$$\frac{da_2}{dx} = j\kappa \exp(j2k_T x)\, a_1 + jk_0 a_2 - j\alpha^* V \exp(jk_T x)$$

By applying the rotation frame, and setting $\Delta = k_T - k_0$

$$\frac{d\tilde{a}_1}{dx} = j\Delta \tilde{a}_1 + j\kappa \tilde{a}_2 + j\alpha V$$

$$\frac{d\tilde{a}_2}{dx} = -j\kappa \tilde{a}_1 - j\Delta \tilde{a}_2 - j\alpha^* V$$

To get the electromechanical coupling efficiency, we need to analyze the whole impedance network near the IDT region. The acoustic excitation is embedded in the electrical circuit of the IDT as an external source. The fingers with opposite voltages compose a capacitor C_T. The resistance on each IDT finger causes an additional voltage to drop from the busbar to the capacitor and is modeled as a series resistor R_e. The acoustic waves are equivalent to an external transmission line connecting on the electrodes contributing to the current on the fingers through the inverse piezoelectric effect with efficiency η, thus can be considered as the current source in

parallel to C_T. From energy conservation, we have $\eta = 2\alpha$. Thus, the current on the busbar satisfies the following equation:

$$\frac{dI}{dx} = j2\alpha\tilde{a}_1 - j2\alpha^*\tilde{a}_2 - \frac{j\omega C_T}{\Lambda_T(1 + j2\omega C_T R_E)}V_0$$

In our case, the surface acoustic waves are fully generated through input electrical power. There is no backward propagation SAW at the front of the transmitter, and no forward propagation SAW at the end of the transmitter. The total current in the transmitter is solved with the boundary conditions, $\tilde{a}_1(0) = \tilde{a}_2(L) = I(0) = 0$. The solutions are listed here.

$$\tilde{a}_1 = \frac{4sin\left(\frac{DL}{2}\right)}{D[Dcos(DL) + j\Delta sin(DL)]}\left[(\alpha\Delta - \alpha^*\kappa)sin\left(\frac{DL}{2}\right) - j\alpha Dcos\left(\frac{DL}{2}\right)\right]V_0$$

$$\tilde{a}_2 = \frac{4sin\left(\frac{DL}{2}\right)}{D[Dcos(DL) + j\Delta sin(DL)]}\left[(-a\kappa^* - \alpha^*\Delta)sin\left(\frac{DL}{2}\right) + j\alpha^* Dcos\left(\frac{DL}{2}\right)\right]V_0$$

$$I(L) = \frac{j\omega C_T L}{\Lambda_T(1 + j2\omega C_T R_E)} + Y(\omega)$$

$$Y(\omega) = \frac{j(4\alpha^*\alpha\Delta + 2\kappa^*\alpha^2 + 2\kappa\alpha^{*2})L}{D^2} - \frac{4(-\Delta^2\alpha\alpha^* + \Delta\kappa\alpha^{*2} + \kappa\kappa^*\alpha\alpha^* - \Delta\kappa^*\alpha^2)}{D^3[Dcos(DL) + j\Delta sin(DL)]}$$

$$\cdot(1 - cos(DL)) + \frac{2(-\kappa^*\alpha^2 - 2\Delta\alpha\alpha^* + \kappa\alpha^{*2})}{D^2[Dcos(DL) + j\Delta sin(DL)]}jsin(DL)$$

$$with\ D = \sqrt{\Delta^2 + \kappa\kappa^*}$$

The total impedance of the fingers contains two terms. The first term is the pure electrical impedance, which from the expression is simply IDT resistance in series to the IDT capacitor. The second term depending only on the electromechanical coupling factor (α), the reflection of the two acoustic waves (κ), and the length (L) of the IDT corresponds to the acoustic excitation. We can thus model the acoustic response near the resonance with the following equivalent circuit. To get a clear picture, let us first consider the IDT fingers are reflectionless: $D = \Delta, \kappa = 0$.

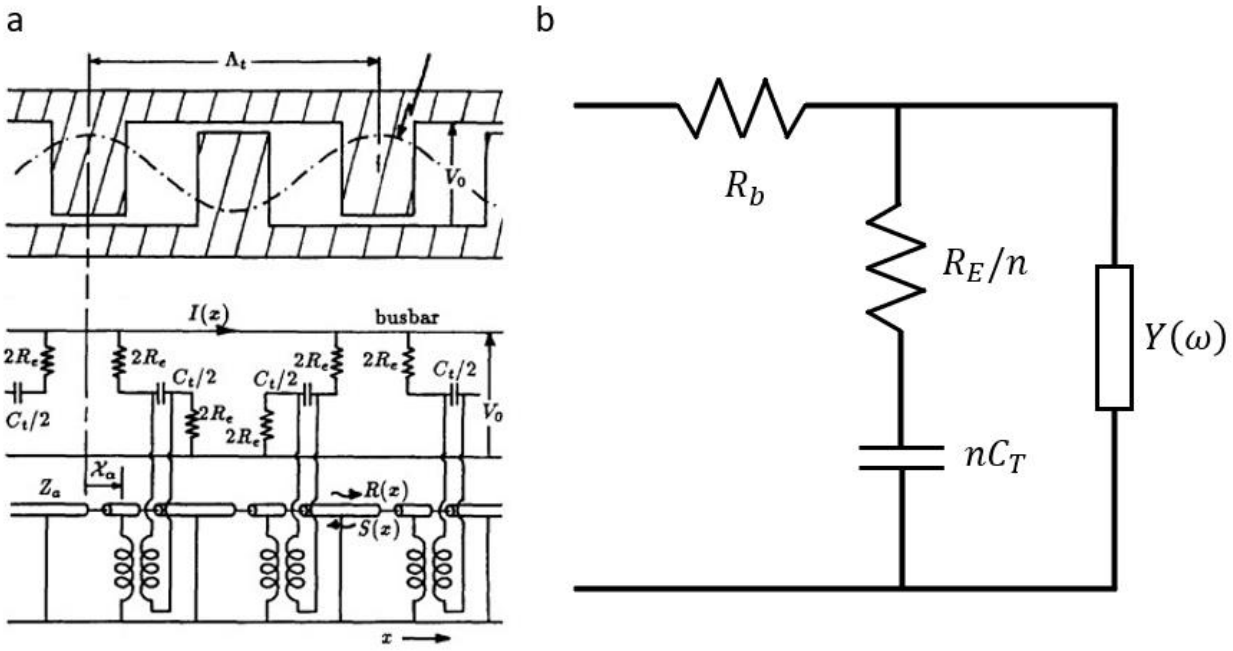

Figure 2.1 **The Equivalent Circuit Model of IDT from COM Analysis**. a) The forward and backward Lamb waves are equivalent to the electrical signal inside the transmission line. b) The resultant equivalent circuit model in the IDT fingers region. n is the number of IDT fingers, R_E and C_T are the resistance and capacitance for a single pair of IDT fingers, R_b is the resistance of the busbar.

$$Y(\omega) = \frac{4\alpha\alpha^* v_g^2}{(\omega-\omega_0)^2}\left(e^{-\frac{i(\omega-\omega_0)L}{v_g}} - 1 + \frac{j(\omega-\omega_0)L}{v_g}\right)$$

In real devices, the reflection at the IDT boundaries is not negligible. Thus, the frequency domain response of electromechanical coupling is very complicated. Fortunately, the electrical background has a simple form so that we can always fitting the background and leave the acoustic excitation impedance as an undefined impedance. The electromechanical coupling factor and the power conversion efficiency are then obtained by fitting the background near the resonance and extracting the power consumption for both the electrical circuit and mechanical conversion. Even though the equivalent circuit model is a good approximation for IDT with a large aperture, there are many undefined parameters like the acoustic reflectivity at the IDT boundaries as well as the

electromechanical coupling factor that are hard to estimate. So, we used FEM simulations to guide our design.

2.7 SURFACE ACOUSTIC WAVE DEVICES ON ALUMINUM NITRIDE MEMBRANE

Aluminum nitride is a wide bandgap (6.2 eV) semiconductor of wurtzite crystalline structure with a lattice constant: a=3.112 Å, c=4.982 Å. Its refractive index is about 2.2 for telecom band light. It has good piezoelectricity in the vertical direction due to the asymmetry. Its good CMOS compatibility compared to $LiNbO_3$ and $LiTaO_3$ makes it an excellent platform for integrated acousto-optic devices. The piezoelectric constant, stiffness matrix, and the photoelastic matrix of crystalline aluminum nitride are collected in Table (1). Because we are using c-axis polycrystalline aluminum nitride grown on silicon with magnetron sputtering in our real devices, I also list the typical stiffness matrix for aluminum nitride thin films using the same growing condition which is used in the acoustic simulations. It was widely known that adding scandium inside aluminum nitride would make it ferroelectric and increased its piezoelectricity. Recently, both academia and industry started to tap the potential of aluminum scandium nitride. We are also discovering new acousto-optic devices on the aluminum scandium nitride platform; thus, its elastic constants[144] and piezoelectricity[144] are also listed in the table.

Table 1 Elasticity, Piezoelectricity, and Photoelasticity of Selected Materials

Material	stiffness matrix (GPa)	Piezoelectric constant (strain –charge form)	Photoelastic matrix
	$\begin{pmatrix} c_{11} & c_{12} & c_{13} & 0 & 0 & 0 \\ c_{12} & c_{22} & c_{13} & 0 & 0 & 0 \\ c_{13} & c_{13} & c_{33} & 0 & 0 & 0 \\ 0 & 0 & 0 & c_{44} & 0 & 0 \\ 0 & 0 & 0 & 0 & c_{44} & 0 \\ 0 & 0 & 0 & 0 & 0 & c_{66} \end{pmatrix}$	$\begin{pmatrix} 0 & 0 & 0 & 0 & e_{15} & 0 \\ 0 & 0 & 0 & e_{15} & 0 & 0 \\ e_{13} & e_{13} & e_{33} & 0 & 0 & 0 \end{pmatrix}$	$\begin{pmatrix} p_{11} & p_{12} & p_{13} & 0 & 0 & 0 \\ p_{12} & p_{22} & p_{13} & 0 & 0 & 0 \\ p_{13} & p_{13} & p_{33} & 0 & 0 & 0 \\ 0 & 0 & 0 & p_{44} & 0 & 0 \\ 0 & 0 & 0 & 0 & p_{44} & 0 \\ 0 & 0 & 0 & 0 & 0 & p_{66} \end{pmatrix}$
AlN (wurtzite)	$c_{11} = 410; c_{12} = 149; c_{13} = 99;$ $c_{33} = 389; c_{44} = 125.$	$e_{15} = -0.33; e_{13} = -0.38;$ $e_{33} = 1.26.$	$p_{11} = -0.1; p_{12} = -0.027; p_{13} = -0.019;$ $p_{33} = -0.107; p_{44} = -0.032; p_{66} = -0.037.$
AlN (c-axis)	$c_{11} = 404; c_{12} = 143; c_{13} = 103;$ $c_{33} = 402; c_{44} = 124.$	$e_{15} = -0.3; e_{13} = -0.54;$ $e_{33} = 1.52.$	
$AlSc_{0.32}N_{0.68}$ (c-axis)	$c_{11} = 307; c_{12} = 108; c_{13} = 123;$ $c_{33} = 230; c_{44} = 110$	$e_{15} = -0.23; e_{13} = -0.69;$ $e_{33} = 2.8$	

The zero-order symmetrical and antisymmetric Lamb modes are identified by solving eigenmodes using COMSOL Multiphysics. The mode profile of S_0(A_0) mode in Figure 2.2 (a(b)). The arrow surfaces and color image show total displacement fields and y-axis displacement fields, respectively. In the long-wavelength limit, the S_0 mode looks like a "breathing mode," and the A_0 mode looks like a shear wave. In case the wavelength is comparable to the membrane thickness, both S_0 and A_0 modes showed elliptical particle motion near the membrane. This is the evidence that zero-order Lamb modes are closely related to Rayleigh surface waves. The two degenerated Rayleigh waves at the top and bottom surfaces are coupled and hybridized to A_0 and S_0 modes with frequency splitting. The dispersion curves and the mode profile of S_0, A_0, and Rayleigh also show that in the low-frequency limit, the symmetrical mode has a higher phase and group velocity with most of the mechanical energy in the center of the membrane. The antisymmetric mode, on the contrary, has a lower phase and group velocity with mechanical energy concentrating near the boundaries. In the higher frequency limit, the acoustic wavelength decreases to much shorter than the membrane thickness. The overlap between the two Rayleigh waves vanishes; thus, both the symmetrical mode and the antisymmetric mode perform like the Rayleigh wave, and so do their

dispersion curves. As will be shown in Chapter 3, we are interested when the wavelength of the Lamb modes is comparable to the membrane thickness.

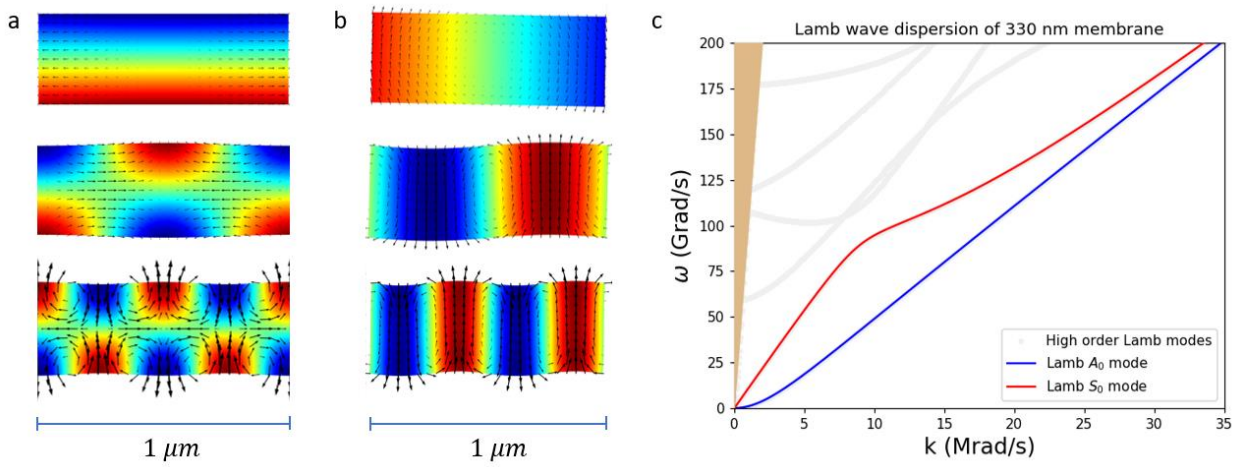

Figure 2.2 **Lamb S0 and A0 Mode Profile of 330 nm AlN**. a) displacement fields (black arrows) and y displacement (colormap) for Lamb S0 mode of 10 um (top), 1 um (middle), and 500 nm (bottom). b) displacement fields for Lamb A0 mode of 10 um (top), 1 um (middle), and 500 nm (bottom).

The acoustic waves in the IDT finger regions are much different. Due to the limitation on fabrication capability, we can only deposit electrodes on the top of the membrane. The deposited metal heavily breaks the mirror symmetry in the vertical direction. Thus, the acoustic waves in the IDT regions are not Lamb modes. The eigenmodes with different types and thicknesses of the metal are simulated. The result showed that both aluminum and gold electrodes distorted the acoustic modes in the IDT region. Aluminum performed better in maintaining the Lamb modes profile due to its lighter weight. Even with 160 nm thick electrodes deposited, the mode profile does not shift too much from Lamb waves. When gold reaches 60 nm or thicker, the Lamb-like modes are no longer generated. However, in real devices, the oxidation layer on the surface of aluminum not only increases the resistance of fingers significantly but also negatively affects the

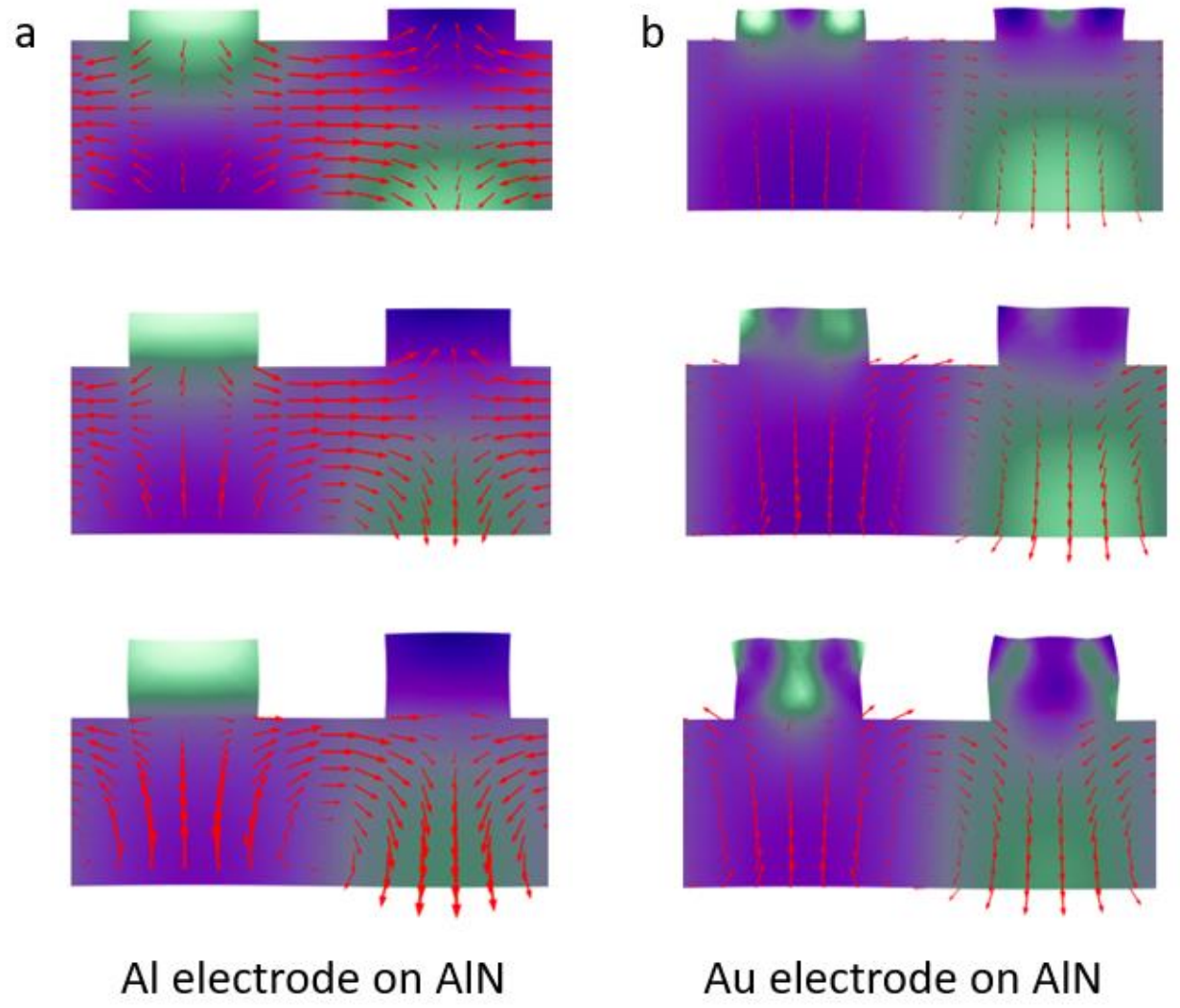

Figure 2.3 **Lamb S0 Mode in IDT Fingers Region.** The 1 μm Lamb S0 mode of 330 nm aluminum nitride distortion with different electrode thicknesses was simulated. a) aluminum fingers with a thickness of 60 nm (top), 110 nm (middle), and 160 nm (bottom). b) gold fingers with a thickness of 60 nm (top), 110 nm (middle), and 160 nm (bottom).

engagement of probes during the measurement. The deposited metal also shifts the resonance frequency; however, by scanning the parameters when designing real devices, we are always able to compensate for the drift.

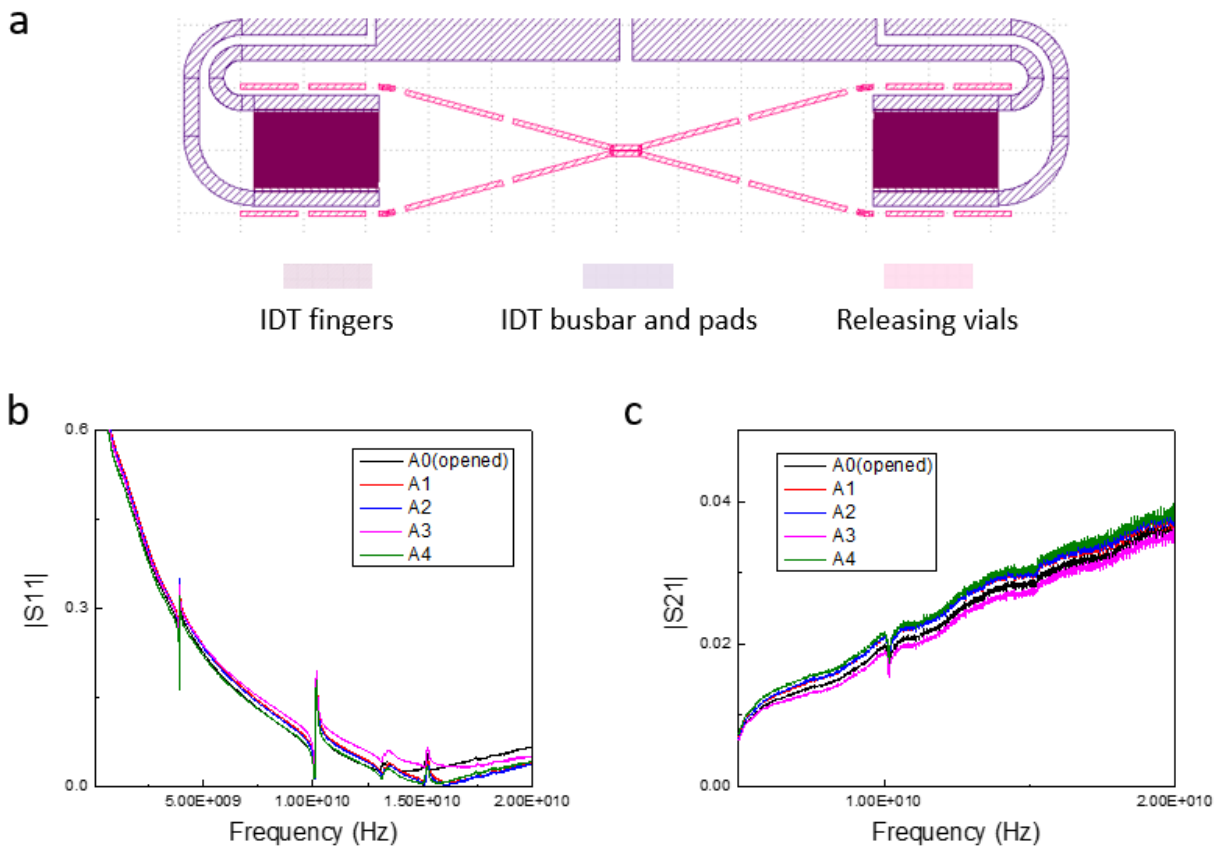

Figure 2.4 **A Lamb Waveguide Device for Acoustic Calibration**. a) Layer out of the acoustic transmission line device. Five devices with waveguide widths of 0 (opened), 0.8 μm, 1.5 μm, 2.2 μm, and 3 μm are realized. The transmitters and receivers are identical flat IDTs with 100 pairs of 1 μm period fingers and 50 μm acoustic aperture. b) S11 measurement of acoustic transmitters, acoustic resonances are identified at 3.8 GHz, 10.1 GHz, 13.1 GHz, and 15.2 GHz, respectively. c) S21 measurement of acoustic transmission. Transmission at 10.1 GHz is observed.

A typical acoustic device for transmission measurement is shown in Figure 2.4. The Lamb waves are generated from top IDT and coupled to the waveguide through a linear taper coupler. The waves are then coupled out from the waveguide and are detected by the bottom detector through the electromechanical coupling. There are 100 pairs of IDT fingers in the transmitter and the receiver with a finger period of 1 μm. The acoustic transmitter is calibrated by the S11 measurement with a vector network analyzer (VNA). Four resonances are measured at 3.8 GHz,

10.1 GHz, 13.1 GHz, and 15.2 GHz, indicating the power conversion from the electromagnetic wave to the acoustic wave. The 3.8 GHz and 10.1 GHz resonances, which match with our simulation result of Lamb S0 and A0 modes respectively, have the strongest power conversion efficiency. The 13.1 GHz and 15.2 GHz modes are high-order Lamb modes. The acoustic transmission is measured with S21 measurement. As shown in Figure 2.4(b), the weak transmission of the acoustic wave is observed at 10.1 GHz showing that Lamb S0 modes are successfully excited and transmitted to the receiver. However, the transmission power is independent of the width of the acoustic waveguide and even observed by the devices without waveguide. It means the detected signal mainly comes from leakage of acoustic waves at the supporting bars between releasing vials rather than the waveguide. This experiment shows that a normal linear taper coupler cannot convert membrane Lamb modes to the guided acoustic modes in the waveguide.

2.8 GUIDED MODES IN THE OPTOMECHANICAL WAVEGUIDE

The Lamb-like acoustic modes in phononic waveguides are more complicated. Due to the non-zero Poisson's ratio, the displacement in the *z*-direction accompanies displacement fields in the *xy* plane. To distinguish from Lamb modes defined in the membrane, I would like to call the Lamb-like modes in the phononic waveguides guided Lamb modes. The dispersion of guided Lamb mode is highly dependent on the waveguide width. Because of the relatively small piezoelectric constant of aluminum nitride and the resultant large active IDT finger area for acoustic generation, we always need to couple acoustic waves from the membrane to the waveguides. Details about how to couple acoustic waves from the membrane to the waveguide, which is different among projects, are included in Chapter 3 and Chapter 4.

Chapter 3. ELECTROMECHANICAL BRILLOUIN SCATTERING IN THE OPTOMECHANICAL WAVEGUIDE

3.1 MOTIVATIONS AND FEASIBILITY

In the well-known stimulated Brillouin scattering (SBS) process, spontaneous acoustic phonons in materials are stimulated by laser light and scatter the latter into a Stokes sideband. SBS becomes more pronounced in optical fibers and has been harnessed to amplify optical signals and even achieve lasing. The exploitation of SBS has recently surged on integrated photonics platforms as subwavelength-scale confinement of photons and phonons in waveguides leads to drastically enhanced interaction. Instead of optically stimulating the emission of photons, coherent phonons can also be electromechanically excited with very high efficiency as has been exploited in radiofrequency acoustic filters. Here, we demonstrate electromechanically excited Brillouin scattering in integrated, piezoelectric optomechanical waveguides. Acoustic phonons of 16 GHz frequency are excited with nanofabricated electromechanical transducers to scatter counter-propagating photons in the waveguide into a single anti-Stokes sideband. We show that the phase-matching conditions of Brillouin scattering can be tuned by varying both the optical wavelength and the acoustic frequency to realize tunable single-sideband modulation or filtering. By combining the fields of Brillouin scattering photonics and nanoelectromechanical systems, our approach provides an efficient interface between microwave and optical photons that will be important for microwave photonics and potentially quantum transduction.

Light-sound interaction through the Brillouin scattering process is of technological importance because this three-wave mixing process provides transduction between the fast-

moving photons and the slow-moving phonons [1-3]. Stimulated Brillouin scattering (SBS) can occur in optical fibers [4], and more recently, in integrated photonic waveguides [5-7] and optical cavities8-11, in which the optical wave and the acoustic wave can co-propagate. With a strong pump light, the acoustic mode, in fiber or waveguide, that satisfies both energy conservation and momentum conservation (i.e. phase-matching conditions) will be stimulated and scatter the light into a Stokes sideband that has a frequency lower than the pump exactly by the mechanical frequency. Because the mechanical frequency in SBS is typically in the multiple gigahertz ranges, SBS has found important applications in the optical processing of microwave signals. With the advance of integrated photonics, recently the effort in exploiting SBS has shifted from optical fibers to integrated waveguides on platforms of silicon, silicon nitride, and chalcogenide glass, leading to significant results, including Brillouin amplification and lasing, tunable microwave filters, frequency combs, and synthesizers [5-7,12-18].

Through optically stimulating acoustic waves at microwave frequencies, SBS provides a route of transduction from the optical domain to the microwave domain. The coherent excited phonons through the beating of strong pump light and seeding signals satisfy both the momentum and energy conservation automatically in stimulated Brillouin scattering. However, the low efficiency in generating phonons from the beating of the optical field requires not only a high-power laser source as the pump but also a long waveguide length for enough scattering possibility. Most of the works in on-chip SBS focus on the case signal and pump propagating in the same direction [18,25,27,30]. And the signal is set to be small compared to the pump, so the pump light is considered as an inexhaustible source of energy. But from another point of view, most power of the strong pump is wasted. Moreover, the copropagating signal is always accompanied by a stronger pump power, which may require more optical components to filter it out in some

applications. And due to the small momentum difference of two optical modes in the same direction, the acoustic wave momentum, which is just the momentum difference between two optical modes, is also very small. In this case, the shift of Stokes and anti-Stokes sidebands are always hundreds of megahertz. The modern information technology is aiming for encoding information to higher frequency channels from the gigahertz range to even tens or hundreds of gigahertz range. To match the requirement of high-frequency mechanical modulation in this range, the corresponding acoustic wavevector must be larger than the telecom light around 1550 nm, which cannot be satisfied with two copropagating modes. The other shortage of stimulated Brillouin scattering is that, to carry the microwave single, an external electro-optical modulator is required. On the other hand, acousto-optic devices have also been reinvented with modern fabrication and characterization technology since the early 2000s. However, all the works are done with low-frequency acoustic waves. Most of the work in this field focuses on acoustic excitation of local mechanical modes of an optomechanical resonator [31–33] and achieve strong coupling to the electromagnetic field, which does not really scatter photons immediately with generated phonons. The shortages and limitations of stimulated Brillouin scattering and lack of research of acousto-optic backscattering in modern on-chip platforms inspired our idea of externally excited phonons with piezoelectric effect and coupled the phonons to a waveguide to scatter back the light to its anti-Stokes sideband. In our work, both the acoustic wave and the light are confined in a one-dimensional waveguide. The acoustic wavelength needs to be half of the optical wavelength to bounce back photons, which for 1550 nm telecom light and aluminum nitride waveguide is around 500 nm. Such acoustic wave transducers are feasible with modern electron beam lithography technology. Other critical parts for efficient photon phonon scattering are acoustic modulation efficiency of refractive index and shape of the waveguide, phase matching condition of guided

acoustic and optical modes, the efficiency of phonon generating from IDTs, and the coupling efficiency of the acoustic wave from IDT regions to the waveguide.

3.2 THEORY OF ELECTROMECHANICAL BRILLOUIN SCATTERING

Firstly, I want to expand Brillouin's idea of scattering between optical and acoustic plane waves to the situation of guide modes inside the optomechanical waveguide. In our experiments, the optomechanical waveguide is a single-mode optical waveguide supporting the TE0 modes. The scattering induced by acoustic has happened between a backward TE0 mode with a lower frequency and a forward TE0 mode with higher frequency. The acoustic wave is scattered photon from one mode to another through refractive index modulation by its strain. The two optical modes are described by their electrical fields:

$$E = E^{(1)} + E^{(2)} \quad (Eq.1)$$

$$where\ E^{(i)} = e^{(i)}(r,t)a^{(i)}(z) + c.c.$$

$e^{(i)}(r,t) = \tilde{e}^{(i)}(x,y)exp\left(i\beta^{(i)}z - i\omega^{(i)}t\right)$ is the eigenfunction of the wave equation. $a^{(i)}(z)$ is the slowly varying amplitude caused by the small perturbation of $\Delta\varepsilon(x,y)\ exp(iqz - i\Omega t)$.

Similarly, the acoustic wave is characterized by the displacement field:

$$U(r,t) = u(r,t)b(z) + c.c. \quad (Eq.2)$$

$u(r,t) = \tilde{u}(x,y)exp\,(\,iqz - i\Omega t)$ is the solution of the elastic wave equation in the optomechanical waveguide:

$$\frac{\partial^2 u}{\partial t^2} = -\nabla \cdot (C:\nabla u) \quad (Eq.3)$$

$b(z)$ is the slow-varying complex amplitude of the elastic wave, which comes from both electrostrictions of the beating profile of the two optical modes and the intrinsic loss from phonon

scattering, scattering at the grain boundaries of the polycrystalline material, and the fabrication imperfections like surface roughness.

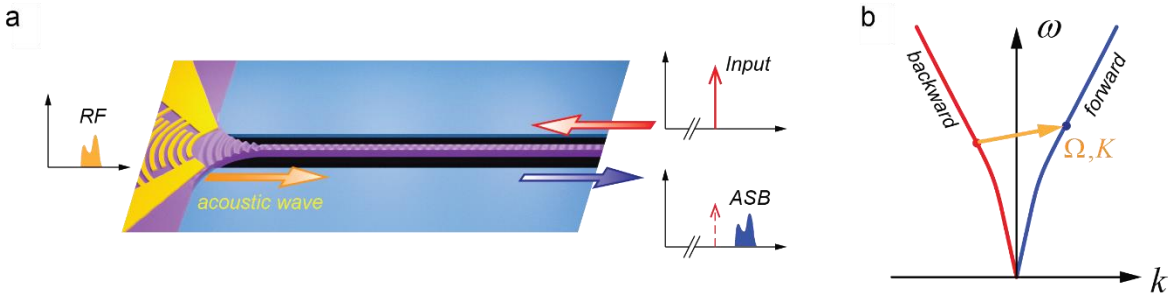

Figure 3.1 **Principle of the Electromechanical Brillouin Scattering**. a) schematic of the device core area. b) the diagram of the phase-matching condition.

For the convenience of analysis, we choose the propagation direction of the acoustic wave as positive, as shown in Figure 3.1(a), and both the electromagnetic modes and the acoustic mode are normalized to their average flux, namely, $P^{(1)} = -1$ and $P^{(2)} = P_b = 1$.

$$\begin{cases} \dfrac{\partial a^{(1)}}{\partial z} = i\omega^{(1)} Q^* a^{(2)} b^* e^{i\kappa z} & (Eq.4) \\ \dfrac{\partial a^{(2)}}{\partial z} = -i\omega^{(2)} Q a^{(1)} b e^{-i\kappa z} & (Eq.5) \\ \dfrac{\partial b}{\partial z} + \alpha b = -i\Omega Q \left[a^{(1)}\right]^* a^{(2)} & (Eq.6) \end{cases}$$

Here,

$$Q = \iint d^2 r e_i^{(1)} e_j^{(2)} n^3 P_{ijkl} S_{kl} \qquad (Eq.7)$$

is the normalized acousto-optic coupling coefficient, and $\kappa = q + \beta^{(1)} - \beta^{(2)}$ is the wave vector mismatch between the acoustic mode and the two optical modes, q is the wavevector of the acoustic wave, and $\beta^{(1)}, \beta^{(2)}$ are the wavevector of the optical waves. Here when $\kappa = 0, i.e. q =$

$\beta^{(2)} - \beta^{(1)}$, it is the so-called phase-matching condition. In the quantum mechanical point of view, the phase-matching condition, as shown in Figure 3.1(b),

$$q = \beta^{(2)} - \beta^{(1)}$$

$$\Omega = \omega^{(2)} - \omega^{(1)}$$

is equivalent to momentum and energy conservations.

We shall neglect the right side of equation $(***)$, that the acoustic wave is externally excited by the IDT and the incident light field $a^{(1)}$ is too weak that $b(z)$ is determined by the intrinsic loss of the waveguide (α) and the intensity at the waveguide entrance $\big(b(0)\big)$. Thus, we can solve the acoustic decay from $(***)$:

$$b(z) = b(0)e^{-\alpha z}$$

The acousto-optic scattering equations are then simplified to the following equation.

$$\begin{cases} \dfrac{\partial a^{(1)}}{\partial z} = i\omega^{(1)} Q^* a^{(2)} b(0) e^{(-\alpha + i\kappa)z} \\ \dfrac{\partial a^{(2)}}{\partial z} = -i\omega^{(2)} Q a^{(1)} b(0) e^{(-\alpha - i\kappa)z} \end{cases}$$

where, $b(z) = b(0)e^{-\alpha z}$ is a solution of acoustic wave decaying along the waveguide. Furthermore, only a small portion of the input (pump) light in the optomechanical waveguide is reflected onto the anti-Stoke sideband, so pump depletion is also neglected. The output anti-Stokes field and power at the end of the waveguide $(z = L)$ are then calculated, respectively, as the following.

$$a^{(2)}_{(z=L)} = i\omega^{(2)} Q a^{(1)} b(0) \left(\frac{e^{-(\alpha + i\kappa)L} - 1}{\alpha + i\kappa} \right)$$

$$P_{BS} = \left[a^{(2)}_{(z=L)} \right]^* a^{(2)}_{(z=L)} = \left(\omega^{(2)} \right)^2 Q^2 P^{(1)} P_b \left(\frac{e^{-2\alpha L} + 1 - 2e^{-\alpha L} \cos(\kappa L)}{\alpha^2 + \kappa^2} \right)$$

The signal reaches its maximum at the critical phase-matching point.

When $\alpha L \ll 1$ (short waveguide limit), the Brillouin scattering efficiency $P_{BS}/P^{(1)}$ as a function of the acoustic frequency approaches a sinc-squared function:

$$\frac{P_{BS}}{P^{(1)}} \approx \left(\omega^{(2)}\right)^2 Q^2 P^{(1)} P_b L^2 sinc^2\left(\frac{\kappa L}{2}\right)$$

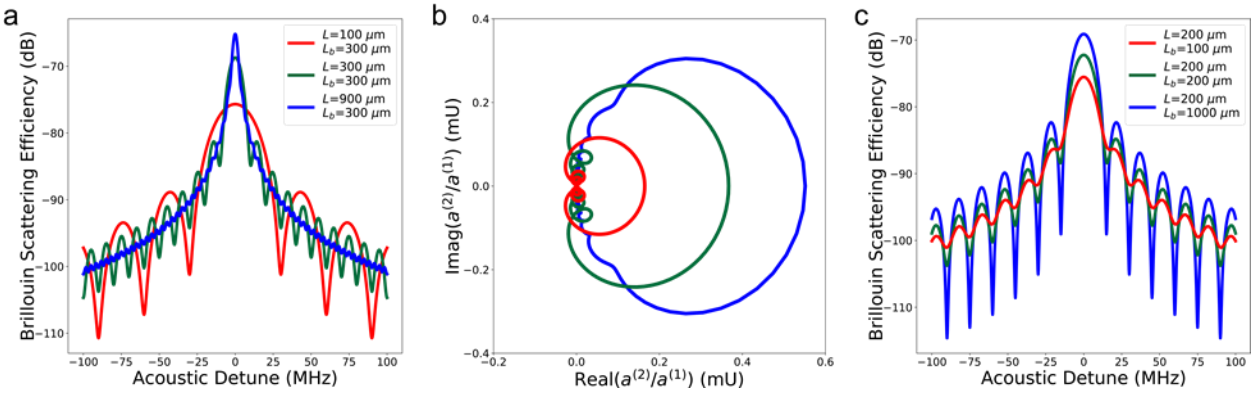

Figure 3.2 **Reflection Spectrum of the Electromechanical Brillouin Scattering**. a) power intensity v.s. acoustic detune for different waveguide lengths. b) polar chart of reflectivity for different waveguide lengths. c) power intensity v.s. acoustic detune for different acoustic decay.

The zeroes of the sinc-squared function are determined by the acoustic wave vector mismatch, such that $\kappa_{\min}^{(n)} = \frac{2n\pi}{L}$. To be consistent with our measurement data, the acoustic wave vector mismatch is expressed in terms of the frequency detune $\delta = \frac{(\Omega - \Omega_0)}{2\pi}$ from the perfect phase-matching point, such that

$$\kappa = \frac{dq}{d\Omega(\Omega - \Omega_0)} = \frac{2\pi\delta}{v_g}$$

Therefore, the positions of the periodical local minima are determined by the waveguide length and the acoustic group velocity such that $\delta_{\min}^{(n)} = \frac{nv_g}{L}$. The acoustic propagation length is defined as $L_b = \frac{1}{2\alpha}$, over which the acoustic mode decays to e^{-1} of its initial power. In our devices, the waveguides are comparable to or longer than L_b such that $\alpha L \geq 1$. In this case, the calculated

plot in Figure 3.2(c) shows that the local minima position does not change much from the zeros of the sinc-squared function, so we can still use those to extract the acoustic group velocity v_g or the effective length of the waveguide.

When the waveguide is much longer than the acoustic propagation length such that $\alpha L \gg 1$ (long waveguide limit), the Brillouin scattering efficiency approximates a Lorentzian function:

$$\frac{P_{BS}}{P^{(1)}} \approx \frac{\left(\omega^{(2)}\right)^2 Q^2 P_b v_g^2}{4\pi^2} \left(\frac{1}{\left(\frac{v_g}{4\pi L_b}\right)^2 + \delta^2} \right)$$

with the full-width-half-maximum (FWHM) linewidth of

$$\Gamma = \frac{v_g}{2\pi L_b}$$

Figure 3.2 (a) and (b) plot the representative situations of both short and long waveguide limits in logarithmic and polar plots, respectively, to show the transition.

From another point of view, the dynamical modulation of the waveguide by the acoustic wave creates a moving Bragg grating mirror. The coupling between the forward- and backward-propagating optical modes, if ignoring the optical dispersion, is equivalent to a reflection on the Bragg mirror. From the coupled-mode equations, the input optical mode exponentially decays into the mirror as

$$a_{(z)}^{(1)} = a_{(z=0)}^{(1)} e^{-\left(\omega^{(1)}\omega^{(2)} Q Q^* P_b - \frac{\kappa^2}{4}\right)^{\frac{1}{2}} z}$$

When the wavelength of the input optical mode is twice the grating period (κ=0), we can get the decay rate $\gamma = \omega |Q| \sqrt{P_b}$. The scattering factor |Q| can be estimated from COMSOL simulation to evaluate the acoustic power on demand for efficient Brillouin backscattering.

3.3 Design and Calibration of the Optical Layer

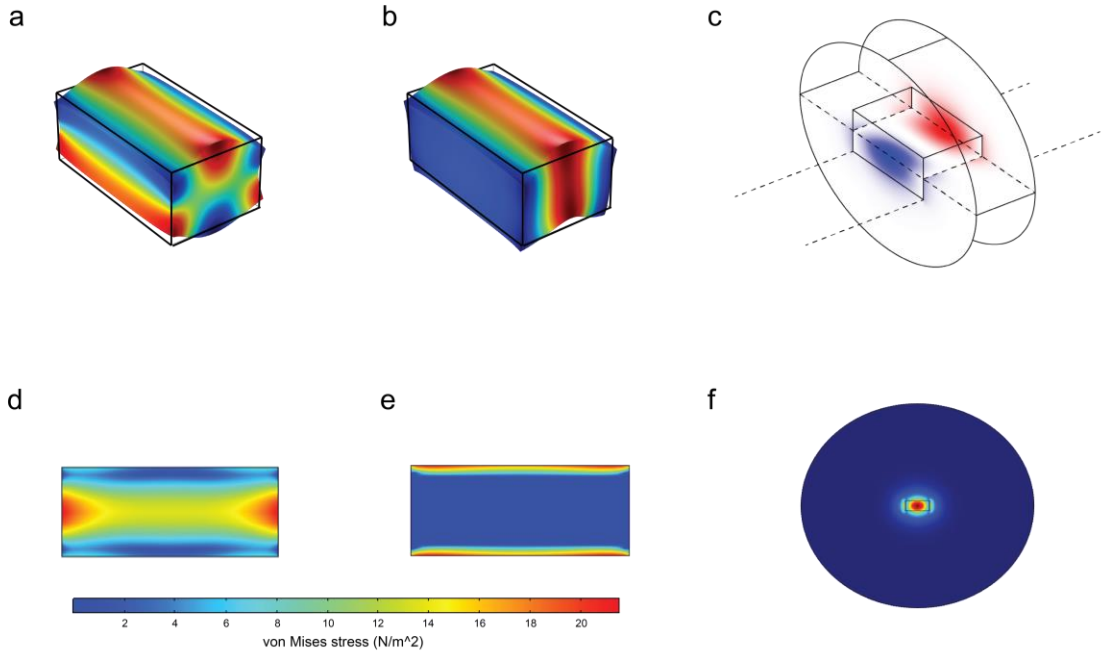

Figure 3.3 **Numerical Simulation of Guided Lamb Modes and the Optical TE Mode**. a. Mode shape of fundamental symmetrical Lamb mode (S0 mode). b. Mode shape of fundamental anti-symmetrical Lamb mode (A0 mode). c. the phase difference of optical TE0 mode in one acoustic wavelength. d. Stress distribution in S0 mode. e. Stress distribution in A0 mode. f. electrical field intensity distribution of TE0 mode in a channel waveguide.

With consideration of the feasibility of our nanofabrication, photoelasticity, and piezoelectricity, we choose aluminum nitride as the platform to realize our idea. To have better confinement of the mechanical vibration, we decided to suspend the whole structure from the substrate. We design the optomechanical waveguide as a channel waveguide with a rectangular cross-section. The simulation of acoustic modes in a suspended waveguide is shown in Figure 3. The optical modes we are interested in is the TE_0 mode, which is easy to couple with a TE grating coupler. As we can see in Figure 5, the electromagnetic field is concentrated at the center of the waveguide and symmetrically distributed with respect to the y-axis and the z-axis. The desired

reflected optical mode is also TE_0 mode, with only a small frequency shift and propagation direction flipped. To maximize the scattering coefficient, the effective refractive index perturbation term in $(Eq. 7)$ must also be symmetrical. As $E^{(1)}$ and $E^{(2)}$ reach their maximum in the center, and the acoustic modes should also have a maximum strain in the center and symmetric boundary movement. It should be noted that the modulation of the refractive index is defined by photoelasticity. From Table 1, the photoelastic coefficients in the xy plane are comparable to that in the z-direction. TE and TM modes should have similar results even though the electrical field of TE modes aligns with the smallest term in the piezoelectrical coupling matrix. For all these reasons, we choose Lamb S0 mode in which the strain and displacement field is symmetric with maximum strain in the center.

Light is coupled to the photonic integrated circuits through grating couplers. The schematic of the optical layer is shown in Figure 3.4(a). The curved grating couplers with a 40-degree opening angle are designed to couple incident TE mode to the TE mode of the waveguide. The gratings have a period of 1.1 μm and a duty cycle of 0.76. An apodized region containing 15 periods was added to gradually convert modes in the grating region to the waveguide TE mode. A 50:50 directional coupler split the input signal into two routes. One path connects to the optomechanical waveguide, where the electromechanical Brillouin scattering happens. The other path is for alignment between integrated devices with the fiber array as well as calibration of the directional coupler. The directional coupler is also used for splitting the back reflection. Half of the backscattered signal is coupled out through the output port. We designed the on-chip circuit to splitting the input signal and the back-reflected signal because the Brillouin signal can be much smaller than the reflection of the input carrier at the interface of the fiber array and the grating coupler. An on-chip splitter can filter out the reflected carrier at this interface. The photonic

integrated circuit is shallowly etched; thus, an adiabatic coupler is designed for gradually converting TE mode in the rib-waveguide to the TE mode in the channel waveguide. The shallow etched width varies to zero with an elliptical shape. The first concern of this design is that the shape reduces the reflection of the carrier. From a quick simulation, compared to the direct change from rib waveguide to channel waveguide, the reflection reduced from 2.5% to 1.4%. The other reason is that the stress distributed more uniformly along the elliptical boundary than a polynomial with sharp corners, which will be included in the Fabrication section. For a device with five μm wide optomechanical waveguide, another adiabatic taper coupler is added for conversion from TE0 mode in 0.8 μm wide waveguide to 5 μm wide waveguide.

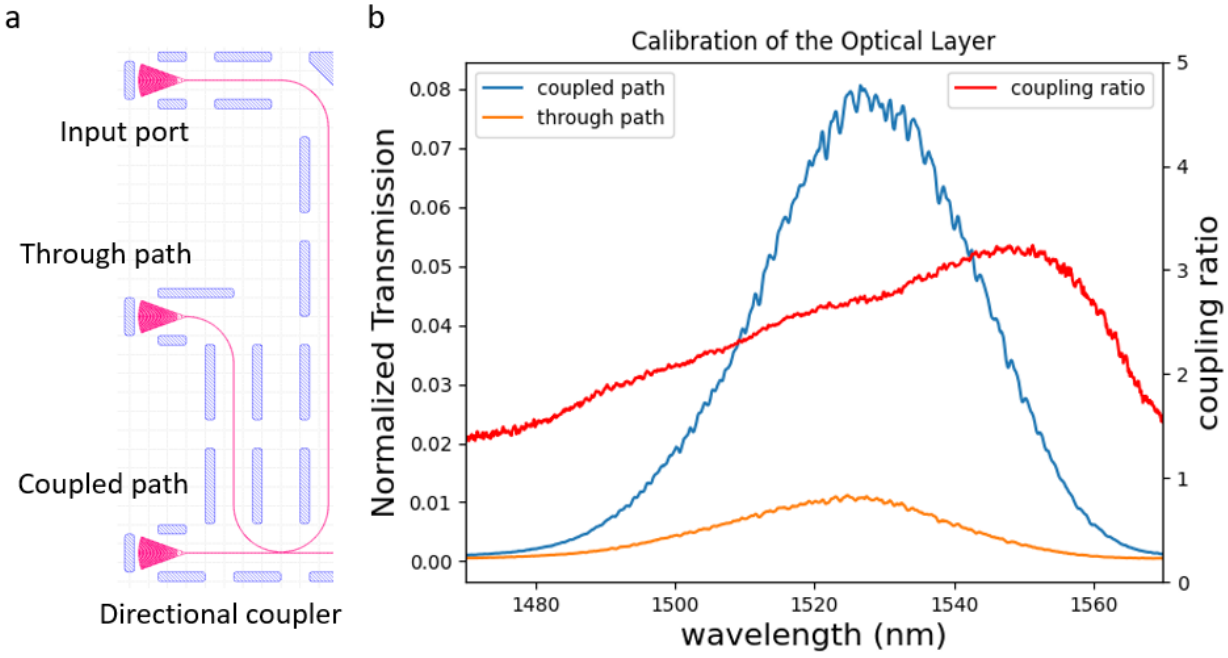

Figure 7 **Calibration of the Optical Layer**. a) schematic of the photonic integrated circuit. The laser was coupled to the input port. The through path and the coupled path transmission were measured through the other two ports, respectively. b) Measurement results of the coupling ratio and transmission spectrum

3.4 DESIGN OF THE ACOUSTIC LAYER

Because the light speed is around five orders of magnitude higher than the sound speed, in the Brillouin scattering scheme, the anti-Stoke frequency shift is much smaller than the input optical frequency. The momentum of the scattered light is identical to the input light in value but opposite in direction. Thus, the momentum conservation requires an acoustic wavelength to be half of the optical wavelength. From the FEM simulation, the effective refractive index of optical TE mode in a 0.8 μm-wide channel waveguide is slightly smaller than 1 μm. The corresponding acoustic wavelength is 0.5 μm.

The acoustic layer is challenging due to very little reference in the acoustic device wavelength of sub-500 nm. The difficulties are mainly the design and fabrication of 0.5 um IDTs. Due to the narrow width of the waveguide, directly fabricating IDTs waveguide width aperture is infeasible though it has maximum acoustic coupling efficiency. First, the 0.5 μm wavelength is comparable to the 0.8 μm waveguide width. The wave emitted from the IDTs diverges very fast that IDT fingers on the back will not contribute to the acoustic wave in the waveguide. On the contrary, the voltage drops along the busbar due to its non-zero resistance makes the IDT fingers in the front side less efficient than IDT fingers on the back. Moreover, because of the narrow width of IDT, we need to have an extremely long (> 2 mm) IDT region to match the impedance of the input microwave transmission line. If the mismatch were too large, the calibration of acoustic transmitters would be very hard that locating the resonance became a new challenge. Analog to the optical grating coupler, there are two methods to couple acoustic waves to the waveguide. The first method uses curved IDT with a curved wavefront with a focal point at the entrance of the waveguide. The second method is flat IDT with a long horn-structure mode converter. We chose the first method in our design.

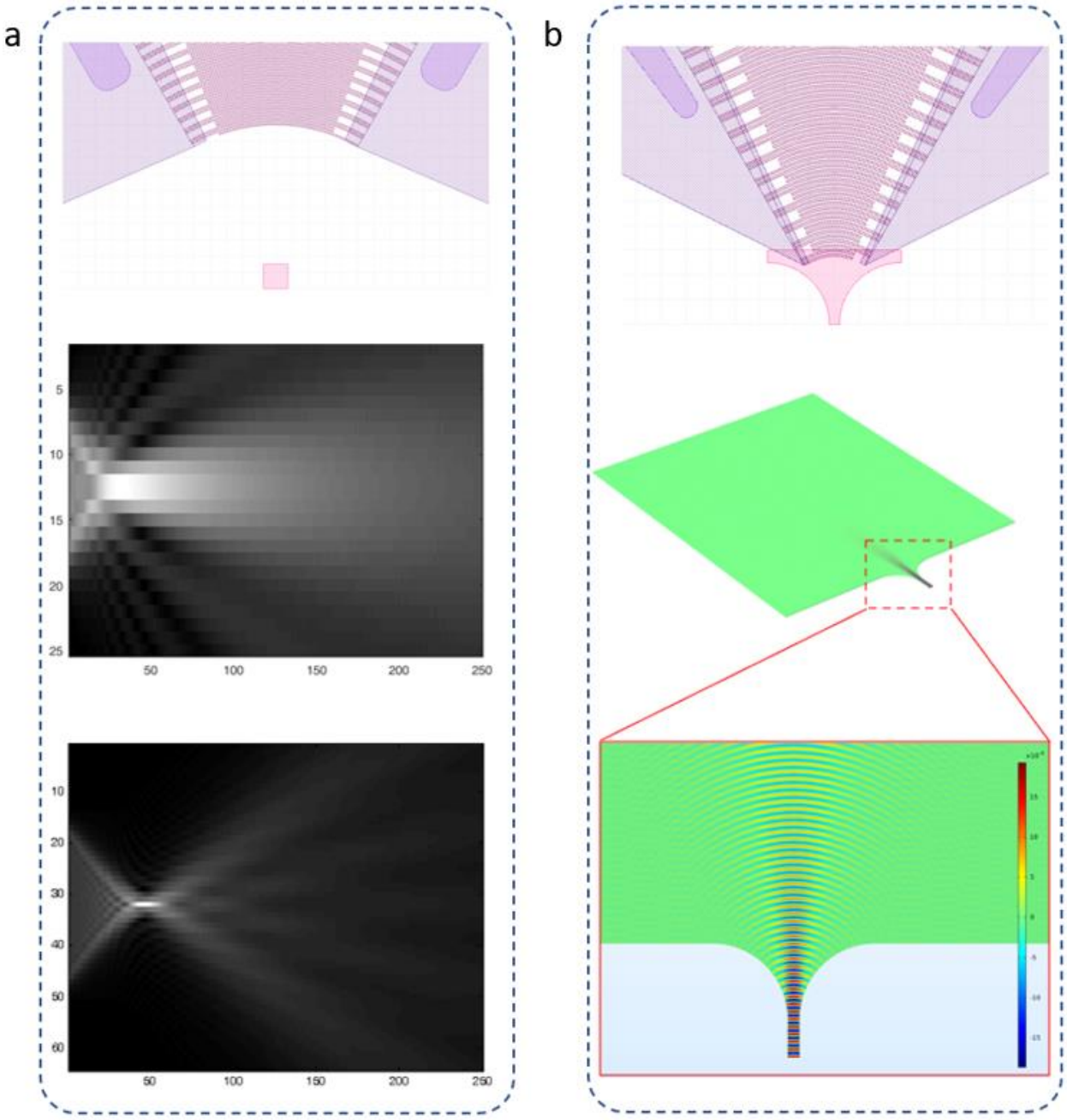

Figure 8 **The Design of focusing IDT**. a) The circular IDT fingers are used for the first batch of devices. A calculation with scalar wave approximation of acoustic wave generated from IDT with 40 (15) degree opening angle is plotted in the bottom (middle) figure. The result showed 40-degree IDT has better acoustic focusing. b) The second batch of devices used IDT wave front conformal IDT.

In our first batch of devices, we used circular IDT for the acoustic wave focusing. The angle of the IDT is estimated by applying scalar wave approximation to the Lamb S0 mode. The amplitude (A) of the acoustic wave propagates out from the IDT fingers follow the wave equation: $k^2A = \left(\partial_x^2 + \partial_y^2\right)A$. IDT fingers with opening angles of 20 to 60 degrees are simulated. The calculation result showed that the overlap between the focused acoustic wave and the entrance mode profile reach the maximum at the IDT opening angle around 40 degrees. Because waveguide width is close to the acoustic wavelength, the horizontal displacement field due to the non-zero Poisson's ratio of the waveguide makes the dispersion of guided Lamb S0 mode in the waveguide different from the Lamb S0 mode of an infinite wide membrane. For the desired 500 nm S0 mode, the mode analysis with COMSOL showed that the corresponding frequency is 16.63 GHz and 16.57 GHz for 800 nm wide waveguide and 2D membrane, respectively. Furthermore, for polycrystalline membrane, the material properties are highly related to the grain size and the qualities of grain boundaries. To compensate the difference between membranes and waveguides as well as the difference between polycrystalline membrane and crystalline bulk, the desired acoustic wavelength in the membrane is scanned from 450 nm to 490 nm for successfully exciting the desired mode.

In the second batch of devices, we further optimized IDT design based on FEM simulation. Because the focusing process of the acoustic wave is reversible, we applied the inverse design strategy that supposed the acoustic wave propagates out from the waveguide and diffract inside the membrane with a curved wavefront. I ran a FEM simulation with COMSOL for guided Lamb S0 mode propagating out from waveguide to the membrane. Then, I patterned IDT fingers along the wavefront in the membrane region to excited acoustic wave focused back to the waveguide. This strategy is used in the device with 0.8 um wide waveguide with a smooth horn structure.

However, for both the circular IDT design based on scalar wave approximation and the wave-front-conformal IDT design based on reverse propagation simulation, we ignored the additional mass loading added to the membrane by metal fingers. As shown in Chapter 2, thick gold heavily changes the mode profile therefore increase the reflection inside the IDT fingers region and dramatically change the acoustic frequency, while aluminum suffers surface oxidization. To solve the problem, we finally choose 140 nm aluminum with 25 nm gold as the electrode. To estimate the difference caused by metal electrode; a 2D FEM simulation of Lamb S0 mode was done by COMSOL. The estimated frequency shift for Lamb S0 mode at 500 nm is only about 53 MHz as shown in Figure 3.6, which is within the IDT's bandwidth.

We designed split-finger IDTs for both scalar wave approximation strategy and the wavefront conformal strategy and used the third harmonic wave excitation of the IDT. There are mainly two concerns in split-finger design. First, for normal IDT design, the IDT period is equivalent to the acoustic wavelength. The IDT finger array works as an acoustic Bragg cavity itself which stop the acoustic wave from propagating out. Even with optimal electromechanical energy conversion efficiency, most of the mechanical vibration will be confine in the IDT regions and dissipated by converting to heat or back to Joule heating in the electrical circuits. With split-finger IDT design, the period of the IDT is three forth of the acoustic wavelength, moving the acoustic frequency out of the Bragg grating bandgap. The other concern is the yield of fabrication capability. With normal IDT design, the fingers are 115 nm to 125 nm wide with height of 165 nm. The successful lift-off process required the resist thickness to be 3 times to the electrode thickness. That means the thickness of resist is about 500 nm which is much larger than the finger width. For split-finger design, the IDT finger width increase from about 120 nm to 180 nm which increases the yield a lot.

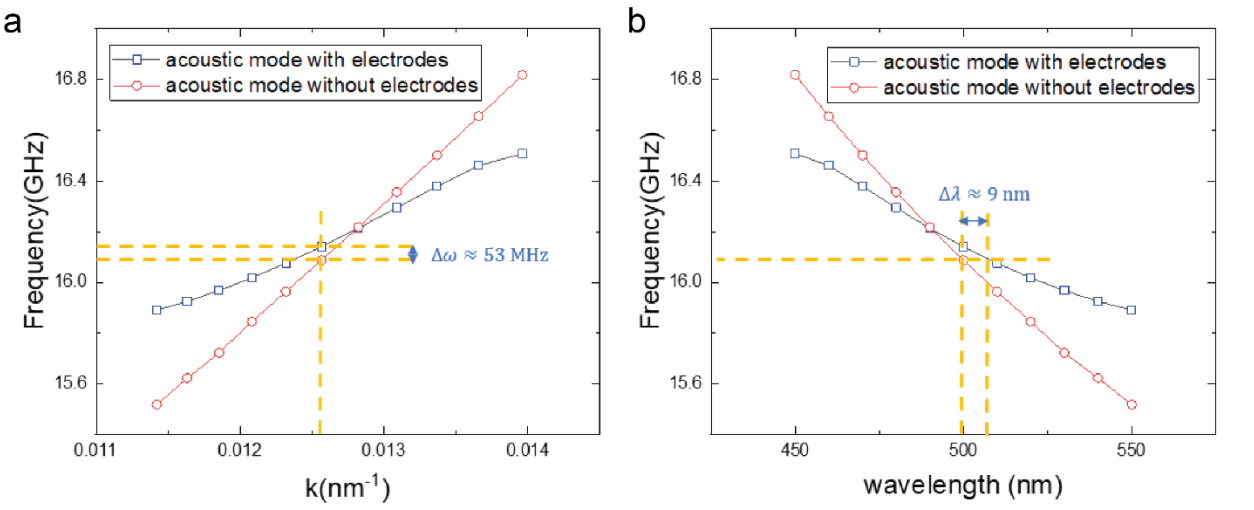

Figure 9 **Comparison of Lamb S_0 Mode Dispersion on the AlN Membranes with and without IDTs Deposited.** a. Comparison of frequency shift at a wavelength of 500 nm. b. Comparison of a wavelength different at the desired frequency for 500 nm lamb mode

3.5 Device Fabrication

The devices are fabricated on 330 nm c-axis oriented polycrystalline aluminum nitride on silicon grown by OEMGroup. To fabricate the channel waveguide, we need to use the auto-alignment technique such that the shallow etched rib waveguides and the fully etched channel waveguides are precisely aligned and independent to the EBL alignment accuracy and the resist development process. So, we used HSQ as the hard mask for the first layer. We grew 10 nm silicon nitride with PECVD (Plasmatherm 790) to protect aluminum nitride from reacting with TMAH based HSQ developer before spinning on HSQ. 180 nm HSQ was spin on as the mask. A Chlorine-based plasma etching (Oxford 180-ICP) was applied to etch away 200 nm AlN after an ebeam lithography (Vistec EBPG5000+) of photonic integrated circuits. The etching selectivity of AlN and HSQ is around 2.5:1. Then, a secondary ebeam lithography of releasing vials is applied with ZEP as the resist, and the HSQ mask is left unremoved. Another chlorine-based plasma etching was applied to fabricate the releasing vials and the channel waveguide. We removed the remaining

HSQ mask with 10 seconds HF wet etching. After typical solvent cleaning, 500 nm thick PMMA is used as the resist for fabricating IDT fingers. The split-finger IDT design increased the IDT finger width from ~125 nm to ~187 nm, which largely increased the fabrication yield. 160 nm aluminum is deposited as IDT fingers by an ebeam evaporation (CHA SEC 600) after another ebeam writing. After lift-off, the acoustic reflector is made by chlorine etching, followed by the fourth ebeam lithography with double-spin ZEP as resist. The pad region of the electrode is written by the last ebeam lithography with double-spin PMMA. The pads are made of multi-layer metals of 50 nm aluminum, 450 nm copper, 50 nm aluminum, and 50 nm gold. Finally, the device is suspended by undercut etching in XeF2 etcher. (SPTS Xacitix e2)

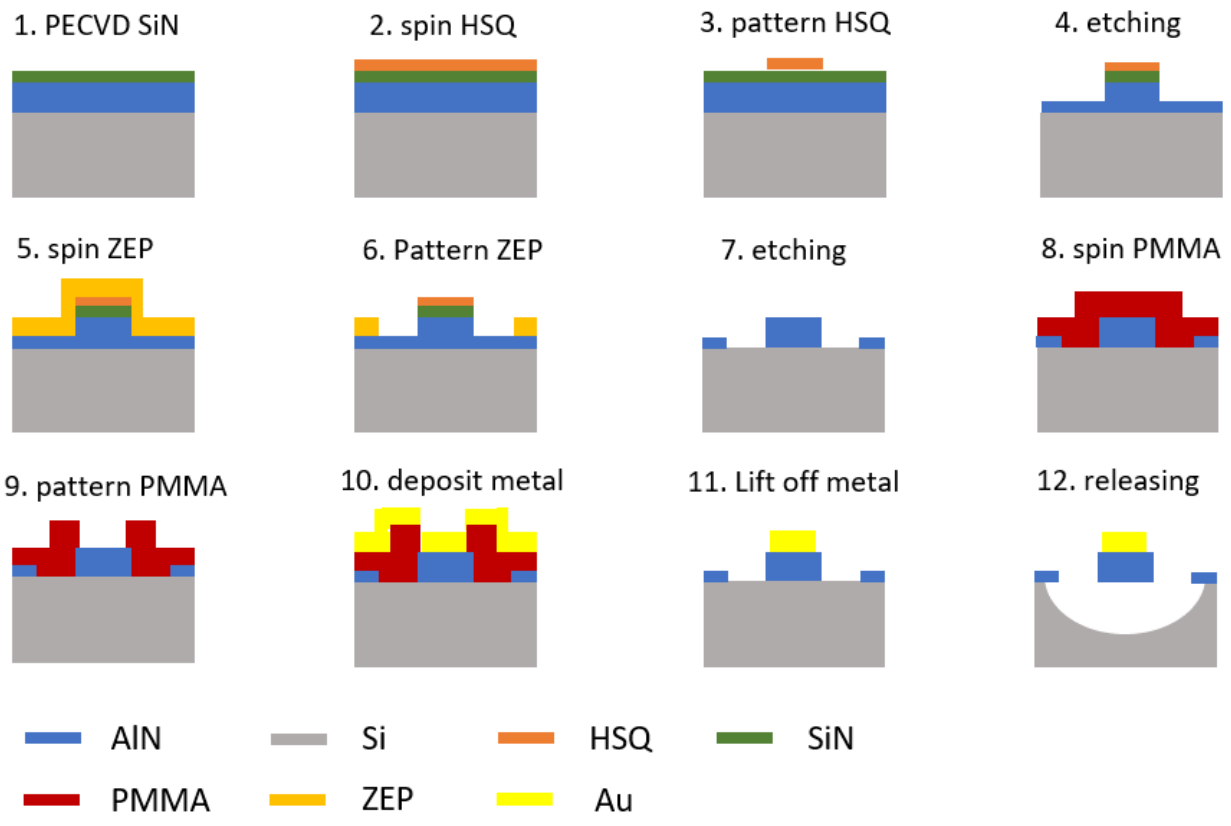

Figure 10 **Fabrication Process Flow.**

The SEM images of a sample device are in Figure 3.8. The lower-left corner is the optical input and output port, the upper right corner is the acoustic input port, and the optomechanical waveguide is located at the center. There are three ports in the optical part; light is transmitted from the rightmost one. After going through a 50:50 directional coupler, half of the light entering the optomechanical waveguide while the other half of the light is coupled out through the left-most grating coupler and used for alignment. After light is reflected by the acoustic wave inside the optomechanical waveguide, it goes through the directional coupler and splits into two paths again. Half of the reflected light is coupled out from the middle grating coupler and sent to the photodetector. Split-finger curved IDTs are deposited at the other entrance and focusing forward Lamb wave to the waveguide. Additionally, a trench reflector at the backside of focusing IDTs is precisely located half wavelength away to push the back-propagating wave back and constructively intervene with the forward propagating wave.

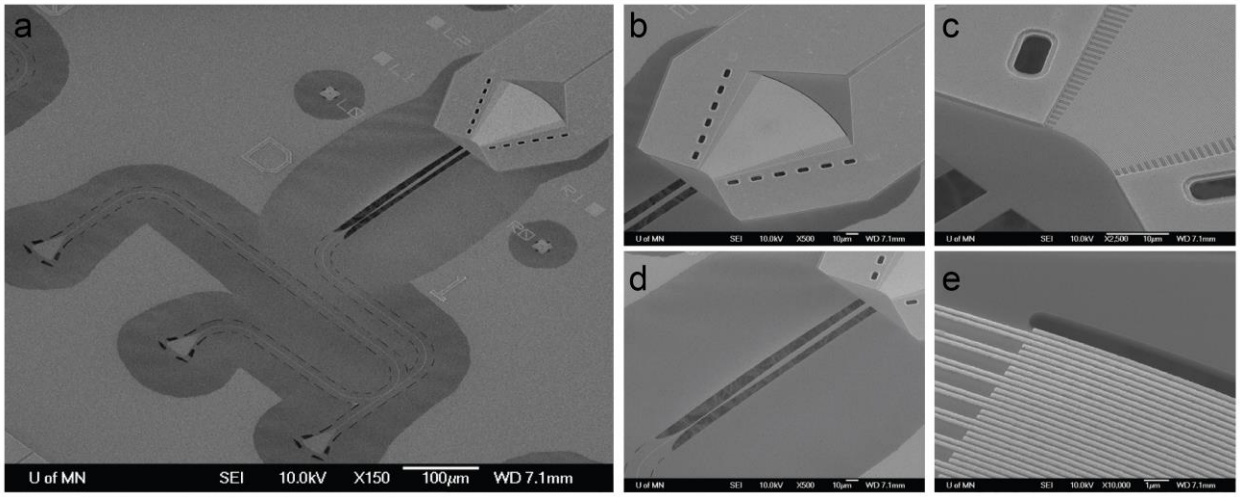

Figure 11 **SEM images of the 5 μm × 100 μm EBS device.** a. the perspective of the whole device. b. Interdigital transducers. c. Acoustic entrance. d. Optomechanical waveguide. e. Trench reflector.

3.6 DEMONSTRATION OF THE ELECTROMECHANICAL BRILLOUIN SCATTERING

The S11 measurement is firstly applied for the calibration of acoustic excitation. The spectrum shows a broadband background with several local resonances located at 1.8 GHz, 6.5 GHz, 8.1 GHz, 10.6 GHz, 12.3 GHz, and 16.4 GHz. All the pure electronic impedances are broadband, which can be fitted from the background. In contrast, the efficient mechanical excitation only occurs when microwaving frequency close to the eigenfrequency of the corresponding acoustic mode. Moreover, the frequency difference between acoustic modes is much larger than the linewidth of any modes. This allows us to separate their equivalent impedance in the equivalent circuit model. The measurement result matched our simulation. It should be noted that the equivalent circuit model we used is slightly different from the one shown in Chapter 2. The series resistor R_s comes from IDTs' the busbars and IDT fingers. The parallel resistor R_1 and capacitor C_e are circuits property of IDT fingers. Because the pitch of IDT is small, which may cause leakage and there may be some shorted channel for current flow due to fabrication imperfection during the lift-off process, the model is revised by adding a parallel resistor to the capacitor. The general complex impedance Y_a stands for an equivalent contribution from mechanical vibrations excited by currents in IDTs fingers. The fundamental S0 mode corresponding to 1.5 μm wavelength is located at 6.5 GHz. The desired third-harmonic S0 mode of 500 nm located at 16.4 GHz. The group velocity decrease in high frequency because Lamb mode properties are highly dependent on thickness and wavelength. With careful optimization, we finally come up with a design of 25%

Lamb mode generation efficiency, as shown in Figure 3.9(c), which is much higher than the acoustic generation efficiency of SBS.

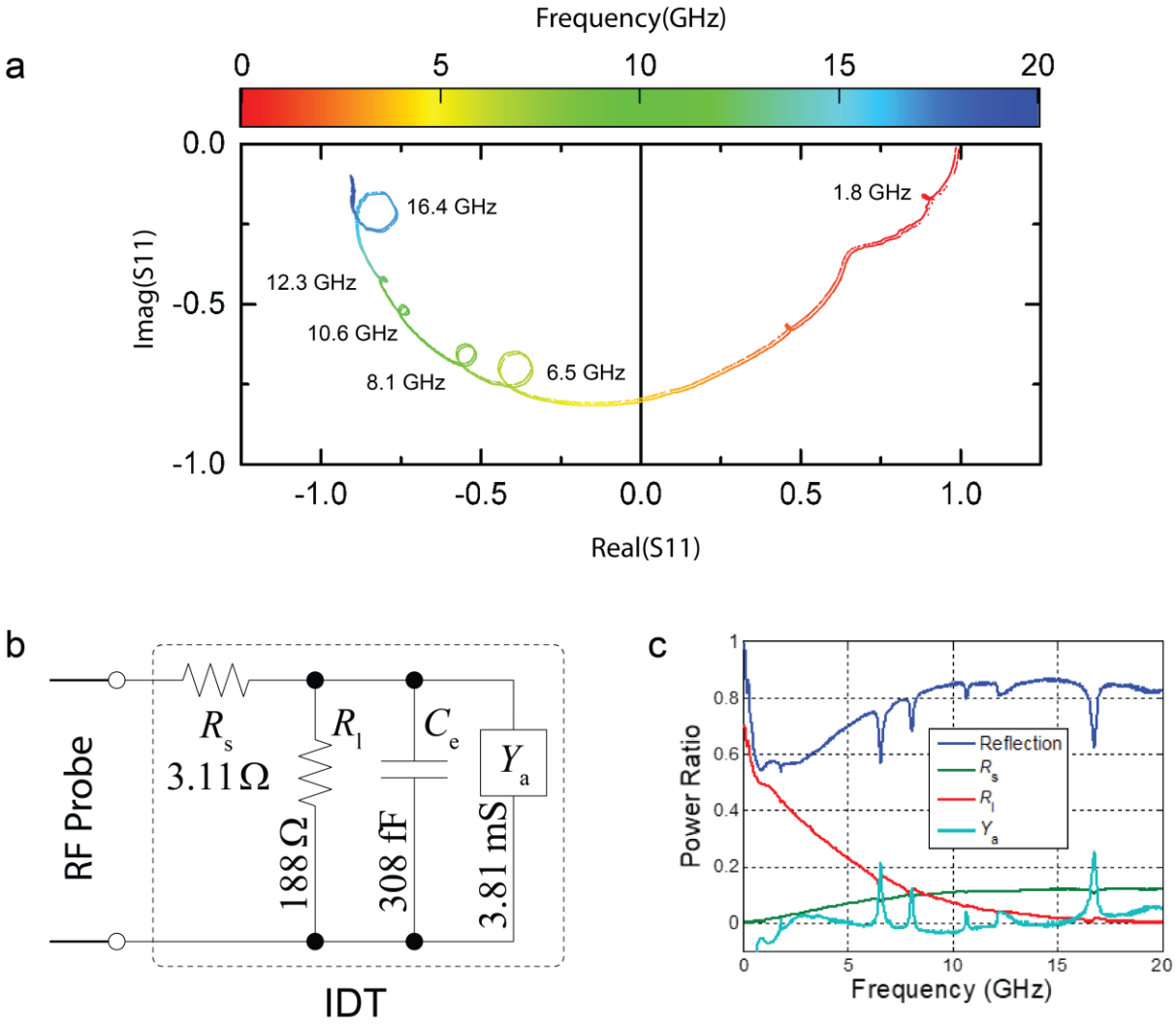

Figure 12 **Characterization of the Lamb Wave Transducer.** a) S11 measurement of the acoustic transducer, acoustic resonances at 1.8 GHz, 6.5 GHz, 8.1 GHz, 10.6 GHz, 12.3 GHz, and 16.4 GHz were labeled. b) the equivalent circuit model for the acoustic transducer. c) The power ratio of different components of the equivalent circuit model

The measurement set-up of the electromechanical Brillouin scattering is shown in Figure 3.9(a). An Agilent 81980A tunable laser is used as the light source, an Agilent E8362B vector network analyzer (VNA) is used as the RF source, and the Brillouin scattering signal is collected

by an optical spectral analyzer (OSA, YOKOGAWA AQ6370D). In the first experiment, the input optical carrier power in the waveguide, the vacuum wavelength, and the RF frequency were all fixed at -4.4 dBm, 1510 nm, and 16.4 GHz, respectively. When the RF power from the signal generator was turned on and increased from 7.9 dBm to 20.9 dBm, a sideband peak appeared on the spectra with increasing magnitude and a frequency of exactly 16.4 GHz higher than the optical carrier. This is clearly the anti-Stokes sideband (ASB) due to Brillouin scattering happening in the optomechanical waveguide when phase-matching conditions are satisfied. The center peak in the spectra, which remains unchanged with the RF power, is the reflected optical carrier due to Rayleigh scattering occurring at the IDT and due to sidewall roughness of the optomechanical waveguide. Theoretically, the ASB power should increase linearly with the acoustic power, which is proportional to the input RF power. The power of the ASB peak is extracted from the spectra and plotted versus the corresponding RF power in the inset of Figure 3.9(b). The measured results show clear linear dependence when the RF power is below 16 dBm. Above 16 dBm, however, a super-linear dependence of the ASB power on the RF power is observed. We tentatively attribute this super-linearity to the heating effect at high RF power levels, which may cause changes in properties of the material. On the red side of Rayleigh scattering, Stokes sideband is not observed that it shows the Brillouin scattering process only happens inside the optomechanical waveguide. In the membrane in front of the curved IDTs, due to multiple reflections from the boundary, Lamb wave propagates in both directions. If effective scattering happened in this region, the reflected light should contain both Stokes and anti-Stokes signals with comparable power. Furthermore, both the phase-matching condition and optical coupling are not fulfilled in the membrane, and the IDT fingers can also absorb the leaked light.

To systematically investigate the Brillouin scattering process in the optomechanical waveguide, we measured the ASB power while scanning both input optical carrier wavelength and the RF frequency with their power fixed. At each combination of the scanned wavelength and frequency, the Brillouin scattering efficiency ($\eta = P_{ASB}/P_0$, where P_{ASB} is the ASB power, and P_0 is the optical carrier power) is calculated. The results measured from three devices with optomechanical waveguide dimension of 5 μm×100 μm, 5 μm ×500 μm, and 0.8 μm ×600 μm, respectively, are presented as color-coded 2D plots in Figure 3.10 (c), (d), and (e). Cross-sectional plots at fixed optical wavelengths are also shown. In all the three cases, the efficiency reaches a maximum when the wavelength and frequency satisfy the exact phase-matching conditions ($\lambda_0 f = 2n_e v_p$), which is a curve that connects the peak points of each cross-sectional curve in the 2D plots. The 2D plots are approximately invariant along this major phase-matching line, whose slope is γ=−0.20 nm/MHz. From the plots, the acoustic phase and group velocities of the S0 mode around 16 GHz in all three devices can be extracted to be similar values of v_p =8.5×103 m/s and v_g=3.0×103 m/s, respectively.

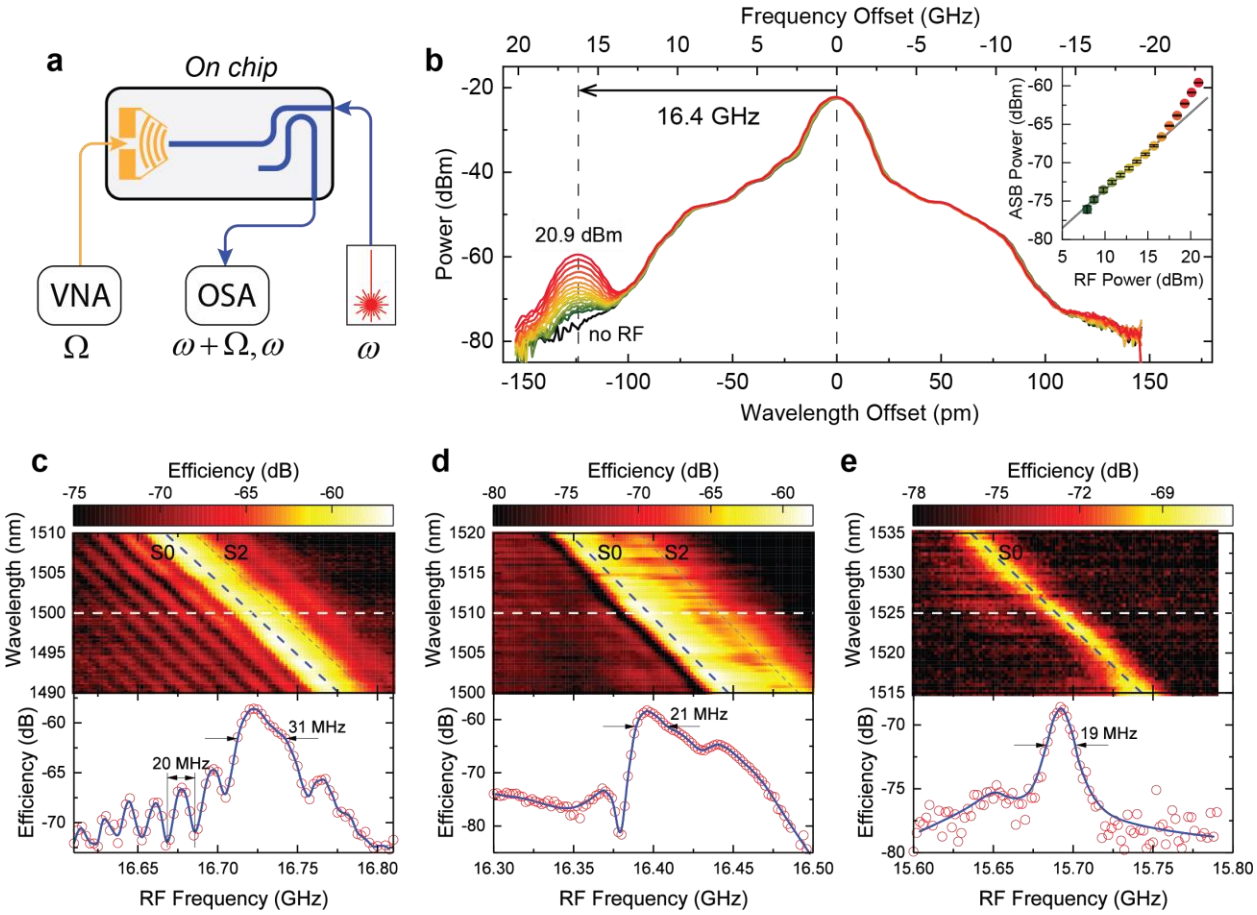

Figure 13 **Experimental Demonstration of Electromechanical Brillouin Scattering.** a. Diagram of the measurement setup. b. Spectra of the Brillouin scattered optical signal, showing a single anti-Stokes sideband (ASB) offset from the carrier by 16.4 GHz. Inset: the ASB power versus input RF power. At relatively high RF power, the dependence becomes super-linear. c-e. The 2D plot of the ASB power when both the optical wavelength and the RF frequency are scanned, measured from devices with waveguide dimension of 5 μm × 100 μm (c), 5 μm × 500 μm (d), and 0.8 μm × 600 μm (e), respectively. Lower panels show the cross-sectional plot along with the white dashed line in the upper panel. Solid blue lines are guides for the eye. The ASB power peaks along the phase-matching curve marked with the blue dashed line.

In addition to the common phase-matching line described above, the 2D plot for each waveguide dimension also shows different unique characteristics. For the 5 μm × 100 μm waveguide, the 2D plot exhibits a decaying periodic fringe pattern away from the major phase-

matching line, resembling a sinc^2(x) function. In contrast, for the 5 μm × 500 μm and 0.8 μm × 600 μm waveguides, the 2D plots exhibit a single peak pattern along the phase-matching curve, resembling the Lorentzian function. Such observations agree excellently with the coupled-mode theory of the three-wave mixing process of Brillouin scattering in optomechanical waveguides, as analyzed above.

The coupling of mode analysis gives that the pattern of the Brillouin scattering efficiency as a function of the optical carrier wavelength and the RF frequency is determined by the acoustic propagation length (L_b) and the effective waveguide length (L). In the optomechanical waveguide, the acoustic wave is excited at one end and propagates toward the other end with an exponential amplitude decay constant $\alpha = 1/(2L_b)$. Compared with the acoustic propagation loss, the optical propagation loss, which is estimated to be less than 1dB/mm from our previous two-port device, is negligibly small in the waveguide. In the short waveguide limit, where $L << L_b$, meaning that the acoustic wave does not decay dramatically within the length of the waveguide, the Brillouin scattering efficiency at a fixed wavelength or RF frequency follows a sinc-squared function of $\mathrm{sinc}^2(\kappa L/2)$ and is independent on L_b. The interval between the minima of the sinc-squared function at any fixed wavelength in the 2D plots equals v_g/L, the reciprocal of the transit time (L/v_g) of the acoustic wave through the waveguide. For the 5×100 waveguide, the short waveguide limit applies, and the 20 MHz interval between two adjacent minima in the cross-sectional curve indicates the effective waveguide length to be ~150 μm, which indicates that the acoustic wave flows into the taper region. It also indicates that the acoustic propagation length

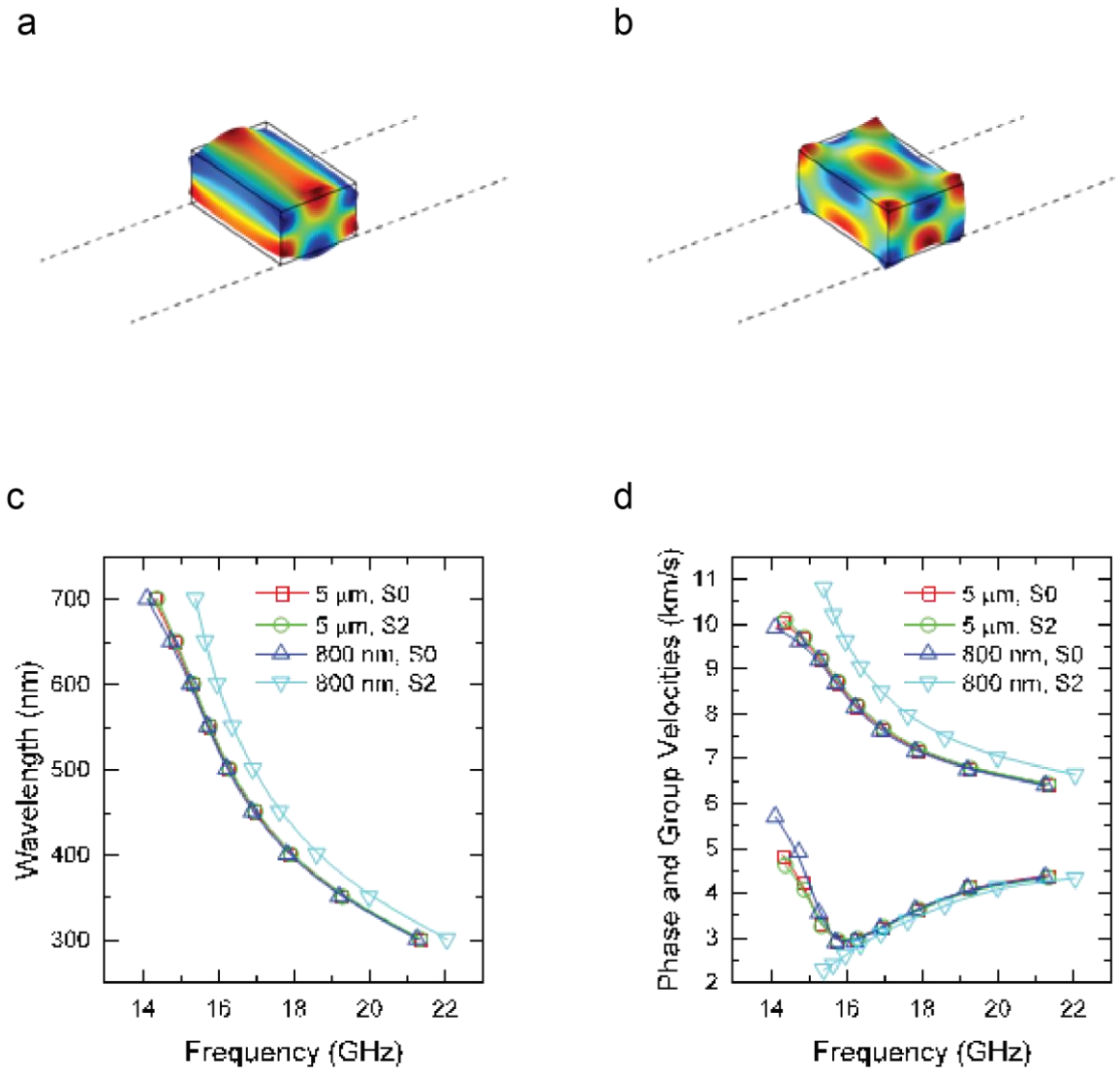

Figure 14 **Comparison of Symmetrical Lamb Modes.** a. Mode profile of S0 mode. b. Mode profile of S2 mode. c. dispersion curve of S0 and S2 modes in 5 μm and 0.8 μm waveguides, respectively. d. Phase and group velocity for S0 and S2 modes in 5 μm and 0.8 μm waveguides.

L_b has a lower bound of ~150 μm. In the long waveguide limit of $L \gg L_b$, where the acoustic wave decays to near-zero power before it reaches the other end of the waveguide, the Brillouin scattering efficiency approximates a Lorentzian function and is independent of L. As derived in the theory part, the full-width half-maximum (FWHM) linewidth of the Lorentzian at any fixed wavelength is $\Gamma = v_g/(2\pi L_b)$. For the 5 μm × 500 μm and 0.8 μm × 600 μm waveguides, the long

waveguide limit applies. The 20 MHz linewidths in Figure 3.9 (c) and (d), taking vg= 3.0×10^3 m/s, indicates a surprisingly low L_b value of 25 μm, much less than that measured in the short device. We attribute the drastic difference in acoustic loss between the short and long optomechanical waveguides to the variation of AlN film quality in different batches and the etching processes.

Furthermore, in the 5 μm ×100 μm and 5 μm ×500 μm waveguides, other than the dominant S0 mode, another acoustic mode is also observed on the high-frequency side of the phase-matching curves. Although this secondary acoustic mode does not significantly contribute to the Brillouin scattering efficiency, its presence distorts the patterns of the 2D plots, rendering them asymmetric with respect to the phase-matching curves. Such asymmetry is not observed in the 0.8×600 waveguide, indicating that only a single mechanical mode, the S0 mode. Another batch of simulations of acoustic modes of 0.8 μm and 5 μm waveguide is run to verify this highly degenerated mode. As shown in Figure 3.10 (b), the Lamb S2 mode, which has displacement fields of opposite direction between the center and two sidewalls, can also be excited from IDTs. For the 0.8 μm waveguide, the S2 mode at 500 nm is about 500 MHz higher than S0 mode in acoustic frequency. This is much larger than our acoustic frequency scanning region, as well as the IDT bandwidth. Moreover, the FWHM of the Lorentzian peak is the only 20MHz, which is far less than 800 MHz. In contrast, frequencies of the S2 mode and S0 mode are only tens of megahertz different, which explains the existence of two peaks.

3.7 APPLICATIONS IN THE RF-PHOTONIC LINKS

The Brillouin scattering in the optomechanical waveguides naturally provides single-sideband (SSB) modulation that is needed for RF photonics communications but otherwise can only be

realized with a sophisticated modulator. To this end, we employed both the homodyne and heterodyne interferometry schemes to demonstrate. On the transmitter side, the measurement scheme is the same as that in Figure 3.9 (a), except that the OSA is now replaced by a meters-long fiber link, which transmits both the Brillouin-scattered ASB and the Rayleigh-scattered optical carrier to the receiver side. The entire optomechanical waveguide device now serves as an SSB modulator with a tunable transmission band for the communication link. For the homodyne scheme, on the receiver side, the Rayleigh-scattered optical carrier, being almost constant throughout the measurement, conveniently serves as the local oscillator (LO). Both the ASB and the carrier transmitted through the fiber link are amplified with an erbium-doped fiber amplifier (EDFA) and routed to a high-speed photodetector (PD). The beating of the ASB and the carrier at the PD down-converts the signal to RF frequency Ω. The complex amplitude of the beating RF signal is measured with the VNA. Figure 3.12 (b) shows the normalized power from the 0.8×600 waveguide measured with four different carrier wavelengths. Expectedly, the efficiency peak moves as the carrier wavelength changes, consistent with the phase-matching line with a slope of −0.20 nm/MHz as in Figure 3.9 (c-e). The efficiency peak for 1530 nm is consistent with the cross-sectional curve at the same wavelength in Figure 3.9 (e). Also included in Figure 3.12 (b) is the normalized complex amplitude of the ASB for 1530 nm in a polar chart, showing both the magnitude and the phase. The shaded blue lines in both panels of Figure 3.12 (b) show the curve fitting results based on the coupled-mode theory, which approximates a Lorentzian peak and agree excellently with the measurement results.

For heterodyne interferometry, on the receiver side, the LO is tapped and frequency-shifted by $\Delta\omega$ from the laser source on the transmitter side. The frequency shift is achieved by an acousto-optic frequency shifter (AOFS) operating at around $\Delta\omega/(2\pi) = 100$ MHz. The ASB transmitted

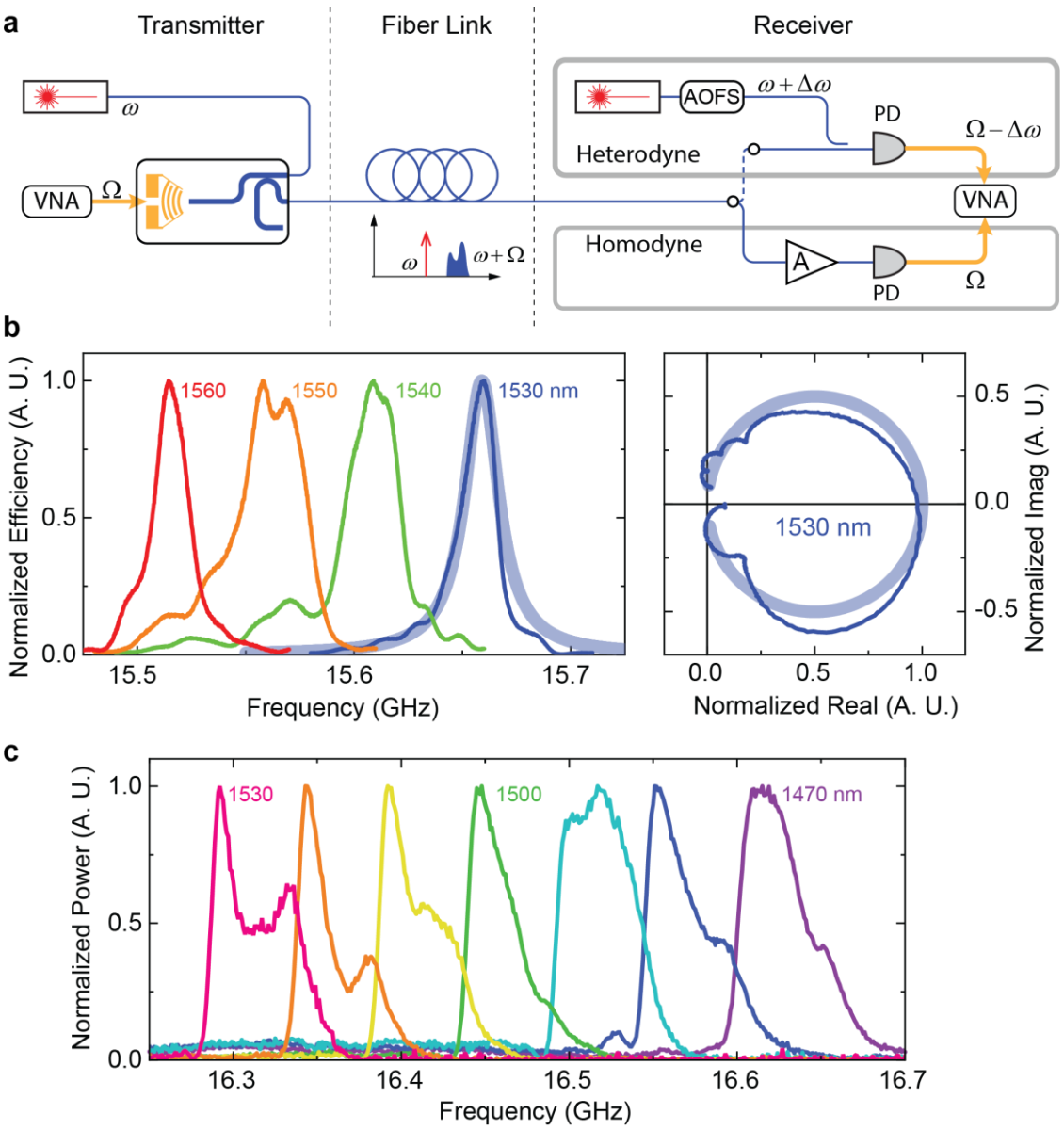

Figure 15 **RF Photonic Link Using Electromechanical Brillouin Scattering**. a. Schematics for transmitting RF signals using homodyne and heterodyne demodulation schemes. b. Measurement results when the homodyne scheme is used. Left panel: The transmission band is tunable over a range of ~200 MHz along the phase-matching curve (Fig. 3.10 (d)) when the optical carrier wavelength is tuned. Right panel: The phase of the transmitted signal is preserved as the received signal shows a full phase tuning between $\pm\pi/2$ within the transmission band. c. Measurement results when the heterodyne scheme is used. The heterodyne scheme is immune to phase scrambling during the transmission. The transmission band is also tunable over a range of >300 MHz by changing the optical carrier wavelength.

through the fiber link is combined with the LO through a 1:1 fiber directional coupler and routed to a high- speed photodetector (PD), which generates the beating signal at the RF frequency $\Omega-\Delta\omega$. It is solely for the convenience to derive the receiver LO from the transmitter laser source. In real-world applications, the LO will be another independent laser at the receiver site, whose frequency is most likely different from that of the transmitter laser. Because the ASB and the LO propagate through different fibers, their relative phase is completely scrambled due to the random refractive index fluctuations in the fibers. In real-world applications, this will also be the case because the long-haul fiber link will be susceptible to disturbance, and the LO will be from an independent laser source. In contrast, the homodyne interferometry does not suffer from this problem because the ASB and the carrier (LO) always propagate through the same optical path. With the scrambled phase, only the power of the beating signal at frequency $\Omega-\Delta\omega$ is measured by the VNA. Figure 3.12(c) shows the measurement results from the 5×500 waveguide for seven different carrier wavelengths, consistent with those in Figure 3.12(d). The horizontal axis is the frequency $\Omega/2\pi$, at which the IDT is driven. In both the homodyne and heterodyne schemes, the transmission band, which is about 20 MHz to 40 MHz wide, can be tuned continuously across a frequency span of ~200 MHz and >300 MHz, respectively, by changing the input optical carrier wavelength.

3.8 CONCLUSION OF THE PROJECT

My work has successfully demonstrated the phenomenon of electromechanically induced Brillouin scattering. In my opinion, the significance of this work is to confine light and acoustics in the same wavelength range in the same waveguide. Distinguished from other works, the interaction between photons and phonons occurred in optomechanical cavities; even though some also demonstrate optomechanical waveguides, we proved that the optomechanical waveguides could co-guide photons and phonons and with strong interaction. However, the highest Brillouin

scattering efficiency achieved for the 5 μm×100 μm, 5 μm ×500 μm, and 0.8 μm ×600 μm waveguides are −56 dB, −58 dB, and −67 dB, respectively. A FEM simulation is applied to estimate the Brillouin scattering efficiency. The Lamb wave is considered as a Bragg grating with refractive index perturbation $\Delta n = \Delta n(x, y) \cos kz$ proportional to the acoustic power inside the waveguide. The simulation result showed that for 1 mW acoustic power inside the waveguide,

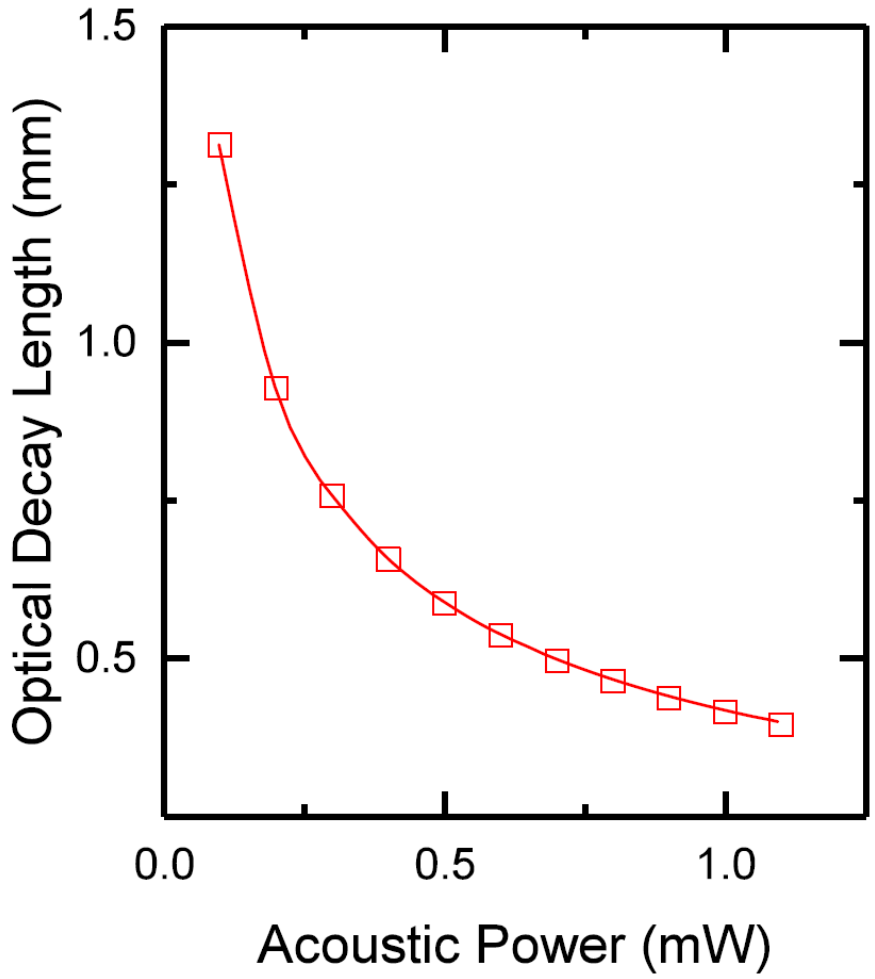

Figure 16 **Optical Decay Length with Acoustic Power in the Optomechanical Waveguide.** A FEM simulation of optical decay due to Brillouin backscattering is applied using COMSOL. Refractive index modulation by photo-elastic effect, Pockels effect from the piezoelectric field, and boundary movement is considered

the optical decay length is 0.415 mm, meaning Brillouin reflection efficiency achieving 98% for 500 μm long waveguides. However, the measurement results are drastically lower than 98%. The S11 measurement and the optical transmission measurements show effective acoustic generation and optical coupling. So, we attribute this drastically low efficiency of the device to the coupling of the Lamb wave from the membrane to the optomechanical waveguide. As discussed above, the shape of IDTs, as well as the coupling region, is not well optimized. The Lamb wave mode has particle displacement in both longitudinal and transverse direction, so the scalar wave approximation is not accurate, especially for waveguide width of 0.8 μm, which is in the same order of acoustic wavelength 0.5 μm. Another uncertainty comes from the etching process of aluminum nitride. The plasma etching of aluminum nitride is not stabilized due to a mixture of usage of O_2 plasma, fluorine-based plasma, and chlorine-based plasma in the same tool. The flashing plasma during etching will cause the unsmooth sidewall of the optomechanical waveguide, thus increase the acoustic loss. The gas-phase XeF_2 etcher will also leave some polymer-like thin film on the suspended membrane, which is hard to be removed. The HSQ that must be developed in TMAH based solution requires an additional silicon nitride protection layer and makes the chemical environment even more complex. And the BOE wet process for removing the remaining HSQ and silicon nitride protective layer may also attack the surface of the aluminum nitride. Both unstable etchings and indelible byproducts can increase acoustic loss as well as affect acoustic frequency.

Our plan is to solve all the technical problems first. For the Lamb wave coupling, instead of using curved IDT, we are going to try simple flat IDTs but add a parabolic horn coupler between the membrane and waveguide. The design of the parabolic horn comes from an analogy in ray optics. Furthermore, mechanical modes are denser in membranes, so the plane width needs to

change slowly to avoid coupling to unwanted modes at similar frequencies. When it is getting narrower, mechanical modes density is much lower, so a faster change will not end in too much power loss. In principle, if the acoustic wave is lossless, longer the horn results in higher acoustic coupling. However, the propagating loss inside the horn region is non-negligible. The trade-off between length and width of the horn needs further experimental characterization. Some previous works, as shown in Figure 3.14 presented about 9:1 wavefront width compression ratio in a 2 mm-long horn for a surface acoustic wave on GaAs [145]. This is the start point of our horn design. The other problem that limits our device performance is an acoustic loss. To solve the unsmooth sidewall from unstable plasma etching, we are going to optimize our etching recipe in the new etcher. To solve the BOE and XeF2 etching problem, we are now using sputtered aluminum nitride on silicon dioxide and use HF vapor etcher for removing silicon dioxide hard masks and releasing the devices. With the difficulties of acoustic coupling and loss solved, we can make a more functional device. Firstly, for our current device, with a strong anti-Stokes sideband generated, a useful on-chip acousto-optical modulator or an RF link is built spontaneously. And another interesting result we are eager to see is the acousto-optical induced nonreciprocity. If the acousto-optic interaction can be further improved, most of the photons are scattered back to its anti-Stokes sideband; thus, there will be no transmission when sending like from this end. However, if the light is sending from the other end of the waveguide, light is co-propagating with the acoustic wave and does not satisfy the phase-matching condition, and the transmission is not forbidden; therefore, break the reciprocity of the optical system.

In conclusion, we have successfully demonstrated on-chip backward Brillouin scattering in an optomechanical waveguide with electromechanically generated phonons. The phase-matching conditions of this nonlinear three-wave mixing process is reached with an ultrahigh acoustic

frequency of 16 GHz. The gigahertz range acoustic wave has a unique position to bridge the telecom infrared light and wireless microwave communication system. And we also demonstrated this potential application of photonic links. We are still working on optimizing the fabrication technology and design of our device to push the Brillouin scattering efficiency close to unity, so this Brillouin optomechanical system can be competitive and find more applications in microwave photonics.

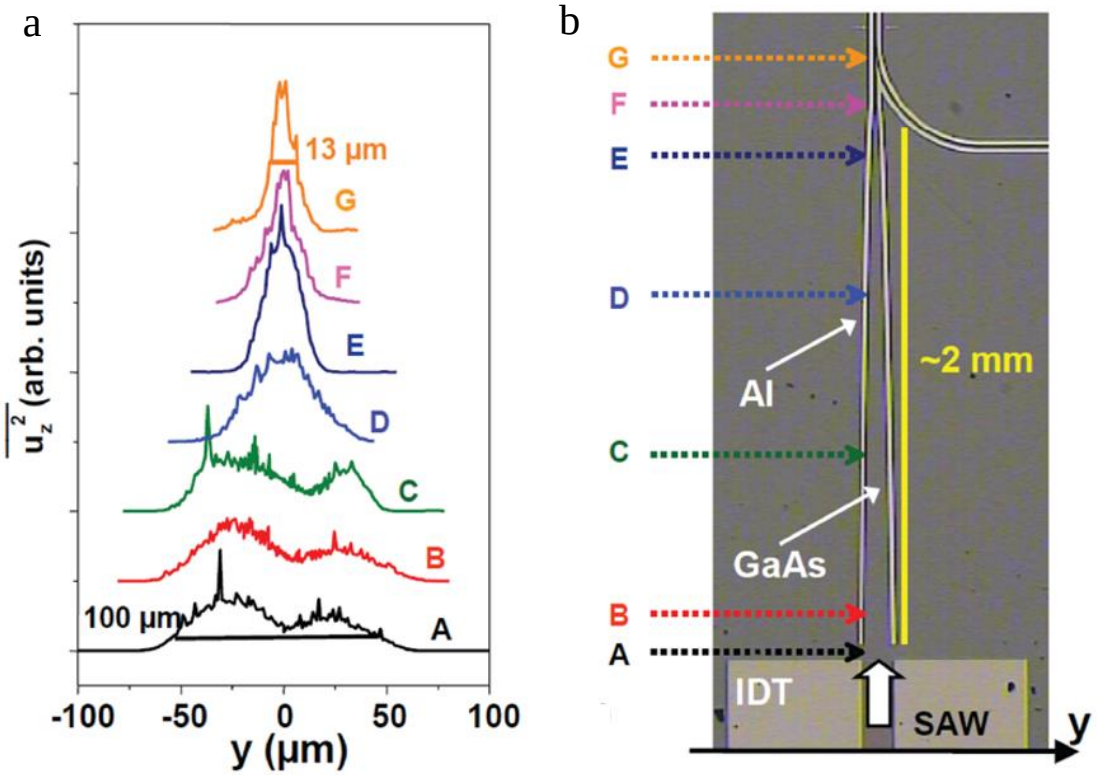

Figure 3.14 **Parabolic Horn for Surface Acoustic Wave Coupling from IDT to the Waveguide** [145]**.** a) acoustic mode profile at different position in the acoustic coupler shown in b. b) Optical image of the SAW waveguide.

Chapter 4. SUBWAVELENGTH-SCALE PHONONIC WAVEGUIDE FOR GHZ-RANGE LAMB MODES

4.1 INTRODUCTION

One of the main differences distinguishing Brillouin optomechanics from the traditional cavity optomechanics is the propagational modes of mechanical vibrations. The directionality of the acoustic modes breaks the time-reversal symmetry of the photonic system resulting in novel phenomena like the electromechanical Brillouin scattering and applications like single-sideband acousto-optic modulation. However, currently due to the inefficient acoustic mode generation in the subwavelength-scale waveguide, the Brillouin scattering signal is too weak to realize real applications. The study of the coupling mechanism of acoustic waves to subwavelength structures is emerging for future work in integrated acousto-optics. Moreover, besides working as a medium for cross-talking between light and microwave signals, acoustic waves are information carriers themselves. In the classical regime, surface acoustic waves transfer microwave signals in the piezoelectrical resonance thus have been used as microwave bandpass filters in the mobile and wireless communication. In the quantum regime, the piezoelectrically excited phonons are demonstrated as low-loss channels for routing and delays between superconducting qubits.

Traditional surface acoustic wave devices focus only on the design of transmitters, receivers, as well as cavities. Acoustic waves in guided structures especially of the subwavelength dimension have not been fully investigated. Inspired by previous works in the photonic integrated circuits, phononic integrated circuits guiding acoustic waves on nanoscale on-chip acoustic waveguides became popular recently. The current work of phononic integrated circuits on GaN/Sapphire[105]

and $LiNbO_3$/Sapphire[146] rely on the index-guiding principle of confining acoustic modes by cladding the low sound velocity material with materials of higher sound velocity. Another more straightforward way, which has not been demonstrated yet, is to guide acoustic waves is isolating the waveguides from surroundings by releasing the whole structure. In this work, I am going to demonstrate a phononic waveguide based on a suspended aluminum nitride beam in the subwavelength regime. I am also going to study the coupling mechanism of acoustic wave from membrane to subwavelength-scale waveguides.

4.2 MOTIVATION

Aluminum nitride is famous for its good mechanical and optical properties. Its strong piezoelectricity made it easy to generate acoustic waves through AC electrical signal. Different from index-guiding surface acoustic wave waveguides made on LiSa or GaN-on-sapphire platform, aluminum nitride's high acoustic velocity made it impossible to guide surface acoustic waves on substrates like sapphire or silicon dioxides. However, owing to the CMOS compatibility, the fabrication of suspended waveguides on aluminum nitride is not a big problem. Compared with the index-guiding phononic circuit, in which displacement fields are extended evanescently to the substrate, the suspended waveguides strictly isolate acoustic energy from leaking substrate, thus, in principle, have better confinement and lower loss of the acoustic modes. The better confinement is important for design high performance integrated phononic devices like microwave delay lines and ring resonators. Like free-space optics, surface acoustic waves suffer from diffraction during the propagation in free-standing membranes, which limited the propagation distance of the surface acoustic wave devices. Confining acoustic waves to subwavelength-scale waveguides is one way to solve this problem. More importantly, the properties of acoustic modes are not only dependent on the elastic moduli of the bulk material but also highly related to the boundary condition. When

waveguide width is comparable to the acoustic wavelength, the properties of guided modes change dramatically. The guided modes confined in wavelength scale or subwavelength scale suspended phononic waveguides have not been investigated.

Moreover, the research of acoustic waveguides in the subwavelength scale is important for the future optomechanical waveguide-based acousto-optic devices. In Chapter 3, we concluded that the low Brillouin scattering efficiency mainly due to the high acoustic loss of the guided modes and weak coupling of the acoustic wave from the free membrane to the optomechanical waveguide. The key to these problems is understanding the coupling mechanism of an acoustic coupler and what the mode looks like inside a suspended waveguide. With the microwave impedance microscopy provided by our collaborator from UT Austin, we successfully visualize the coupling process in the coupling region, which help us understand the acoustic coupling mechanism in a parabolic horn structure and guide our future design of acoustic waves. The visualization of the acoustic wave also proved the functionality of the microwave impedance technology for inspecting arbitrary mechanical vibration pattern on piezoelectrical material.

4.3 DEVICE DESIGN

In order to realize the Lamb wave phononic waveguides and study the acoustic coupling process, two-port phononic devices are designed. Due to the relatively small piezoelectricity of aluminum nitride, directly fabricating IDT at wavelength width is far from impedance matching of the measurement transmission line; all devices have apertures at least one order of magnitude wider than the waveguide length. Because we need to couple acoustic waves into the suspended waveguide, there are two parabolic acoustic horns added at each end of the waveguide as the acoustic coupler. The Lamb waves are generated piezoelectrically through the acoustic transmitters made by interdigital transducers and coupled to the suspended phononic waveguide

through the parabolic acoustic horn. The wave propagates through the waveguide and then inversely converts to the membrane mode through another horn and received by the receiver. The most challenging part is the large difference between the phononic waveguide width and the IDT aperture. On the one hand, broader IDT excited waves with better collimation and stronger power. On the other hand, the coupling from Lamb waves to sub-wavelength waveguides is less efficient and requires longer acoustic horns. Both the loss and the inter-mode coupling can dramatically decrease the energy of the desired mode and lower the coupling efficiency. In order to optimize our design, three groups of devices were designed with IDT aperture of 10 μm, 20 μm, and 30 μm with acoustic coupler length of 25 μm, 100 μm, and 200 μm, respectively. The acoustic group velocity and decay length were calibrated by varying the waveguide length from 100 μm to 400 μm. The period of the IDT is 3 μm. We apply the split-finger design to reduce the loss caused by the instructive interferential reflection of the generated acoustic wave inside the IDT region. The width of the waveguide is 1 um, which is only one-third of the acoustic wavelength. Two releasing vials were opened at the two sides of the interdigital transducers to suspend the transmitter, and the receiver to avoid reflection at the interface between the unsuspended region and the suspended region and also reduce the mode mismatching. Besides three major groups of devices, we also added two groups of devices to calibrate the design of interdigital transducers. The Group S contained devices with 10 um wide IDT aperture with the number of finger pairs varying from 5 to 40. This group is used for calibration of components in the equivalent circuit model. Group H contained devices with much narrower IDT. The IDT apertures width in Group H were 3 μm, 3.5 μm, and 4.8 μm, respectively. The acoustic horn length of Group H is set to 25 μm. The last special group is Group SP. This group contains acoustic devices with a period of 0.5 μm IDTs for calibration of the fabrication process of ultra-high frequency Brillouin optomechanical devices.

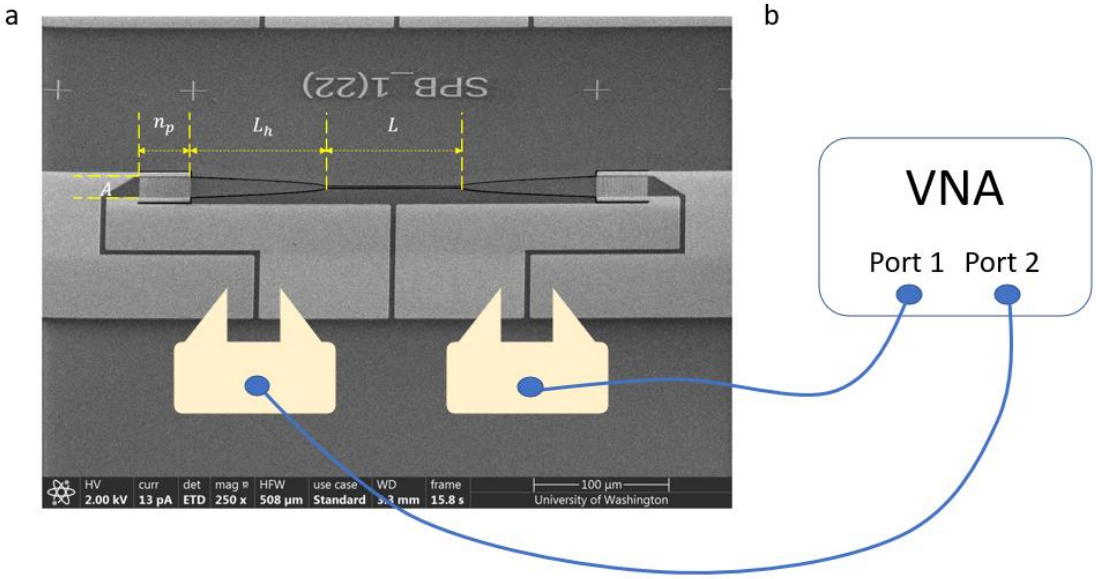

Figure 4.1 **The Device Image and the Schematic of the Measurement Set-up.** a) the SEM image of one sample device. The definitions of key parameters are presented in the image. b) the measurement set-up of the phononic waveguide device.

4.4 Device Fabrication

The devices were fabricated on a commercial 330 nm c-axis polycrystalline aluminum nitride grown by magnetron sputtering on 3 µm thick thermal oxides on silicon wafer from OEM Group. 240-nm-thick silicon dioxide was grown on top of the aluminum nitride as a hard mask by PECVD. The boundaries of the waveguide and the horn-shaped converters and the releasing vials of transducers were patterned with an electron beam lithography using a JEOL 6300F system and ZEP520A as the resist. The pattern was transferred to the hard mask through a fluorine-based plasma etching using PlasmaLab 100 (ICP-180). The hard mask pattern was then transferred to the aluminum nitride with chlorine-based plasma etching using the PlasmaLab 100 (ICP-180) system. Then, I applied the same fluorine-based plasma etching to reduce the hard mask to a few nanometers. The remaining hard mask was removed by loading the sample to vapor HF etcher for 2 minutes. The acoustic transducers are fabricated in two steps. The IDT fingers were patterned

first aligning with acoustic horn and waveguide structures the with EBL using ZEP as the resist. After that, an ebeam evaporation is applied to deposit 100 nm gold film and 7 nm chrome. Chrome is used as the adhesion layer. The IDT fingers were then made through a standard lift-off process in NMP at 90 ℃. The pads were patterned by the last EBL. The pad regions of the IDT fingers are thickened with another standard lift-off process. 300 nm gold with 7 nm chrome is deposited for the thick electrode pads. Finally, the whole devices were loaded into the vapor HF etcher. The factory set RECIPE3 is used for vHF releasing. The lateral etching rate is about 100 nm/min. The releasing process takes 20 cycles with 5 min reaction time per cycle.

4.5 CALIBRATION OF THE SURFACE ACOUSTIC WAVE TRANSDUCERS

The measurement scheme was shown in figure 4.1(b). Port 1 of the VNA was connected to the transmitter through a high-frequency microwave cable and a pair of RF probe. The receiver was connected to Port 2 of the VNA and another pair of RF probe. In the first experiment, we calibrated the performance of the transmitters and receivers through the S11 and S22 measurement. The S11 and S22 measurement results from a sample device (B121) are represented in Figure 4.1(a). Multiple acoustic resonances were detected at 3.44 GHz, 5.04 GHz, 8.21 GHz, 9.49 GHz, 10.11 GHz, 14.63 GHz, and 17.64 GHz, respectively. The resonances at 3.44 GHz and 10.11 GHz corresponded to the third harmonic antisymmetric A_0 (lambda = 1 μm) and the third harmonic symmetrical mode S_0 (lambda = 1 μm), respectively. The Lamb wave transmitter was modeled with an equivalent circuit model based on derivation in Chapter 2. As shown in Figure 4.2 (a), R_s was a series resistor representing the Joule loss on the IDT fingers region. R_1 and C_e indicated the leakage resistance and the capacitance of IDT fingers. Acoustic resonances are modeled by complex impedances to be determined.

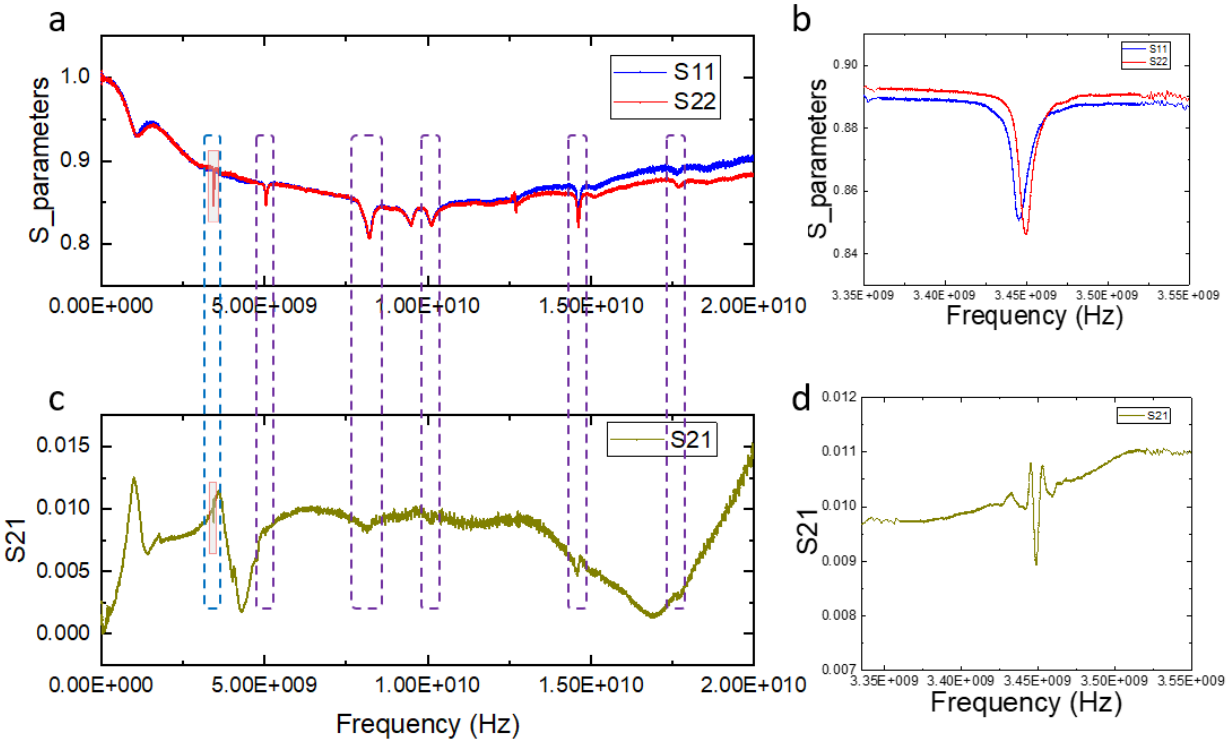

Figure 4.17 **Measurement of S-parameters of Device B121.** a) S11 and S22 measurement results for the calibration of acoustic transducers. Seven resonances are located at 3.44 GHz, 5.04 GHz, 8.21 GHz, 9.49 GHz, 10.11 GHz, 14.63 GHz, and 17.64 GHz. The small Fano resonance at around 12.5 GHz is not an acoustic resonance. It comes from calibration error, which always appears on the calibration of Port 2. b) An enlarged plot of S11 and S22 measurement of acoustic resonance at 3.44 GHz. c) S21 measurement result. The violet dashed bracket showed the small ripples corresponding to acoustic resonances in the S11 measurement. The blue dashed bracket showed the strong S21 signal measured at 3.44 GHz. d) The enlarged plot of S21 at 3.44 GHz.

It should be noted that in the equivalent circuit model derived in Chapter 2, we consider all the capacitors are opened, meaning that the parallel resistance of the capacitor is infinite. In the real devices, some leakage current may occur at the IDT fingers. Because the IDT fingers are dense and narrow, the distance between two electrodes at the finger region is only 375 nm. Some fabrication imperfection like a lift-off failure at one special IDT or the metal strip falling onto the fingers and creating a leakage channel can happen. Moreover, because the transmitter and the

receiver are close to each other, the mutual inductance can cause extra power transmission to the other port and therefore also cause extra power consumption in addition to Joule heating and acoustic excitation. However, a good approximation is solving the simplified equivalent circuit model near the acoustic resonance.

To extract the parameters from the equivalent circuit model shown in Figure 4.3(a), we first fitted the S11 signal near the acoustic resonance. The admittance is derived as:

$$Y_b(\omega) = \frac{1 - S_{11}(\omega)}{1 + S_{11}(\omega)} Y_0 = (R_s + (R_1^{-1} + j\omega C_e)^{-1})^{-1}, for\ \omega\ near\ the\ resonance\ (Eq\ 4.1)$$

After $R_s, C_e, and\ R_1$ are fitted, the second step is solving $Y_a(\omega)$. It can be solved from the following equation within the acoustic resonance:

$$Y_r(\omega) = \frac{1 - S_{11}(\omega)}{1 + S_{11}(\omega)} Y_0 = \left(R_s + \left(R_1^{-1} + j\omega C_e + Y_a(\omega)\right)^{-1}\right)^{-1}, for\ \omega\ on\ resonance\ (Eq. 4.2)$$

$$\therefore Y_a(\omega) = (Y_r(\omega)^{-1} - R_s)^{-1} - R_1^{-1} - j\omega C_e$$

After $Y_r(\omega)$ is solved. The last step is calculating the power consumption on each component:

$$P_{total}(\omega) = \frac{1 - S_{11}(\omega)}{1 + S_{11}(\omega)} = P_{R_s} + P_Z$$

$R_s\ and\ Z_0$ are connected in series, so $P = I^2 Re(Z) \propto Re(Z)$, where Z is the component's impedance.

$$\therefore P_{R_s} = P_{total} \cdot \frac{R_s}{R_s + Re\left(Z_0(\omega)\right)}$$

$$P_Z = P_{total} \cdot \frac{Re\left(Z_0(\omega)\right)}{R_s + Re\left(Z_0(\omega)\right)}$$

$Y_a, C_e, and\ R_1$ are connected in parallel, so $P = U^2 Re(Y) \propto Re(Y)$, where Y is the component's admittance:

$$\therefore P_{R_1} = P_Z \cdot \frac{R_1^{-1}}{R_1^{-1} + Re\left(Y_a(\omega)\right)}$$

$$P_{Y_a} = P_Z \cdot \frac{Re\left(Y_a(\omega)\right)}{R_1^{-1} + Re\left(Y_a(\omega)\right)}$$

Therefore,

$$P_{Y_a} = \frac{1 - S_{11}(\omega)}{1 + S_{11}(\omega)} \cdot \frac{Re\left(Z_0(\omega)\right)}{R_s + Re\left(Z_0(\omega)\right)} \cdot \frac{Re\left(Y_a(\omega)\right)}{R_1^{-1} + Re\left(Y_a(\omega)\right)}$$

$$= \frac{1 - S_{11}(\omega)}{1 + S_{11}(\omega)} \cdot \frac{Re\left(\left(R_1^{-1} + j\omega C_e + Y_a(\omega)\right)^{-1}\right)}{R_s + Re\left(\left(R_1^{-1} + j\omega C_e + Y_a(\omega)\right)^{-1}\right)} \cdot \frac{Re\left(Y_a(\omega)\right)}{R_1^{-1} + Re\left(Y_a(\omega)\right)}$$

The S11 calibration is important that it can guide our optimization of the device to maximize the electromechanical conversion efficiency. Figure 4.3(b) showed the parallel capacitance and the series resistance of Group S. The capacitance grew when the number of IDT fingers increased. The series resistance decreased while the number of IDT fingers decreased. The experimental result matched our theoretical analysis that the IDT fingers naturally worked as capacitors; thus, more IDT finger pairs lead to larger capacitance. The significant drop of series resistance showed that the series resistors were mainly contributed from Joel heating on the IDT fingers rather than other parts of the electrodes like busbars. This exploration matched with my previous experience on the electromechanical Brillouin scattering devices that the fingers burned first when increasing the input microwave power. In the parallel-plate capacitor approximation for closest fingers, the finger capacitance was proportional to the number of finger pairs. The explanation matched the theoretical analysis from the coupling of mode theory. The linear fitting of capacitance showed that the contribution of capacitance from big pads was about 94 pF. The capacitance for each IDT finger pair was about 2 pF. The result showed that the capacitor and inductance from the pad region are not negligible. Though the pad region is not considered in our equivalent circuit models, the

large IDT pad only results in an additional parallel capacitor, which can be modeled as an offset of C_e. The leakage resistance R1 of the IDT finger is much larger than any other component in the electrical circuit model. That means aluminum nitride was insulating, and the fabrication imperfection was very low; thus, the leaking at the IDT fingers was negligible.

With fitted C, R_s, and R_1, the frequency dependence of Y_a, as well as power consumption in each device, is extracted. The power consumption of each component near the acoustic resonance was presented in Figure 4.4(a). When the incident microwave frequency detuned far from the acoustic resonance, the microwave power converted to mechanical vibrations was close to zero. As the incident microwave frequency matches the Lamb wave frequency, the electromechanical coupling efficiency grew to its maximum of 6.7%, proving the efficient excitation of the Lamb wave. To systematically study the electrical performance of IDT fingers, the extracted R_s, C_e, and R_1 value is presented in Figure 4.3(d). The result matches the geometric estimation that wider IDT fingers result in larger capacitors and larger finger resistance.

4.6 ESTIMATION OF ACOUSTIC TRANSMISSION FROM S21 MEASUREMENT

Due to the space limitation between our two probes, the electrode pads of IDT fingers are close to each other. It resulted in the change of direct transmission of high-frequency microwaves from transmitters to receivers when probe engaged. The strong electromagnetic transmission is a broadband background which covers the weak acoustic transmission signal. The Lamb S0 mode at 3.44 GHz, however, has large transmission efficiency thus can be clearly distinguished from the S21 background. Although the transmission background is messy and noisy, benefiting from much slow sound velocity, the Lamb wave component is highly distinguishable by its unique phase response due to the considerable time delay. Knowing the slow varying in phase for direct

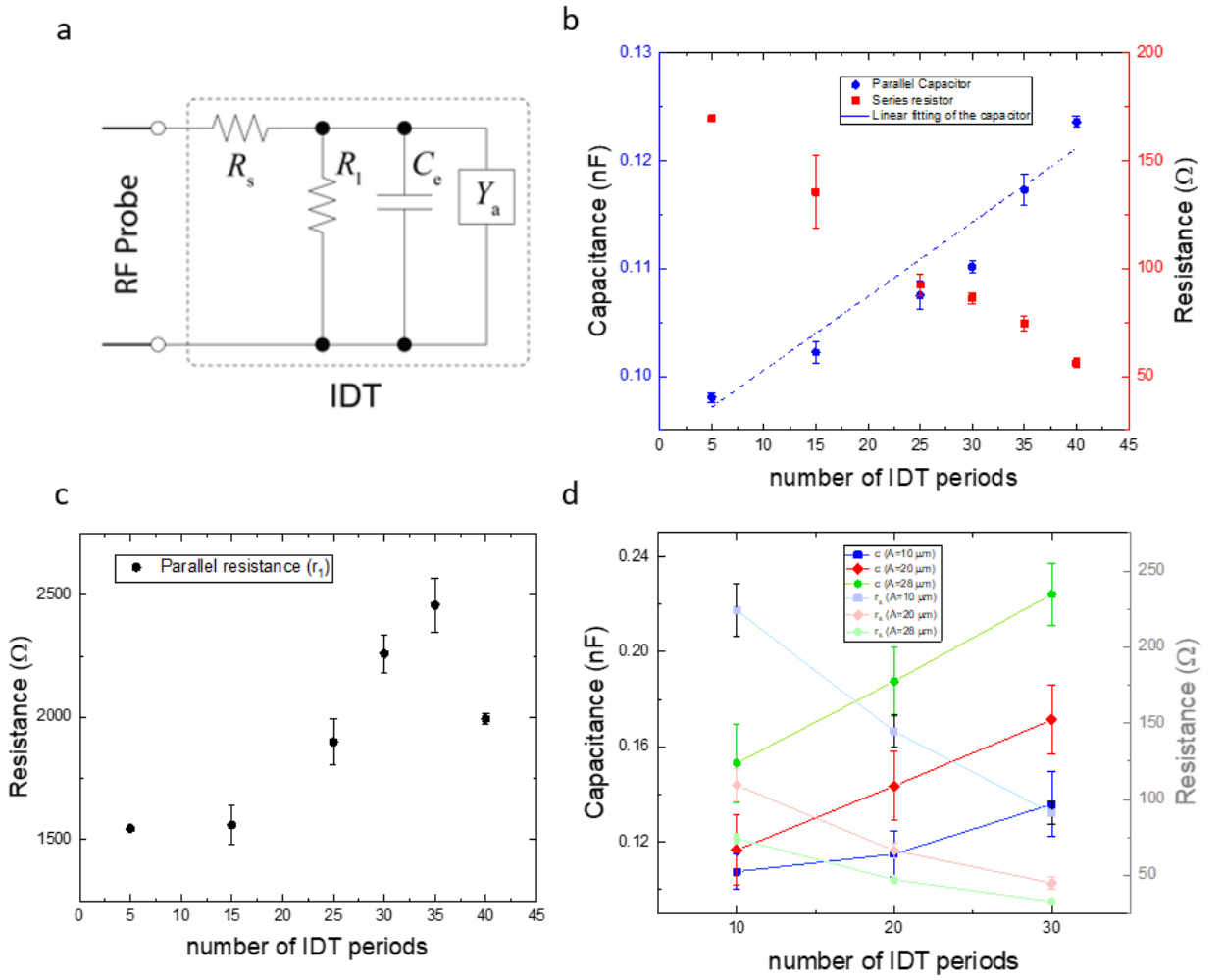

Figure 4.3 **The Characteristics of IDT with the Equivalent Circuit Model.** a) The equivalent circuit model for IDT fingers region. b) Extracted capacitance and resistance from devices in Group S. The linear fitting showed a non-negligible capacitance of electrode pads of 94 pF and the single pair of IDT fingers of 2 pF. The resistance decreases with an increasing number of IDT fingers. c) The extracted capacitor leakage resistor. The fitted result showed the resistance is at least one order of magnitude larger than the series resistor. d) The series capacitor and resistor with respect to the number of IDT finger pairs and the IDT aperture.

electromagnetic transition, we extracted the acoustic background by phenomenologically fitting the background S21 with polynomial function near the acoustic resonance. The purely acoustic response was then extracted by subtracting the fitted background signal. The S21 measurement, as

well as the acoustic resonance with background removed, is shown in Figure 4.4(b) and Figure 4.4(c). The received acoustic signal has a spiral shape, which is a clear transmission line response.

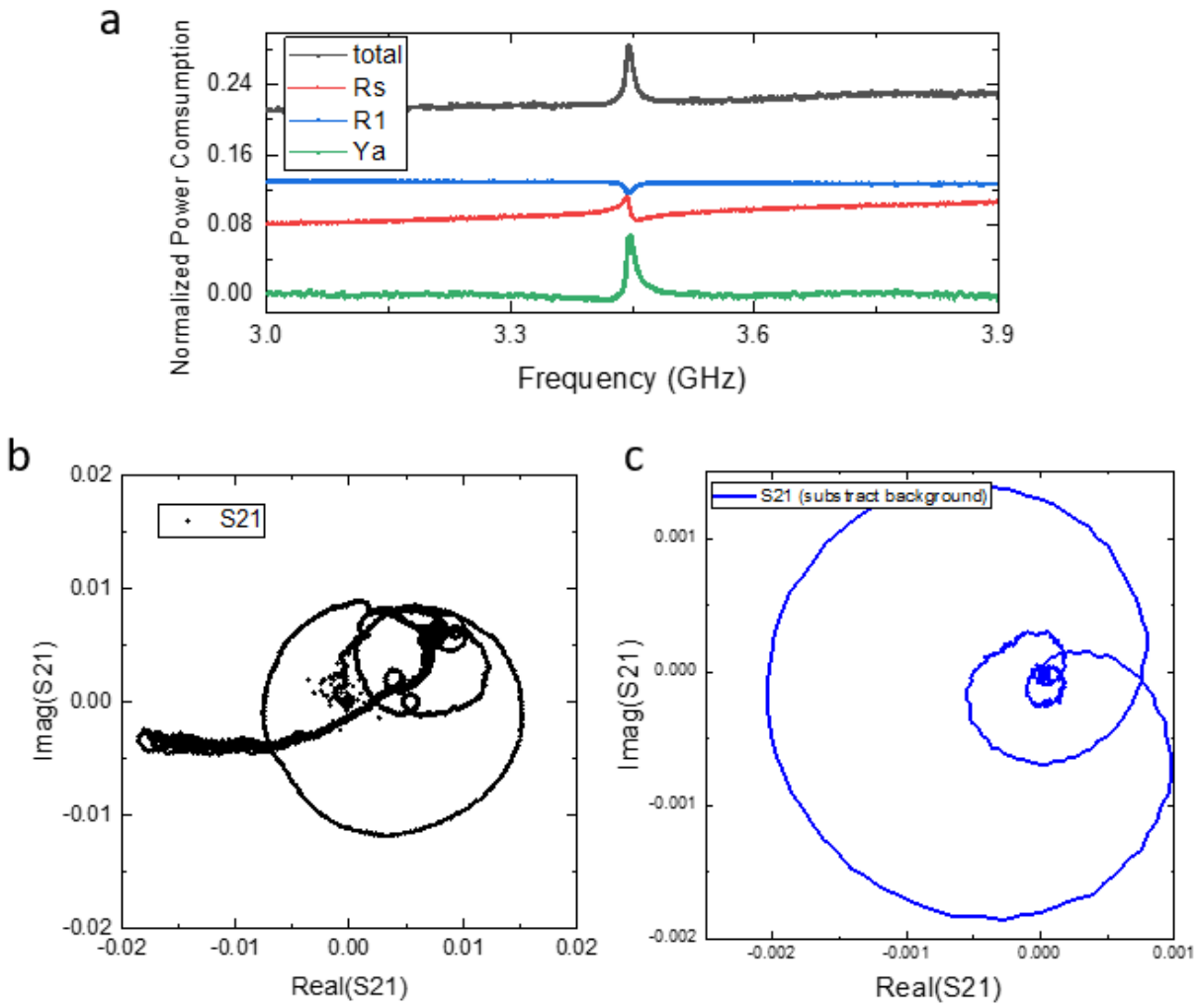

Figure 4.4 **Processed S-parameter Data for the Estimation of Acoustic Transmission.** a) The power consumption of each component of the equivalent circuit model for B121. The maximum electromechanical coupling coefficient is about 6.7%. b) The polar chart of S21 is measured on B121. c) The extracted pure acoustic S21 response by subtracting the slow varying electrical transmission background.

The suspended waveguide was working as an equivalent transmission line for acoustic waves indicating the extraction of acoustic power is successful. The complete picture of the transmission

of an acoustic wavelet around resonance from the transmitter to the receiver can be modeled as follow. The acoustic wave is generated through electromechanical coupling with electromechanical coupling efficiency κ. The acoustic wave then coupled to the suspended subwavelength waveguide with time delay t_1, loss factor α_h and the coupling efficiency κ_h. The acoustic wave traveled inside the waveguide with acoustic loss α. After the acoustic wave propagates out from the waveguide, it coupled again to the membrane mode with a coupling efficiency κ_h^* and inversely converted to electrical power with a coupling efficiency κ^*. Therefore, the electrical signal detected by the receiver should be:

$$T = |\kappa\kappa_h| e^{\frac{\alpha_h}{2}L_h} e^{\frac{\alpha}{2}L}$$

For devices with the same acoustic horn design, the acoustic loss factor can be simply obtained by:

$$\alpha = \frac{2\ln(T/\kappa)}{L}$$

Different from the membrane to waveguide coupling through the acoustic horn, which is hard to estimate and not able to be measured directly. The electromechanical coupling efficiency is extracted by decoding S11 measurement with the equivalent circuit model. The measured acoustic S21 amplitude with respect to waveguide length (L) is shown in Figure 4.5.

To minimize the drift of properties among devices, we calculated the acoustic decay rate by comparing devices in the same group with the same horn and IDT apertures. The device in Group B shows the acoustic loss at around 29 dB/mm with an acoustic coupler coupling efficiency of -15.46 dB. The result from Group A devices containing large uncertainty has an estimated acoustic loss of 40 dB/mm with an acoustic coupling efficiency of -13.91 dB. In general, the S21

measurement shows the acoustic loss inside the optomechanical waveguide ranging from 29 dB/mm to 50 dB/mm.

.

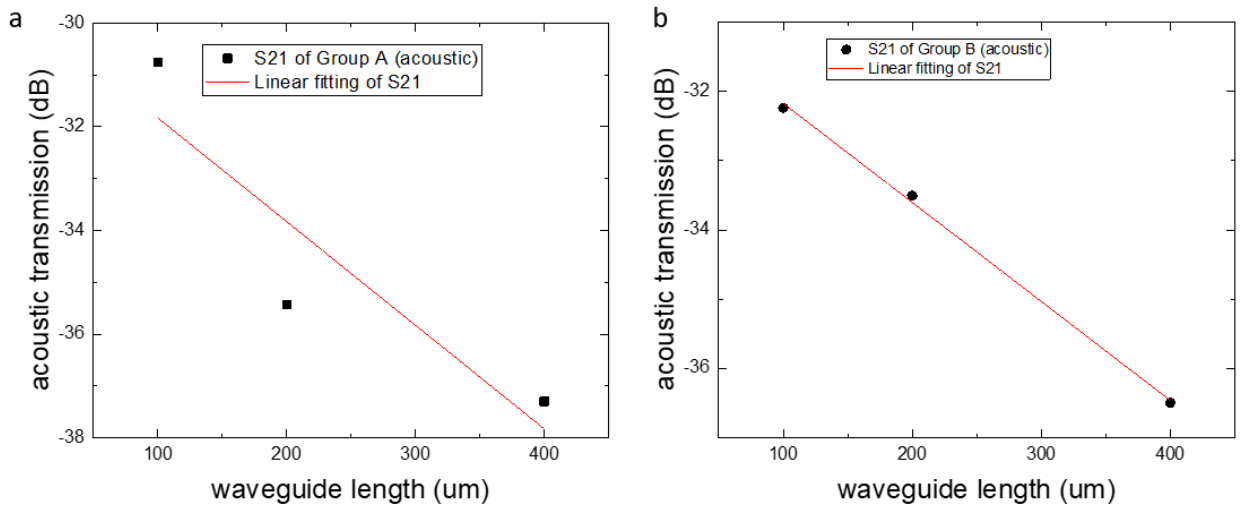

Figure 4.5 **Acoustic Loss and Coupling Efficiency from the S21 Measurement.** a) acoustic transmission signal with different waveguide length for Group A. b) acoustic transmission signal with different wavelength for Group B

In the S21 measurement, Group B shows a result with low uncertainty. Because Group B contains devices all in the center of the chip, the etching process of those devices are better and more uniform. Additionally, the Group B device has better impedance matching with the 50Ω input microwave cable. However, even the data from Group B shows a large variety. It is due to the lack of high-volume devices integration for tens or even hundreds of devices with the same designed parameters. At the same time, the strong electromagnetic background cause the filtering of acoustic transmission sensitive to the background fitting near the resonance.

4.7 VISUALIZATION OF THE SURFACE ACOUSTIC WAVE WITH THE MICROWAVE IMPEDANCE MICROSCOPY

Though we estimate the acoustic loss by direct measuring the transmission through S21 measurement, the result is not convincing due to the unexpected high loss in the phononic waveguide and low coupling efficiency of the parabolic coupler. Great thanks to our collaborator Dae-Hun Lee and Prof. Keji Lai at the University of Taxes Austin, we can directly visualize the surface acoustic wave through the microwave impedance microscopy technology. In the microwave impedance microscopy, a cantilever with a shape tip is used to scanning the surface of the substrate and sensing the change of the surrounding electromagnetic environment. The cantilever and the tip are made of top and bottom metal layers clamping a thin layer of dielectric material in between forming an equivalent LC circuit which the capacitance is sensitive to the piezoelectrical potential on the surface of the sample. When surface acoustic wave is excited, the piezoelectrical potential changes along with the mechanical vibration thus can be detected by the probe. By locking the phase between input and reflected microwave signal to the probe, the surface acoustic wave profile is detected.

Direct scanning of the acoustic wave transmission profile was performed, and the result was shown in Figure 4.6. The acoustic decay length was extracted from a curve fitting of the acoustic power by multiply an exponential decay function with the sinusoidal wave. The acoustic decay rate fitting from direct visualization is about 48 dB/mm. The result fell into the estimated acoustic loss factor with S21 measurement. There are two pieces of additional information we can get from the visualization of the Lamb wave. Firstly, the Lamb wave is coupled into the acoustic wave with moderate coupling efficiency at the entrance of the waveguide. Even though from the large time delay at the acoustic resonance in S21 spectrum, we could confirm that the received signal came

from piezoelectric back-coupling of the Lamb wave, there was some possibility the acoustic wave was transmitting through the outside acoustic channel, which was the surrounding suspended region, by multiple reflection. The visualization proved the acoustic coupling into the waveguide successfully. Second, the acoustic wavelength inside the phononic integrated waveguide is 2 μm, which is twice of the Lamb wavelength 1 μm in the membrane region. This phenomenon indicated that the acoustic phase velocity dramatically increases when the waveguide width decreases to the subwavelength-scale region. The shrink of waveguide width also deformed the mode profile dramatically. As shown in figure 4.6(a), the plane wave profile remains until it reaches the waveguide entrance, where the width of the waveguide dramatically reduces. The acoustic wave inside the phononic waveguide showed a single-mode x-shape profile.

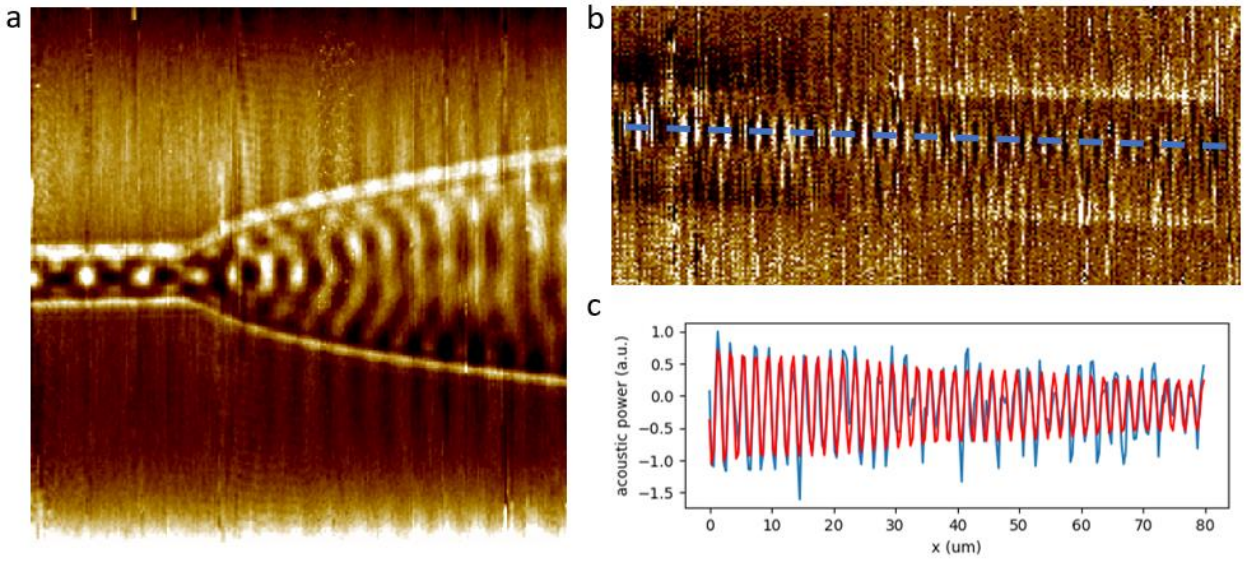

Figure 4.6 **Visualization of Lamb Waves through Microwave Impedance Microscopy (MIM).** a) The progress of Lamb wave coupling from the membrane to the waveguide. b) The acoustic displacement field visualization inside the waveguide from the microwave impedance microscopy. c) The acoustic power along the centerline of the phononic waveguide is extracted. The acoustic power is fitted with sinusoidal wave decaying along the x-direction.

4.8 SIMULATION OF ACOUSTIC COUPLING NEAR THE ENTRANCE OF THE WAVEGUIDE

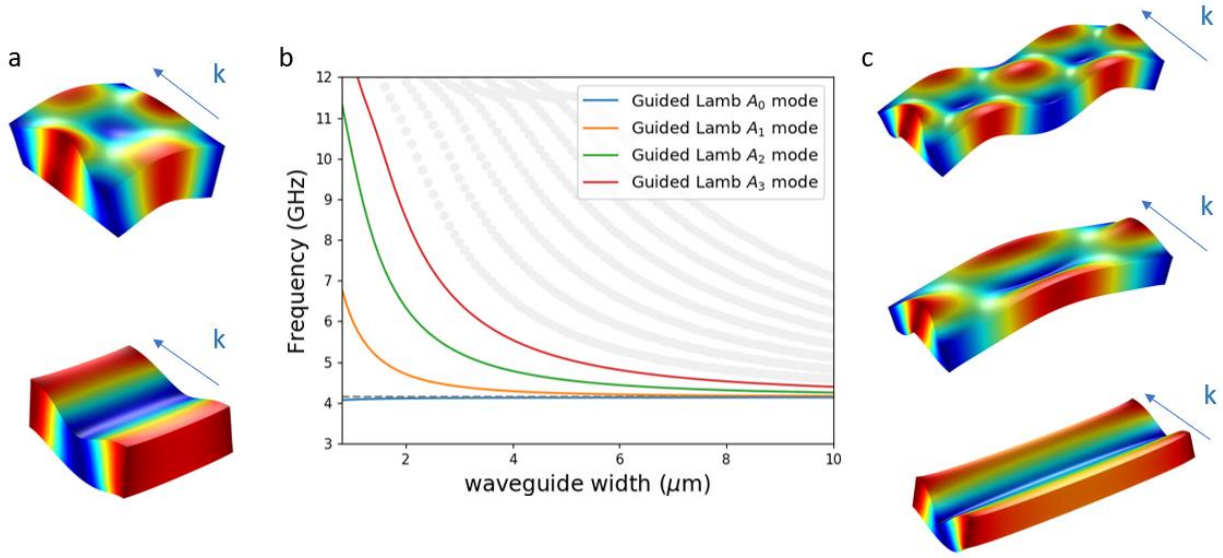

Figure 18 **Antisymmetric Guided Lamb Modes with Varying Phononic Waveguide Width.** The mode profile and eigenfrequency of 1 μm antisymmetric guided Lamb modes with respect to different waveguides width is selected in b). a) Mode profile of guided Lamb modes in the subwavelength limit. c) Mode profile of guided Lamb modes in the wide waveguide limit.

To better understand the phenomenon that occurred at the entrance of the sub-wavelength waveguide, I simulated the mode profile of anti-symmetrical modes and the dispersion curve with respect to the waveguide length. As shown in Figure 4.7, both the dispersion curve and the mode profile change dramatically from the wide waveguide limit to the sub-wavelength limit.

4.9 VISUALIZATION OF LAMB WAVE PROPERTIES IN THE COUPLING REGION

To further study the phenomenon of acoustic coupling inside the horn region, the same visualization with the microwave impedance microscopy was performed in other areas of the acoustic coupler. As shown in Figure 4.8(a), a full scan of the mechanical vibrations in the horn region was performed. But due to the low signal to noise ration and the vibration of the tips in

large area scanning, the images were covered scratch patterns. We can still get some important information that there are some circle-like interference patterns in the center of the horn structure. The other three images showed clearer zoom-in scanning of the area of interest. As shown in Figure 4.8(b), like the device shown previously, the acoustic wave modes at the entrance of the waveguide were flat due to the low optical mode intensity around the membrane mode profile at narrower waveguide width. Figure 4.8(c) is most interesting. Because the density of modes at the width is very large, the

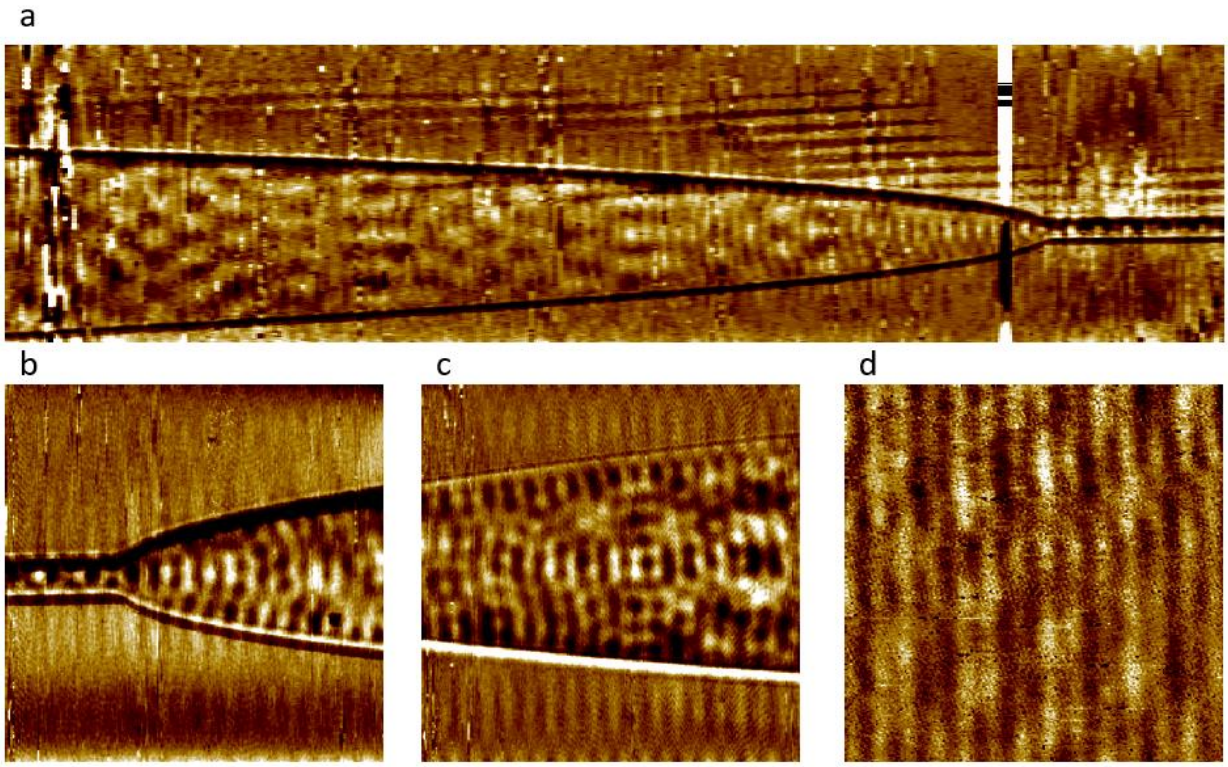

Figure 4.8 **The Visualization of the Lamb Wave Propagation in the Horn Structure.** a) A rough full scan of the acoustic waves inside the horn structure. b) The wavefronts near the entrance of the waveguide. c) The wavefronts in the middle of the horn structure. d) The wavefronts near the IDT fingers

curvature of the two side walls, however, are not as small as near the IDT region. The inter-mode coupling and the reflection from the edges are more serious. Moreover, from Figure 4.8(a), the

wider the waveguide width, the more the ripples formed in the transverse direction. This is clear evidence of the pattern formed by interference among reflections from the boundaries.

4.10 CONCLUSION AND OUTLOOK

In this chapter, I fabricated a subwavelength photonic waveguide based on the aluminum nitride membrane. Transmission of 3.4 GHz Lamb modes with 1 um wide 330 nm thick suspended waveguide was successfully measured through both S21 measurement and direct visualization. Different acoustic horns are designed for the optimization of the coupling of the Lamb wave. In the best device, we can observe small transmission signals at six acoustic resonances from the S11 and S21 spectrum. However, due to fabrication induced differences among devices, the S21 signal is not sufficient for a systematic study on all acoustic resonances. The insertion loss of the acoustic wave varying among devices. The best devices have a waveguide insertion loss of 29 dB/mm, while the majority is on the level of 48 dB/mm. The SAW visualization observed that wider IDT aperture with longer acoustic horn length caused more loss not only from the propagation loss but also from scattering and coupling to other mechanical modes. With the simulation, we observed that the design of the IDT aperture should not be far larger than the acoustic wavelength. The wider the IDT fingers, the higher the mode density near the membrane acoustic modes. That observation matched our result of acoustic coupling efficiency for Group A is larger than Group B. In general, the Lamb wave transmission in sub-wavelength suspended photonic waveguide was successfully demonstrated. The insertion loss and coupling efficiency was obtained. The design parameters of IDTs have also been studied, which can guide our future design of the devices. The future work of this project will be on increasing the performance and searching for potential applications based on the currently developed devices.

The first application that we are interested in building GHz range microwave true delay with a single mode phononic waveguide. As mentioned in previous chapters, the low group velocity of the sound makes surface acoustic wave and bulk acoustic wave devices best for high-frequency microwave signal processing. One of the key components in microwave engineering is the tunable true-time delay, which was not easy to make, especially at GHz frequency. The lamb waveguide is naturally an RF true delay for the microwave within IDT's excitation bandwidth. Surface acoustic wave devices have been using as a microwave true time delay for years. However, the surface acoustic waves diffract easily on the surface of the bulk material, which makes it hard to fabricate long-distance delay lined. Like single-mode optical fibers to free-space optics, the problems can be solved easily using the single-mode phononic waveguide. Another advantage of the suspended phononic waveguide is that the highly confined mechanical vibration is sensitive to the external force. A small bending of the waveguide not only changes the waveguide length but also tune the acoustic mode velocity inside the waveguide. Recently, due to high loss and low coupling efficiency of the waveguide, the acoustic tunable delay line suffered from high insertion loss and low signal to noise ratio. However, with the development of fabrication techniques, the shortage can be overcome.

Besides applications in the classical regime, the subwavelength-scale phononic waveguide is useful as a low-loss and low-noise communication channel between qubits. Recent research shows clear strength and weakness in different qubit. Superconducting qubit has good operability and easy and fast to control. The optical qubit which is photon has long decoherent time and low propagation loss along fiber. So, future quantum information system may need photon for communication and superconducting qubit for computation. To avoid the disturbance of superconducting qubit by incident light, recent research showed piezoelectrically excited phonon

to be a good candidate for information transfer. Moreover, surface acoustic wave phonons are also a good candidate as a low-loss communication channel between two superconducting qubit on a chip.

The applications in classical and quantum region demand better device performance. For the optimization of the current platform, there are two routes. The polycrystalline aluminum nitride has an intrinsic high acoustic loss. However, benefiting from its excellent CMOS-compatibility and high piezoelectricity, all current devices can be integrated on the silicon-on-insulator platform. The aluminum nitride thin film is only used for acoustic generation. The generated acoustic wave propagates in the silicon membrane. Because silicon is high purity single crystalline material with the nanofabrication technique well developed, the acoustic wave will encounter fewer scattering centers. On the other hand, for efficient phononic or acousto-optic devices, the efficient generation of the acoustic wave is always a better solution. We need to further increase the piezoelectricity of aluminum nitride. The reason that the current device requiring a complicated horn structure or focusing IDT design is that the electromechanical coupling factor of aluminum nitride is a bit low that small IDT will always mismatch the input transmission line impedance; thus, the observation of acoustic resonances will be challenging. By using a material with higher piezoelectricity, the acoustic coupling problem can be simply solved by fabricating smaller IDTs with a narrower aperture. New research on aluminum scandium nitride reported a five times stronger piezoelectricity than aluminum nitride. Aluminum nitride and aluminum scandium nitride are both CMOS-compatible with similar optical properties. By changing aluminum nitride with aluminum scandium nitride. The current acoustic transducer with 20 μm aperture can be shrinking down to a 5 μm wide device. From the previous Lamb wave visualization and simulation results, the narrowing of the IDT aperture will not only avoid the edge reflection and the high mode volume

region but also shortening the required coupling length of the acoustic wave. Therefore, even with similar acoustic propagation loss, the transmission of aluminum scandium nitride can be much stronger.

Chapter 5. CONCLUSIONS AND OUTLOOK

5.1 SUMMARY

The central topic of my dissertation is reinventing acousto-optics devices by tailoring nanophotonic devices in the wavelength scale. The main accomplishment is the electromechanical Brillouin scattering in the optomechanical waveguides. Detailed research of acoustic properties in the subwavelength waveguide is finished for further improvement of the acousto-optic devices.

In Chapter 1, I briefly summarize the history and state-of-art research on integrated photonic circuits and Brillouin scattering.

In Chapter 2, a detailed introduction of surface acoustic wave devices is included. Because we are working on the thin films and waveguides with the spatial confinement comparable to or smaller than the acoustic wavelength, the acoustic properties are unique. The excitation and manipulation of the auditory mode of interest lie in the center of my research topic. The theoretical model and the numerical simulation used to estimate the key performance of IDT, including the electromechanical coupling efficiency, the resonance shift, and profile distortion with metal deposited, are the important foundation for projects in Chapter 3 and Chapter 4.

In Chapter 3, I talked about the experiment of electromechanical Brillouin scattering. We successfully excited the acoustic wave at a wavelength of 500 nm and coupled it to the waveguide for the backscattering of infrared light. Three different devices $5\ \mu m \times 500\ \mu m$, $5\ \mu m \times 100\ \mu m$, and $0.8\ \mu m \times 600\ \mu m$ were fabricated. The electromechanically Brillouin scattering was successfully observed. A systematic study of the devices by scanning the microwave frequency and the laser wavelength shows the short waveguide and long waveguide reflection spectrum. The potential application of the RF-photonic link demonstrates the interconnection of the microwave

frequency band and the telecommunication bands based on rigorous phase-matching conditions for light and sound with the wavelength on the same order, even with the maximum scattering efficiency of -56 dB currently achieved.

In Chapter 4, I talked about the research on the phononic waveguide with subwavelength width. Instead of using a curved interdigital transducer to focus acoustic waves, we used flat IDT combining with an acoustic horn for the coupling of the acoustic wave. Three different groups of devices, long horns with wide IDTs, medium horns with medium IDTs, and short horns with narrow IDTs, are fabricated for comparison. Devices with different waveguide lengths are fabricated to estimate the acoustic loss inside the phononic waveguide. We successfully measure the transmission signal of the acoustic wave at 3.44 GHz. Acoustic loss of 48 dB/mm is explored by both measuring the S21 signal and visualizing the shape of the acoustic wave in the waveguide. The maximum electromechanical coupling efficiency of 6.7% is measured with wider IDT. However, in the case of coupling efficiency, the shorter horn performs slightly better for acoustic coupling. With the visualization of acoustic wave propagating inside the waveguide, we observed the interference pattern of the acoustic wave through the reflection of waveguide edges. Together with FEM simulation, we found the mode density rapidly increases for waveguide width increased, which explains the dissipation of the desired mode and weak coupling to the waveguide.

5.2 FUTURE PERSPECTIVES

Previously project has successfully demonstrated the strong interaction between acoustic waves and electromagnetic waves with wavelengths on the same scale. The only weakness of the current device is the efficiency of generating a strong acoustic wave in a waveguide. The special research on phononic waveguides on aluminum nitride shows that the high loss of acoustic waves

may be an intrinsic property of the polycrystalline film. The scattering at the grain boundaries limits the performance of acoustic devices built directly on aluminum nitride.

Two main paths are realized for solving this problem. Firstly, aluminum nitride is good for its excellent CMOS compatibility. By growing aluminum nitride on the silicon-on-insulator platform, we fabricate powerful acousto-optic devices directly on silicon. Silicon is a single crystal, and the mature fabrication technique for CMOS can directly benefit our fabrication of acoustic waveguide. If the acoustic loss is dominated by the grain boundaries, the single crystalline silicon film can directly solve this problem. If the acoustic loss is dominated by sidewall qualities of aluminum nitride, the fabrication capability of silicon is much higher and mature. With all acoustic parts integrated on silicon thin film, more functionality like compact acousto-optic modulator based on highly confined acoustic modes and optical modes, coherent control, and crosstalking between photonic crystal cavities by acoustic wave with long propagation distances, and many other phenomena of analog of quantum mechanics can be observed. The main problem that needs to be solved is how to embed aluminum nitride. Typically, aluminum nitride is sputtered on the wafer before fabricating other layers. It finally comes again to the effective way to etch away aluminum nitride with high-quality silicon left.

The other future routes are to change our platform to materials with higher electromechanical coupling efficiency like aluminum scandium nitride. The reported aluminum scandium nitride thin film has five-times stronger piezoelectricity, which means the electromechanical coupling efficiency can increase by five times. Coupling acoustic waves to subwavelength-scale phononic waveguides requires co-design of IDT and the coupler. As shown in Chapter 4, the conflict is that better coupling of acoustic waves requires narrow IDT, while stronger excitation of acoustic waves require wider IDT. By switching to a material with stronger piezoelectricity like aluminum

scandium nitride or lithium niobate, even with a narrow IDT aperture, we can find the acoustic resonance and generate a robust acoustic wave. With a mature platform developed for manipulating acoustic waves and optical waves in the same wavelength scale, acousto-optic devices based on electromechanical Brillouin scattering will be more powerful.

Reference

[1] I. Jacobs, “Optical Fiber Communication Technology and System Overview,” in *Trends in Optical Fibre Metrology and Standards*, O. D. D. Soares, Ed. Dordrecht: Springer Netherlands, 1995, pp. 567–591.

[2] K. C. Kao and G. A. Hockham, “Dielectric-fibre surface waveguides for optical frequencies,” *Proceedings of the Institution of Electrical Engineers*, vol. 113, no. 7, pp. 1151–1158, Jul. 1966, doi: 10.1049/piee.1966.0189.

[3] J. E. Sharping, Y. Okawachi, and A. L. Gaeta, “Wide bandwidth slow light using a Raman fiber amplifier,” *Opt. Express*, vol. 13, no. 16, pp. 6092–6098, Aug. 2005, doi: 10.1364/OPEX.13.006092.

[4] A. Liem, J. Limpert, H. Zellmer, and A. Tünnermann, “100-W single-frequency master-oscillator fiber power amplifier,” *Opt. Lett.*, vol. 28, no. 17, pp. 1537–1539, Sep. 2003, doi: 10.1364/OL.28.001537.

[5] J. Limpert *et al.*, “High-power femtosecond Yb-doped fiber amplifier,” *Opt. Express*, vol. 10, no. 14, pp. 628–638, Jul. 2002, doi: 10.1364/OE.10.000628.

[6] J. P. Koplow, D. A. V. Kliner, and L. Goldberg, “Single-mode operation of a coiled multimode fiber amplifier,” *Opt. Lett.*, vol. 25, no. 7, pp. 442–444, Apr. 2000, doi: 10.1364/OL.25.000442.

[7] M. Tachibana, R. I. Laming, P. R. Morkel, and D. N. Payne, “Erbium-doped fiber amplifier with flattened gain spectrum,” *IEEE Photonics Technology Letters*, vol. 3, no. 2, pp. 118–120, Feb. 1991, doi: 10.1109/68.76860.

[8] C. J. S. de Matos, L. de S. Menezes, A. M. Brito-Silva, M. A. Martinez Gámez, A. S. L. Gomes, and C. B. de Araújo, “Random Fiber Laser,” *Phys. Rev. Lett.*, vol. 99, no. 15, p. 153903, Oct. 2007, doi: 10.1103/PhysRevLett.99.153903.

[9] Y. Jeong, J. K. Sahu, D. N. Payne, and J. Nilsson, “Ytterbium-doped large-core fiber laser with 1.36 kW continuous-wave output power,” *Opt. Express*, vol. 12, no. 25, pp. 6088–6092, Dec. 2004, doi: 10.1364/OPEX.12.006088.

[10] E. Snitzer, H. Po, F. Hakimi, R. Tumminelli, and B. McCollum, “Double clad, offset core Nd fiber laser,” in *Optical fiber sensors*, 1988, p. PD5.

[11] S. V. Chernikov, Y. Zhu, J. R. Taylor, and V. P. Gapontsev, “Supercontinuum self-Q-switched ytterbium fiber laser,” *Opt. Lett.*, vol. 22, no. 5, pp. 298–300, Mar. 1997, doi: 10.1364/OL.22.000298.

[12] M. E. Fermann and I. Hartl, “Ultrafast Fiber Laser Technology,” *IEEE Journal of Selected Topics in Quantum Electronics*, vol. 15, no. 1, pp. 191–206, Jan. 2009, doi: 10.1109/JSTQE.2008.2010246.

[13] J. Homola, “Optical fiber sensor based on surface plasmon excitation,” *Sensors and Actuators B: Chemical*, vol. 29, no. 1–3, pp. 401–405, Oct. 1995, doi: 10.1016/0925-4005(95)01714-3.

[14] M. Niklès, L. Thévenaz, and P. A. Robert, “Simple distributed fiber sensor based on Brillouin gain spectrum analysis,” *Opt. Lett.*, vol. 21, no. 10, pp. 758–760, May 1996, doi: 10.1364/OL.21.000758.

[15] L. Viet Nguyen, D. Hwang, S. Moon, D. Seung Moon, and Y. Chung, “High temperature fiber sensor with high sensitivity based on core diameter mismatch,” *Opt. Express*, vol. 16, no. 15, pp. 11369–11375, Jul. 2008, doi: 10.1364/OE.16.011369.

[16] M. Paniccia, M. Morse, and M. Salib, “Silicon photonics,” *Springer, Berlin*, 2004.
[17] G. T. Reed, W. R. Headley, and C. E. J. Png, “Silicon photonics: the early years,” San Jose, California, United States, Mar. 2005, p. 1, doi: 10.1117/12.596921.
[18] A. Cutolo, M. Iodice, P. Spirito, and L. Zeni, “Silicon electro-optic modulator based on a three terminal device integrated in a low-loss single-mode SOI waveguide,” *Journal of Lightwave Technology*, vol. 15, no. 3, pp. 505–518, Mar. 1997, doi: 10.1109/50.557567.
[19] B. Chmielak *et al.*, “Pockels effect based fully integrated, strained silicon electro-optic modulator,” *Opt. Express*, vol. 19, no. 18, pp. 17212–17219, Aug. 2011, doi: 10.1364/OE.19.017212.
[20] A. Sciuto, S. Libertino, A. Alessandria, S. Coffa, and G. Coppola, “Design, fabrication, and testing of an integrated Si-based light modulator,” *Journal of Lightwave Technology*, vol. 21, no. 1, pp. 228–235, Jan. 2003, doi: 10.1109/JLT.2003.808608.
[21] B. R. Hemenway, O. Solgaard, and D. M. Bloom, “All-silicon integrated optical modulator for 1.3 μm fiber-optic interconnects,” *Appl. Phys. Lett.*, vol. 55, no. 4, pp. 349–350, Jul. 1989, doi: 10.1063/1.101905.
[22] Q. Xu, B. Schmidt, S. Pradhan, and M. Lipson, “Micrometre-scale silicon electro-optic modulator,” *Nature*, vol. 435, no. 7040, pp. 325–327, May 2005, doi: 10.1038/nature03569.
[23] K. Ohira *et al.*, “On-chip optical interconnection by using integrated III-V laser diode and photodetector with silicon waveguide,” *Opt. Express*, vol. 18, no. 15, pp. 15440–15447, Jul. 2010, doi: 10.1364/OE.18.015440.
[24] B. Mason, G. A. Fish, S. P. DenBaars, and L. A. Coldren, “Widely tunable sampled grating DBR laser with integrated electroabsorption modulator,” *IEEE Photonics Technology Letters*, vol. 11, no. 6, pp. 638–640, Jun. 1999, doi: 10.1109/68.766769.
[25] R. Nagarajan *et al.*, “InP Photonic Integrated Circuits,” *IEEE Journal of Selected Topics in Quantum Electronics*, vol. 16, no. 5, pp. 1113–1125, Oct. 2010, doi: 10.1109/JSTQE.2009.2037828.
[26] K. Preston, S. Manipatruni, A. Gondarenko, C. B. Poitras, and M. Lipson, “Deposited silicon high-speed integrated electro-optic modulator,” *Opt. Express*, vol. 17, no. 7, pp. 5118–5124, Mar. 2009, doi: 10.1364/OE.17.005118.
[27] S. Ristic, A. Bhardwaj, M. J. Rodwell, L. A. Coldren, and L. A. Johansson, “An Optical Phase-Locked Loop Photonic Integrated Circuit,” *Journal of Lightwave Technology*, vol. 28, no. 4, pp. 526–538, Feb. 2010, doi: 10.1109/JLT.2009.2030341.
[28] E. A. Kittlaus, H. Shin, and P. T. Rakich, “Large Brillouin amplification in silicon,” *Nature Photonics*, vol. 10, no. 7, p. 463, 2016.
[29] A. Rickman, “The commercialization of silicon photonics,” *Nature Photonics*, vol. 8, no. 8, pp. 579–582, Aug. 2014, doi: 10.1038/nphoton.2014.175.
[30] G. Roelkens *et al.*, “III-V/silicon photonics for on-chip and intra-chip optical interconnects: III-V/silicon photonics for optical interconnects,” *Laser & Photon. Rev.*, vol. 4, no. 6, pp. 751–779, Nov. 2010, doi: 10.1002/lpor.200900033.
[31] R. Soref, “The Past, Present, and Future of Silicon Photonics,” *IEEE Journal of Selected Topics in Quantum Electronics*, vol. 12, no. 6, pp. 1678–1687, Dec. 2006, doi: 10.1109/JSTQE.2006.883151.
[32] Cary Gunn, Adit Narasimha, Behnam Analui, Yi Liang, and T. J. Sleboda, “A 40Gb CMOS photonics transceiver,” Feb. 2007, vol. 6477, doi: 10.1117/12.702884.

[33] K. A. Williams *et al.*, “InP photonic circuits using generic integration [Invited],” *Photon. Res.*, vol. 3, no. 5, p. B60, Oct. 2015, doi: 10.1364/PRJ.3.000B60.
[34] A. Bilenca *et al.*, “InAs/InP 1550 nm quantum dash semiconductor optical amplifiers,” *Electronics Letters*, vol. 38, no. 22, pp. 1350–1351, Oct. 2002, doi: 10.1049/el:20020928.
[35] P. W. Juodawlkis, J. J. Plant, R. K. Huang, L. J. Missaggia, and J. P. Donnelly, “High-power 1.5-μm InGaAsP-InP slab-coupled optical waveguide amplifier,” *IEEE Photonics Technology Letters*, vol. 17, no. 2, pp. 279–281, Feb. 2005, doi: 10.1109/LPT.2004.839770.
[36] D. G. Rabus, M. Hamacher, U. Troppenz, and H. Heidrich, “Optical filters based on ring resonators with integrated semiconductor optical amplifiers in GaInAsP-InP,” *IEEE Journal of Selected Topics in Quantum Electronics*, vol. 8, no. 6, pp. 1405–1411, Dec. 2002, doi: 10.1109/JSTQE.2002.806692.
[37] D. Hadass *et al.*, “Time-resolved chirp in an InAs⁄InP quantum-dash optical amplifier operating with 10Gbit⁄s data,” *Appl. Phys. Lett.*, vol. 87, no. 2, p. 021104, Jul. 2005, doi: 10.1063/1.1994947.
[38] K. -. Liou *et al.*, “Operation of integrated InGaAsP-InP optical amplifier-monitoring detector with feedback control circuit,” *IEEE Photonics Technology Letters*, vol. 2, no. 12, pp. 878–880, Dec. 1990, doi: 10.1109/68.62016.
[39] A. Beling and J. C. Campbell, “InP-Based High-Speed Photodetectors,” *J. Lightwave Technol.*, vol. 27, no. 3, pp. 343–355, Feb. 2009.
[40] H. -. Bach *et al.*, “InP-based waveguide-integrated photodetector with 100-GHz bandwidth,” *IEEE Journal of Selected Topics in Quantum Electronics*, vol. 10, no. 4, pp. 668–672, Aug. 2004, doi: 10.1109/JSTQE.2004.831510.
[41] X. Duan, Y. Huang, Y. Shang, J. Wang, and X. Ren, “High-efficiency dual-absorption InGaAs/InP photodetector incorporating GaAs/AlGaAs Bragg reflectors,” *Opt. Lett.*, vol. 39, no. 8, pp. 2447–2450, Apr. 2014, doi: 10.1364/OL.39.002447.
[42] H. Lim, S. Tsao, W. Zhang, and M. Razeghi, “High-performance InAs quantum-dot infrared photodetectors grown on InP substrate operating at room temperature,” *Appl. Phys. Lett.*, vol. 90, no. 13, p. 131112, Mar. 2007, doi: 10.1063/1.2719160.
[43] N. Youngblood and M. Li, “Integration of 2D materials on a silicon photonics platform for optoelectronics applications,” *Nanophotonics*, vol. 6, no. 6, pp. 1205–1218, Dec. 2016, doi: 10.1515/nanoph-2016-0155.
[44] R.-J. Shiue *et al.*, “Enhanced photodetection in graphene-integrated photonic crystal cavity,” *Appl. Phys. Lett.*, vol. 103, no. 24, p. 241109, Dec. 2013, doi: 10.1063/1.4839235.
[45] H. Zhou *et al.*, “Enhanced photoresponsivity in graphene-silicon slow-light photonic crystal waveguides,” *Appl. Phys. Lett.*, vol. 108, no. 11, p. 111106, Mar. 2016, doi: 10.1063/1.4944414.
[46] N. Youngblood, C. Chen, S. J. Koester, and M. Li, “Waveguide-integrated black phosphorus photodetector with high responsivity and low dark current,” *Nature Photonics*, vol. 9, no. 4, pp. 247–252, Apr. 2015, doi: 10.1038/nphoton.2015.23.
[47] C. Chen *et al.*, “Three-Dimensional Integration of Black Phosphorus Photodetector with Silicon Photonics and Nanoplasmonics,” *Nano Lett.*, vol. 17, no. 2, pp. 985–991, Feb. 2017, doi: 10.1021/acs.nanolett.6b04332.
[48] R. Peng, K. Khaliji, N. Youngblood, R. Grassi, T. Low, and M. Li, “Midinfrared Electro-optic Modulation in Few-Layer Black Phosphorus,” *Nano Lett.*, vol. 17, no. 10, pp. 6315–6320, Oct. 2017, doi: 10.1021/acs.nanolett.7b03050.

[49] N. Youngblood, Y. Anugrah, R. Ma, S. J. Koester, and M. Li, "Multifunctional Graphene Optical Modulator and Photodetector Integrated on Silicon Waveguides," *Nano Lett.*, vol. 14, no. 5, pp. 2741–2746, May 2014, doi: 10.1021/nl500712u.
[50] M. Liu *et al.*, "A graphene-based broadband optical modulator," *Nature*, vol. 474, no. 7349, pp. 64–67, Jun. 2011, doi: 10.1038/nature10067.
[51] Y. Shen *et al.*, "Deep learning with coherent nanophotonic circuits," *Nature Photonics*, vol. 11, no. 7, pp. 441–446, Jul. 2017, doi: 10.1038/nphoton.2017.93.
[52] C. Wu, H. Yu, S. Lee, R. Peng, I. Takeuchi, and M. Li, "Programmable Phase-change Metasurfaces on Waveguides for Multimode Photonic Convolutional Neural Network," *arXiv:2004.10651 [physics]*, Jul. 2020, Accessed: Sep. 09, 2020. [Online]. Available: http://arxiv.org/abs/2004.10651.
[53] M. Miscuglio and V. J. Sorger, "Photonic tensor cores for machine learning," *Applied Physics Reviews*, vol. 7, no. 3, p. 031404, Sep. 2020, doi: 10.1063/5.0001942.
[54] C. Xiong, W. H. P. Pernice, X. Sun, C. Schuck, K. Y. Fong, and H. X. Tang, "Aluminum nitride as a new material for chip-scale optomechanics and nonlinear optics," *New Journal of Physics*, vol. 14, no. 9, p. 095014, Sep. 2012, doi: 10.1088/1367-2630/14/9/095014.
[55] L. Fan, X. Sun, C. Xiong, C. Schuck, and H. X. Tang, "Aluminum nitride piezo-acousto-photonic crystal nanocavity with high quality factors," *Applied Physics Letters*, vol. 102, no. 15, p. 153507, 2013.
[56] W. Pernice, C. Xiong, C. Schuck, and H. Tang, "High-Q aluminum nitride photonic crystal nanobeam cavities," *Applied Physics Letters*, vol. 100, no. 9, p. 091105, 2012.
[57] H. Li, S. A. Tadesse, Q. Liu, and M. Li, "Nanophotonic cavity optomechanics with propagating acoustic waves at frequencies up to 12 GHz," *Optica*, vol. 2, no. 9, pp. 826–831, Sep. 2015, doi: 10.1364/OPTICA.2.000826.
[58] S. A. Tadesse and M. Li, "Sub-optical wavelength acoustic wave modulation of integrated photonic resonators at microwave frequencies," *Nature Communications*, vol. 5, no. 1, p. 5402, Nov. 2014, doi: 10.1038/ncomms6402.
[59] X. Guo, C.-L. Zou, and H. X. Tang, "Second-harmonic generation in aluminum nitride microrings with 2500%/W conversion efficiency," *Optica*, vol. 3, no. 10, pp. 1126–1131, Oct. 2016, doi: 10.1364/OPTICA.3.001126.
[60] W. H. P. Pernice, C. Xiong, C. Schuck, and H. X. Tang, "Second harmonic generation in phase matched aluminum nitride waveguides and micro-ring resonators," *Appl. Phys. Lett.*, vol. 100, no. 22, p. 223501, May 2012, doi: 10.1063/1.4722941.
[61] T.-J. Lu *et al.*, "Aluminum nitride integrated photonics platform for the ultraviolet to visible spectrum," *Optics express*, vol. 26, no. 9, pp. 11147–11160, 2018.
[62] M. Stegmaier, J. Ebert, J. M. Meckbach, K. Ilin, M. Siegel, and W. H. P. Pernice, "Aluminum nitride nanophotonic circuits operating at ultraviolet wavelengths," *Appl. Phys. Lett.*, vol. 104, no. 9, p. 091108, Mar. 2014, doi: 10.1063/1.4867529.
[63] B. Dong *et al.*, "Aluminum nitride on insulator (AlNOI) platform for mid-infrared photonics," *Opt. Lett.*, vol. 44, no. 1, pp. 73–76, Jan. 2019, doi: 10.1364/OL.44.000073.
[64] S. A. Tadesse, H. Li, Q. Liu, and M. Li, "Acousto-optic modulation of a photonic crystal nanocavity with Lamb waves in microwave K band," *Applied Physics Letters*, vol. 107, no. 20, p. 201113, 2015.
[65] B. Desiatov, A. Shams-Ansari, M. Zhang, C. Wang, and M. Lončar, "Ultra-low-loss integrated visible photonics using thin-film lithium niobate," *Optica*, vol. 6, no. 3, pp. 380–384, 2019.

[66] L. He, M. Zhang, A. Shams-Ansari, R. Zhu, C. Wang, and L. Marko, “Low-loss fiber-to-chip interface for lithium niobate photonic integrated circuits,” *Optics letters*, vol. 44, no. 9, pp. 2314–2317, 2019.

[67] C. Wang *et al.*, “Second harmonic generation in nano-structured thin-film lithium niobate waveguides,” *Opt. Express, OE*, vol. 25, no. 6, pp. 6963–6973, Mar. 2017, doi: 10.1364/OE.25.006963.

[68] C. Wang *et al.*, “Integrated lithium niobate electro-optic modulators operating at CMOS-compatible voltages,” *Nature*, vol. 562, no. 7725, pp. 101–104, 2018.

[69] C. Wang, M. Zhang, B. Stern, M. Lipson, and M. Lončar, “Nanophotonic lithium niobate electro-optic modulators,” *Opt. Express, OE*, vol. 26, no. 2, pp. 1547–1555, Jan. 2018, doi: 10.1364/OE.26.001547.

[70] M. Zhang *et al.*, “Broadband electro-optic frequency comb generation in a lithium niobate microring resonator,” *Nature*, vol. 568, no. 7752, pp. 373–377, Apr. 2019, doi: 10.1038/s41586-019-1008-7.

[71] L. Shao *et al.*, “Integrated Lithium Niobate Acousto-optic Frequency Shifter,” in *Conference on Lasers and Electro-Optics (2020), paper STh1F.5*, May 2020, p. STh1F.5, Accessed: Sep. 09, 2020. [Online]. Available: https://www.osapublishing.org/abstract.cfm?uri=CLEO_SI-2020-STh1F.5.

[72] L. Shao *et al.*, “Integrated Lithium Niobate Acousto-optic Cavities for Microwave-to-optical Conversion,” in *Conference on Lasers and Electro-Optics (2020), paper FM2R.1*, May 2020, p. FM2R.1, Accessed: Sep. 09, 2020. [Online]. Available: https://www.osapublishing.org/abstract.cfm?uri=CLEO_QELS-2020-FM2R.1.

[73] P. E. Barclay, K.-M. Fu, C. Santori, and R. G. Beausoleil, “Hybrid photonic crystal cavity and waveguide for coupling to diamond NV-centers,” *Opt. Express, OE*, vol. 17, no. 12, pp. 9588–9601, Jun. 2009, doi: 10.1364/OE.17.009588.

[74] M. K. Bhaskar *et al.*, “Quantum Nonlinear Optics with a Germanium-Vacancy Color Center in a Nanoscale Diamond Waveguide,” *Phys. Rev. Lett.*, vol. 118, no. 22, p. 223603, May 2017, doi: 10.1103/PhysRevLett.118.223603.

[75] D. Le Sage *et al.*, “Efficient photon detection from color centers in a diamond optical waveguide,” *Phys. Rev. B*, vol. 85, no. 12, p. 121202, Mar. 2012, doi: 10.1103/PhysRevB.85.121202.

[76] A. Sipahigil *et al.*, “An integrated diamond nanophotonics platform for quantum-optical networks,” *Science*, vol. 354, no. 6314, pp. 847–850, Nov. 2016, doi: 10.1126/science.aah6875.

[77] S. A. Momenzadeh *et al.*, “Nanoengineered Diamond Waveguide as a Robust Bright Platform for Nanomagnetometry Using Shallow Nitrogen Vacancy Centers,” *Nano Lett.*, vol. 15, no. 1, pp. 165–169, Jan. 2015, doi: 10.1021/nl503326t.

[78] Lord Rayleigh, “On Waves Propagated along the Plane Surface of an Elastic Solid,” *Proc London Math Soc*, vol. s1-17, no. 1, pp. 4–11, Nov. 1885, doi: 10.1112/plms/s1-17.1.4.

[79] C. Campbell, *Surface Acoustic Wave Devices for Mobil and Wireless Communications*, 1st ed. USA: Academic Press, Inc., 1998.

[80] R. M. White and F. W. Voltmer, “Direct piezoelectric coupling to surface elastic waves,” *Appl. Phys. Lett.*, vol. 7, no. 12, pp. 314–316, Dec. 1965, doi: 10.1063/1.1754276.

[81] T. Watanabe and S. Fushimi, “Surface acoustic wave filter,” US4841265A, Jun. 20, 1989.

[82] J. Koike, K. Shimoe, and H. Ieki, “1.5 GHz Low-Loss Surface Acoustic Wave Filter Using ZnO/Sapphire Substrate,” *Jpn. J. Appl. Phys.*, vol. 32, no. 5S, p. 2337, May 1993, doi: 10.1143/JJAP.32.2337.
[83] T. Ushiroku and H. Ieki, “Surface acoustic wave filter,” US5694096A, Dec. 02, 1997.
[84] T. Ushiroku and H. Ieki, “Surface acoustic wave filter,” US5770985A, Jun. 23, 1998.
[85] R. GOTO, “Multi-mode surface acoustic wave filter with stepped acoustic reflectors,” US20200162056A1, May 21, 2020.
[86] J. Mazotta, “High isolation surface acoustic wave duplexer,” US20200076406A1, Mar. 05, 2020.
[87] J. A. Bahamonde and I. Kymissis, “A Non-Reciprocal Surface Acoustic Wave Filter Based on Asymmetrical Delay Lines and Parametric Interactions,” in *2020 IEEE 33rd International Conference on Micro Electro Mechanical Systems (MEMS)*, Jan. 2020, pp. 1250–1253, doi: 10.1109/MEMS46641.2020.9056343.
[88] R. Lanz and P. Muralt, “Bandpass filters for 8 GHz using solidly mounted bulk acoustic wave resonators,” *IEEE Transactions on Ultrasonics, Ferroelectrics, and Frequency Control*, vol. 52, no. 6, pp. 938–948, Jun. 2005, doi: 10.1109/TUFFC.2005.1504016.
[89] J. Ellä, “Balanced filter structure utilizing bulk acoustic wave resonators having different areas,” US6278342B1, Aug. 21, 2001.
[90] H. P. Loebl, C. Metzmacher, R. F. Milsom, P. Lok, F. van Straten, and A. Tuinhout, “RF Bulk Acoustic Wave Resonators and Filters,” *Journal of Electroceramics*, vol. 12, no. 1, pp. 109–118, Jan. 2004, doi: 10.1023/B:JECR.0000034005.21609.91.
[91] M. Bisoffi *et al.*, “Detection of viral bioagents using a shear horizontal surface acoustic wave biosensor,” *Biosensors and Bioelectronics*, vol. 23, no. 9, pp. 1397–1403, Apr. 2008, doi: 10.1016/j.bios.2007.12.016.
[92] K. Länge, B. E. Rapp, and M. Rapp, “Surface acoustic wave biosensors: a review,” *Anal Bioanal Chem*, vol. 391, no. 5, pp. 1509–1519, Jul. 2008, doi: 10.1007/s00216-008-1911-5.
[93] G. S. Calabrese, Hank. Wohltjen, and M. K. Roy, “Surface acoustic wave devices as chemical sensors in liquids. Evidence disputing the importance of Rayleigh wave propagation,” *Anal. Chem.*, vol. 59, no. 6, pp. 833–837, Mar. 1987, doi: 10.1021/ac00133a010.
[94] E. T. Zellers, R. M. White, and S. W. Wenzel, “Computer modelling of polymer-coated ZnO/Si surface-acoustic-wave and lamb-wave chemical sensors,” *Sensors and Actuators*, vol. 14, no. 1, pp. 35–45, May 1988, doi: 10.1016/0250-6874(88)80005-2.
[95] R. A. McGill *et al.*, “Performance optimization of surface acoustic wave chemical sensors,” *IEEE Transactions on Ultrasonics, Ferroelectrics, and Frequency Control*, vol. 45, no. 5, pp. 1370–1380, Sep. 1998, doi: 10.1109/58.726464.
[96] M. Noguchi and E. Hirai, “Piezoelectric element, piezoelectric actuator, ink jet recording head, ink jet printer, surface acoustic wave element, frequency filter, oscillator, electronic circuit, thin film piezoelectric resonator, and electronic apparatus,” US7766464B2, Aug. 03, 2010.
[97] D. Beyssen, L. Le Brizoual, O. Elmazria, and P. Alnot, “Microfluidic device based on surface acoustic wave,” *Sensors and Actuators B: Chemical*, vol. 118, no. 1, pp. 380–385, Oct. 2006, doi: 10.1016/j.snb.2006.04.084.
[98] S. Kapfinger *et al.*, “Dynamic acousto-optic control of a strongly coupled photonic molecule,” *Nature Communications*, vol. 6, p. 8540, Oct. 2015.

[99] D. A. Golter, T. Oo, M. Amezcua, K. A. Stewart, and H. Wang, "Optomechanical Quantum Control of a Nitrogen-Vacancy Center in Diamond," *Phys. Rev. Lett.*, vol. 116, no. 14, p. 143602, Apr. 2016, doi: 10.1103/PhysRevLett.116.143602.
[100] S. Maity *et al.*, "Coherent acoustic control of a single silicon vacancy spin in diamond," *Nature Communications*, vol. 11, no. 1, p. 193, Jan. 2020, doi: 10.1038/s41467-019-13822-x.
[101] K. J. Satzinger *et al.*, "Quantum control of surface acoustic-wave phonons," *Nature*, vol. 563, no. 7733, pp. 661–665, Nov. 2018, doi: 10.1038/s41586-018-0719-5.
[102] B. A. Moores, L. R. Sletten, J. J. Viennot, and K. W. Lehnert, "Cavity Quantum Acoustic Device in the Multimode Strong Coupling Regime," *Phys. Rev. Lett.*, vol. 120, no. 22, p. 227701, May 2018, doi: 10.1103/PhysRevLett.120.227701.
[103] R. Manenti *et al.*, "Circuit quantum acoustodynamics with surface acoustic waves," *Nature Communications*, vol. 8, no. 1, p. 975, Oct. 2017, doi: 10.1038/s41467-017-01063-9.
[104] A. Noguchi, R. Yamazaki, Y. Tabuchi, and Y. Nakamura, "Qubit-Assisted Transduction for a Detection of Surface Acoustic Waves near the Quantum Limit," *Phys. Rev. Lett.*, vol. 119, no. 18, p. 180505, Nov. 2017, doi: 10.1103/PhysRevLett.119.180505.
[105] W. Fu *et al.*, "Phononic integrated circuitry and spin–orbit interaction of phonons," *Nature Communications*, vol. 10, no. 1, p. 2743, Jun. 2019, doi: 10.1038/s41467-019-10852-3.
[106] L. Shao *et al.*, "Phononic band structure engineering for high-Q gigahertz surface acoustic wave resonators on lithium niobate," *Physical Review Applied*, vol. 12, no. 1, p. 014022, 2019.
[107] Brillouin, Léon, "Diffusion de la lumière et des rayons X par un corps transparent homogène - Influence de l'agitation thermique," *Ann. Phys.*, vol. 9, no. 17, pp. 88–122, 1922, doi: 10.1051/anphys/192209170088.
[108] P. Debye and F. Sears, "On the scattering of light by supersonic waves," *Proceedings of the National Academy of Sciences of the United States of America*, vol. 18, no. 6, p. 409, 1932.
[109] R. Lucas and P. Biquard, "Optical properties of solids and liquids under ultrasonic vibrations," *J. Phys. Rad.*, vol. 3, p. 464, 1932.
[110] A. Korpel, *Acousto-optics*, vol. 57. CRC Press, 1996.
[111] C. Schaefer and L. Bergmann, "Über neue Beugungserscheinungen an schwingenden Kristallen," *Naturwissenschaften*, vol. 22, no. 41, pp. 685–690, 1934.
[112] A. Kobyakov, M. Sauer, and D. Chowdhury, "Stimulated Brillouin scattering in optical fibers," *Adv. Opt. Photon.*, vol. 2, no. 1, pp. 1–59, Mar. 2010, doi: 10.1364/AOP.2.000001.
[113] C. S. Tsai, *Guided-wave acousto-optics: interactions, devices, and applications*, vol. 23. Springer Science & Business Media, 2013.
[114] H. Cummins and N. Knable, "Single sideband modulation of coherent light by Bragg reflection from acoustical waves," *Proceedings of the IEEE*, vol. 51, no. 9, pp. 1246–1246, 1963.
[115] M. King, W. R. Bennett, L. B. Lambert, and M. Arm, "Real-time electrooptical signal processors with coherent detection," *Applied optics*, vol. 6, no. 8, pp. 1367–1375, 1967.
[116] R. Whitman, A. Korpel, and S. Lotsoff, "Application of acoustic Bragg diffraction to optical processing techniques," in *Modern Optics*, 1967, vol. 17, p. 243.
[117] A. Korpel, *Electro-optical signal transfer apparatus*. Google Patents, 1970.

[118] A. Korpel, *Light-sound interaction system with acoustic beam steering*. Google Patents, 1969.
[119] A. Korpel, R. Adler, P. Desmares, and W. Watson, "A television display using acoustic deflection and modulation of coherent light," *Applied Optics*, vol. 5, no. 10, pp. 1667–1675, 1966.
[120] R. Adler, A. Korpel, and P. Desmares, "An instrument for making surface waves visible," *IEEE Transactions on Sonics and Ultrasonics*, vol. 15, no. 3, pp. 157–160, 1968.
[121] R. Chiao, C. Townes, and B. Stoicheff, "Stimulated Brillouin scattering and coherent generation of intense hypersonic waves," *Physical Review Letters*, vol. 12, no. 21, p. 592, 1964.
[122] G. Valley, "A review of stimulated Brillouin scattering excited with a broad-band pump laser," *IEEE Journal of Quantum Electronics*, vol. 22, no. 5, pp. 704–712, May 1986, doi: 10.1109/JQE.1986.1073005.
[123] K. Hill, B. Kawasaki, and D. Johnson, "CW Brillouin laser," *Applied Physics Letters*, vol. 28, no. 10, pp. 608–609, 1976.
[124] N. T. Otterstrom, R. O. Behunin, E. A. Kittlaus, Z. Wang, and P. T. Rakich, "A silicon Brillouin laser," *Science*, vol. 360, no. 6393, pp. 1113–1116, 2018.
[125] D. Garus, K. Krebber, F. Schliep, and T. Gogolla, "Distributed sensing technique based on Brillouin optical-fiber frequency-domain analysis," *Optics letters*, vol. 21, no. 17, pp. 1402–1404, 1996.
[126] K. Hotate and S. S. Ong, "Distributed dynamic strain measurement using a correlation-based Brillouin sensing system," *IEEE Photonics Technology Letters*, vol. 15, no. 2, pp. 272–274, 2003.
[127] R. Pant *et al.*, "On-chip stimulated Brillouin scattering," *Optics express*, vol. 19, no. 9, pp. 8285–8290, 2011.
[128] S. Chin *et al.*, "Broadband true time delay for microwave signal processing, using slow light based on stimulated Brillouin scattering in optical fibers," *Opt. Express*, vol. 18, no. 21, pp. 22599–22613, Oct. 2010, doi: 10.1364/OE.18.022599.
[129] J. Sancho *et al.*, "Tunable and reconfigurable multi-tap microwave photonic filter based on dynamic Brillouin gratings in fibers," *Opt. Express*, vol. 20, no. 6, pp. 6157–6162, Mar. 2012, doi: 10.1364/OE.20.006157.
[130] J.-C. Beugnot *et al.*, "Complete experimental characterization of stimulated Brillouin scattering in photonic crystal fiber," *Opt. Express*, vol. 15, no. 23, pp. 15517–15522, Nov. 2007, doi: 10.1364/OE.15.015517.
[131] H. Shin *et al.*, "Tailorable stimulated Brillouin scattering in nanoscale silicon waveguides," *Nature communications*, vol. 4, p. 1944, 2013.
[132] D. Marpaung *et al.*, "Low-power, chip-based stimulated Brillouin scattering microwave photonic filter with ultrahigh selectivity," *Optica*, vol. 2, no. 2, pp. 76–83, 2015.
[133] B. Morrison *et al.*, "Compact Brillouin devices through hybrid integration on silicon," *Optica*, vol. 4, no. 8, pp. 847–854, 2017.
[134] D. Braje, L. Hollberg, and S. Diddams, "Brillouin-Enhanced Hyperparametric Generation of an Optical Frequency Comb in a Monolithic Highly Nonlinear Fiber Cavity Pumped by a cw Laser," *Phys. Rev. Lett.*, vol. 102, no. 19, p. 193902, May 2009, doi: 10.1103/PhysRevLett.102.193902.

[135] D. B. Sohn, S. Kim, and G. Bahl, “Time-reversal symmetry breaking with acoustic pumping of nanophotonic circuits,” *Nature Photonics*, vol. 12, no. 2, pp. 91–97, Feb. 2018, doi: 10.1038/s41566-017-0075-2.

[136] Q. Liu, H. Li, and M. Li, “Electromechanical Brillouin scattering in integrated optomechanical waveguides,” *Optica, OPTICA*, vol. 6, no. 6, pp. 778–785, Jun. 2019, doi: 10.1364/OPTICA.6.000778.

[137] M. Schmidt, S. Kessler, V. Peano, O. Painter, and F. Marquardt, “Optomechanical creation of magnetic fields for photons on a lattice,” *Optica, OPTICA*, vol. 2, no. 7, pp. 635–641, Jul. 2015, doi: 10.1364/OPTICA.2.000635.

[138] S. Mittal, J. Fan, S. Faez, A. Migdall, J. M. Taylor, and M. Hafezi, “Topologically Robust Transport of Photons in a Synthetic Gauge Field,” *Phys. Rev. Lett.*, vol. 113, no. 8, p. 087403, Aug. 2014, doi: 10.1103/PhysRevLett.113.087403.

[139] M. Li, “Electromechanical Brillouin scattering in integrated planar photonics,” *APL Photonics*, vol. 4, no. 8, p. 080802, Aug. 2019, doi: 10.1063/1.5108672.

[140] M. Kalaee, M. Mirhosseini, P. B. Dieterle, M. Peruzzo, J. M. Fink, and O. Painter, “Quantum electromechanics of a hypersonic crystal,” *Nat. Nanotechnol.*, vol. 14, no. 4, pp. 334–339, Apr. 2019, doi: 10.1038/s41565-019-0377-2.

[141] M. Mirhosseini, A. Sipahigil, M. Kalaee, and O. Painter, “Quantum transduction of optical photons from a superconducting qubit,” *arXiv:2004.04838 [quant-ph]*, Apr. 2020, Accessed: Sep. 09, 2020. [Online]. Available: http://arxiv.org/abs/2004.04838.

[142] E. Kim *et al.*, “Quantum electrodynamics in a topological waveguide,” p. 28.

[143] “On waves in an elastic plate,” *Proc. R. Soc. Lond. A*, vol. 93, no. 648, pp. 114–128, Mar. 1917, doi: 10.1098/rspa.1917.0008.

[144] N. Kurz *et al.*, “Experimental determination of the electro-acoustic properties of thin film AlScN using surface acoustic wave resonators,” *Journal of Applied Physics*, vol. 126, no. 7, p. 075106, Aug. 2019, doi: 10.1063/1.5094611.

[145] M. M. de Lima, J. Camacho, W. Seidel, H. Kostial, and P. V. Santos, “Intense acoustic beams for photonic modulation,” in *Photonic Crystal Materials and Nanostructures*, 2004, vol. 5450, pp. 118–126.

[146] F. M. Mayor, W. Jiang, C. J. Sarabalis, T. P. McKenna, J. D. Witmer, and A. H. Safavi-Naeini, “Gigahertz phononic integrated circuits on thin-film lithium niobate on sapphire,” *arXiv preprint arXiv:2007.04961*, 2020.